Modeling stochastic behavior of state variables within the optimization of departure procedures

T. Smits

Technische Universiteit Delft

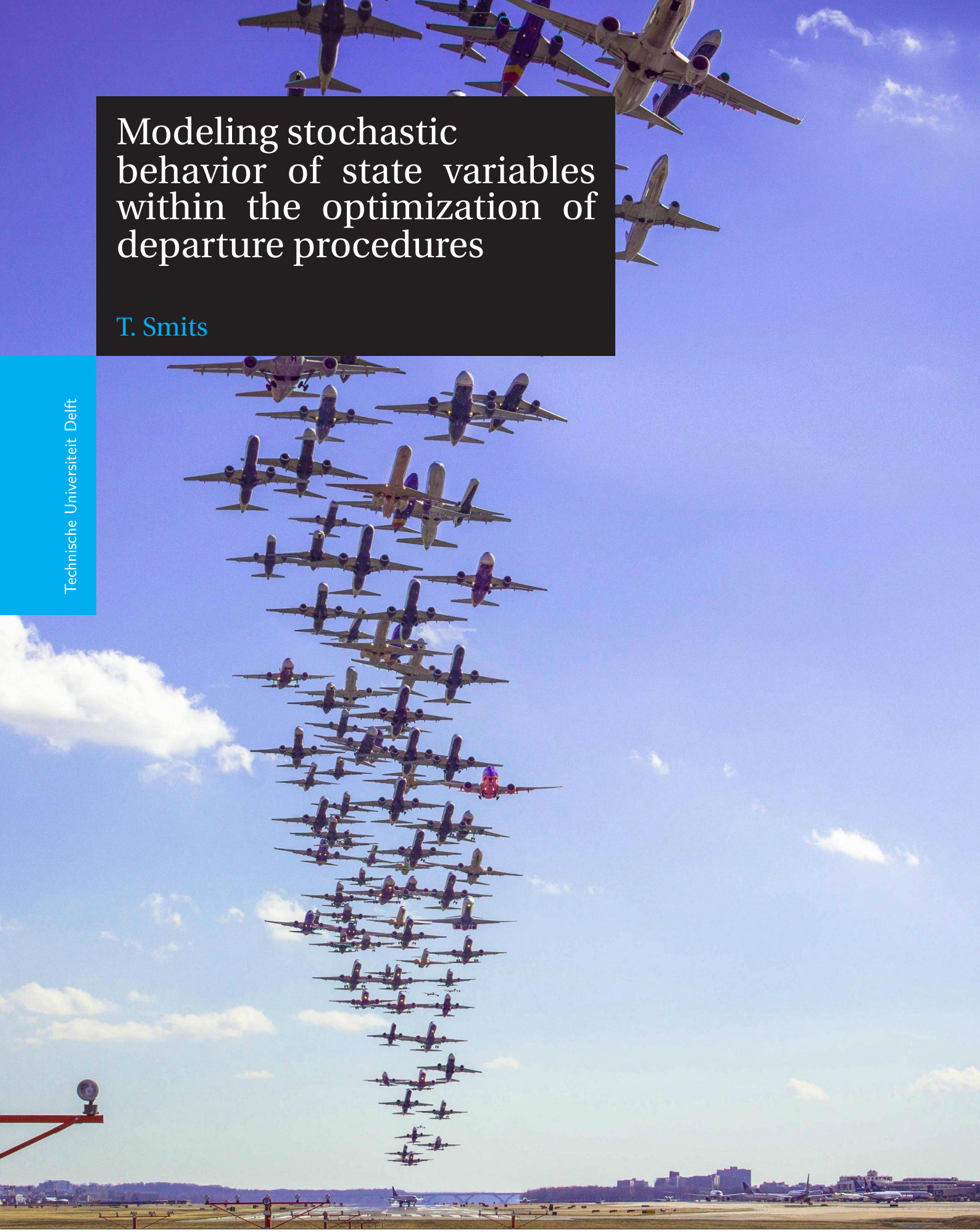

TU Delft Delft University of Technology

Challenge the future

MODELING STOCHASTIC BEHAVIOR OF STATE VARIABLES WITHIN THE OPTIMIZATION OF DEPARTURE PROCEDURES

by

T. Smits

in partial fulfillment of the requirements for the degree of

Master of Science
in Aerospace Engineering

at the Delft University of Technology,
to be defended publicly on Thursday August 23, 2018 at 2:30 AM.

Student number:	4094336	
Supervisors:	Dr. ir. S. Hartjes	TU Delft
	Dr. M. A. Mitici	TU Delft
Thesis committee:	Prof. dr. R. F. Curran,	TU Delft
	Ir. J. A. Melkert,	TU Delft

An electronic version of this thesis is available at http://repository.tudelft.nl/.

TU Delft Delft University of Technology

PREFACE

During the literature study, the development of an algorithm that was able to model the stochastic behavior of state variables and take that into account during the optimization and writing this thesis, I received a lot of support and guidance from my two daily supervisors: Mihaela Mitici and Sander Hartjes. They could always find a way to make time for my questions and therefore I would like to thank both of them.

I would also like to thank PhD Candidate Vihn Ho-Huu, which helped me set up the multi-objective evolutionary algorithm and explained the different aspects that were relevant for my research.

Finally, I would like to thank my family, friends and roommates, who all waited very patiently for me to finish this thesis.

T. Smits
Delft, August 2018

ABSTRACT

The aviation sector is an ever growing sector, which results in that the number of movements at airports also continues to grow. However, for communities located close to busy airports, this has a negative effect on their way of living. The aircraft noise can results in serious health issues, like stress, heart problems and sleep disturbance. The government attempts to decrease these negative effects with noise related regulations. With the implementation of noise abatement studies, it is possible to still increase their capacity without exceeding their noise related limitations. In these studies, the procedures are designed in such a way, that they minimize the noise impact. Previous research has shown that this is efficient approach, as it relatively fast and cheap to implement.

Next to that, new navigation procedures are implement at airport to increase their capacity and efficiency. New RNP/RNAV systems allow aircraft to fly a predefined route, while using much less airspace than conventional approaches. However, although the navigation gets more and more accurate, there is still a lateral position error present during terminal procedures. The effect of this lateral deviation, or other stochastic behavior of state variables, on the noise impact was not yet considered during the optimization of these terminal procedures, but could influences designing the most optimal route. Therefore, the objective of this thesis is to develop a method that allows the modeling of certain aircraft state variables, determine its effect on the noise impact and take that into account during the design of departure procedures, while optimizing for the number of awakening and the fuel consumption.

To model the noise and emission impact caused by a single trajectory, an existing intermediate point-mass model is combined with an integrated noise model and a geographic information system. With the use of the ANSI criterion, the noise impact is translated to a number of awakenings, which together with the fuel consumption will be the objective criteria for the multi-objective evolutionary algorithm based on decomposition. This algorithm is able to directly compute the Pareto front, which contains all the optimal solutions.

The lateral position error is modeled as a normal distribution bases on the required navigation performance during terminal procedures. To simulate the effect on the noise impact, a Monte Carlo simulation of the lateral deviation is performed. As the objective of this research is to take this effect on the noise impact into account during the optimization, an function is developed to directly approximate this effect, which saves a significant amount of computational cost. Secondly, the initial weight deviation is modeled and again simulated with Monte Carlo to determine its effect on the noise impact. However, effect was minimal and implementing it within the optimization would drastically increase the computational cost. Therefore, the initial weight deviation is not considered during the optimization of terminal procedures.

Multiple case studies were performed for two departure routes of Amsterdam Airport Schiphol, namely the Spijkerboor 2K SID and the ARNEM 3E SID. From the stochastic analysis of the lateral position error it was concluded that the received SEL values are over estimated for grid points close to the nominal trajectory and are under estimated at locations further away. This phenomenon is even more present for grid points located on the outer side of a turn segment and less present when they are on the inner side of the turn. When comparing the total number of awakenings from the deterministic simulation and the stochastic one, no significant difference was present however. It seemed that the area where the noise is overestimated was compensated with an area where it was underestimated. This was also one of the main reasons that the effect of a stochastic noise related objective function was almost not present during the optimization of departure routes. For both case studies, the Pareto fronts of both optimization approaches were almost identical and thus not resulting in different solutions.

However, when a higher cutoff value for the ANSI criterion function was used, the results will differ. The cutoff value of 65 dB (instead of 50.5) resulted in a difference of almost 1 % between the chance that awakenings occur or that they do not. This resulted in the simulation for the lateral deviation that at some grid points, were in the deterministic case no awakenings occurred, there was now a possibility that 1% or more from the population would be awaken. Therefore, the expected number of awakenings could differ significant with the deterministic number of awakenings and so new results were visible between the two optimization results.

In the end, it can be concluded that this research was successful in achieving its goal: developing a method which was able to model the stochastic behavior of a state variable and take that into account in the optimization of departure procedures. The lateral position error seemed to have more effect on the noise impact than the initial weight deviation, and even shown effect in the optimization of the Spijkerboor 2K departure when a higher cutoff SEL value was used. However, this does not assure that implementing the lateral deviation has a effect on the results of the optimization, but is always highly depended on the characteristics of the case study.

NOMENCLATURE

Greek Symbols

α	Confidence level
α	Smoothing factor
β_i	A term either equal to $+90°$ or $-90°$
χ	The heading angle of the aircraft
$\Delta\chi_i$	The heading change of RF leg i
ϵ	Lateral position error
η	The thrust setting
$\eta_{n,i}$	The normalized thrust setting at segment i
γ	The climb angle
$\gamma_{n,i}$	The normalized climb angle at segment i
μ	Bank angle
μ	The mean of a Normal distribution
Ω	Solution space
ϕ	Distributed random variable
π	Pi
ρ	Air density
ρ_0	Air density at sea level
σ	The standard deviation of a Normal distribution
θ	Family of random variables

Roman Symbols

C_i	The center of turn i
C_{turn}	Turn correction factor
D	Drag
d	Distance
$f()$	Objective function
$g^{i,j}$	Grid point
g_0	Gravitational constant
h	Altitude of the aircraft
h	Altitude
h_1	First descision altitude
L_A	A-weighted sould level
L_i	The length of a TF leg i
N	Number of simulations/runs
n	Number of indexes, sample size
P	Air pressure
P	Probability
P_0	Air pressure at sea level
pop	Population
Q	Number of discretized segments
R	Turn radius of RF leg i
s	Distance flown
T	Thrust
t	Time
V_{EAS}	The equivalent airspeed
V_{TAS}	True airspeed
W	Weight
w_i	Weight factor
X	Stochastic variable
x	A solution
x	The x-position of the aircraft
x^*	An optimal solution
x_0	The x-coordinate of the initial position
x_f	The x-coordinate of the final position
X_n	Discrete stochastic variable
X_t	Time continuous stochastic variable
y	The y-position of the aircraft
y_0	The y-coordinate of the initial position
y_f	The y-coordinate of the final position
z^*	Ideal point in a Pareto front
Z_i	The Z-score of a data point i

Other Symbols

$\dot{m}_{\text{f}}$	The fuel mass flow
Awak	The number of awakenings
Fuel	The total amount of fuel consumed
SEL	Sound exposure level

Abbreviations

AAS	Amsterdam Airport Schiphol
AAS	Amsterdam Airport Schiphol
ADS-B	Automatic Dependent Surveillance-Broadcast
ANSI	American National Standards Institute
ATC	Air Traffic Control
CDA	Continuous Descent Approach

CLT Central Limit Theory

EA Evolutionary Algorithm

EAS Equivalent Airspeed

FICAN Federal Interagency Committee on Aviation Noise

FMS Flight Management System

FTE Flight Technical Error

GIS Geographic Information System

ILS Instrument Landing System

INM Integrated Noise Model

KS-test Kolmogorov–Smirnov test

MOEA/D Multi-Objective Evolutionary Algorihtm based on Decomposition

MTOW Maximum Take-Off Weight

NADP Noise Abatement Departure Procedure

NM Nautical Mile

NSE Navigation System Error

NSGA-II Non-dominant Sorting Genetic Algorithm II

NTD Noise-Thrust-Distance

ODE Ordinary Differential Equation

OEW Operating Empty Weight

PDE Path Definition Error

PDF Probability Density Function

PMF Probability Mass Function

RF Radius-to-a-Fix

RNAV Area Navigation

RNP Required Navigation Performance

SEL Sound Exposure Level

SID Standard Instrument Departure

TAS True Airspeed

TF Track-to-a-Fix

TSE Total System Error

ZFW Zero Fuel Weight

CONTENTS

List of Figures

List of Tables

1

INTRODUCTION

There has been a high demand for air transport for the last couple of years and is expected to further increase in the future [13]. To meet this demand, it is necessary that the number of aircraft and airport operations will also increase. However, these operations have a negative effect on the environment due to pollutant emissions [15]. Next to that, the aircraft noise has an negative impact on the communities located near airports. An overexposure to aircraft noise could result in health issues, including sleep disturbance, stress and heart diseases. As an example, in 2017 Amsterdam Airport Schiphol (AAS) received over 33000 complains from 8450 people living nearby, when reaching their limit of 500,000 flight movements per year []. For airports located in inhabited areas, like AAS, the required expansion is therefore restricted so that no further decrease the quality of life will occur for the surrounding communities.

To still increase the number of airport operations, the impact of these operations should be decreased. Three areas have been identified where this is possible. First, new policies and standards could be made. Certain aircraft which are very noisy could be limited or prohibited to operate from the airport or night time restrictions could be applied. Secondly, the development of advanced aircraft technology could contribute to noise reductions By reducing the engine noise or using alternative fuels, the environmental impact could be reduced. The third area is related to the operational procedures. A couple of new procedures have already been implemented, such as the Continuous Descent Approach (CDA) and increasing the Instrument Landing System (ILS) approach angle.

Although all of the mentioned strategies contributed to the reduction of noise impact, the third one is the most suitable solution in the short term. This is because it can be applied faster than the other strategies and at a relatively low cost. To get an insight into the potential maximum gain of updating the operational procedures, optimal routes have been designed in noise abatement studies in recent years [30] [31] [20]. Here, an trajectory optimization is solved, where the objective was to minimize the noise impact, while not exceeding the operational constraints. From these previous studies, multiple conclusions could be drawn. First of all, both gradient and non-gradient optimization methods can be used in combination with a noise model and geographic information to design the optimal route [7] [11]. Secondly, it was earlier established that optimizing for just noise impact would result in infeasible solutions [28]. Therefore, noise abatement studies should always be a multi-objective optimization problem, where at least on objective should be related to noise.

Finally, most of the models used in the noise abatement studies are deterministic. Therefore, the optimization normally results in just one optimal route. However, during terminal procedures it is likely the actual flight path does not completely align with the intended path. Unexpected gusts of wind or inaccuracies in the used navigation systems could be a cause for that. When evaluating the radar data in Fig. 1.1, it can clearly be seen that in most cases the aircraft deviates from the intended departure route.

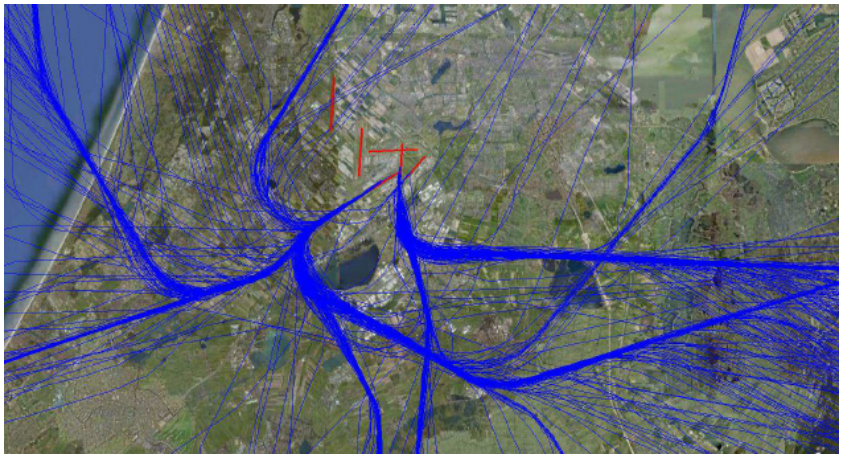

Figure 1.1: Radar data of the flight movements at AAS [8]

These and other possible uncertainties or variation of certain (state) variables are not yet taken into account during the optimization of terminal procedures. A post-optimization stochastic analysis has been performed [21] for example, but the possibility to implement the uncertainties or errors of these (state) variables in the optimization itself is still missing. Also, an analysis of how the stochastic behavior of certain (state) variables affects the overall noise impact is lacking.

With the insights and research gaps stated previously relating to noise abatement studies, this MSc thesis will attempt to answer the following research question:

"How can the stochastic behavior of aircraft state variables be modeled within the optimization of terminal departures, related to noise and economic factors?"

The goal will therefore be to develop an algorithm that can solve a multiple-objective trajectory optimization for terminal departures, while taking into account the effect of stochastic behavior of state variables on the environmental impact. Next to answering this research question, the following four sub-questions should also be answered in this thesis:

"For which objective criteria should the terminal procedures be optimized?"

"Which method will ensure to find the global optimum for the optimization problem where multiple objectives are identified?"

"Which aircraft state variables should be modeled in the stochastic analysis?"

"What is the effect of the stochastic behavior of aircraft state variables on the environmental impact?"

Therefore, the objective of this thesis should also be to identify which objective criteria are relevant for the optimization of the terminal departure routes. A suitable method has to be chosen which ensures a global optimum solution, without the need to transform the problem to single-objective optimization. At least one aircraft state variable had to be selected which stochastic behavior will be simulated. To investigate the effect of that variation on the environmental impact, a stochastic analysis will be performed. Finally, a suitable method will be chosen so that the uncertainty of that state variable can be implemented within the optimization framework.

To accomplish the objectives that are set up, a selection of models and algorithms will be applied. To simulate the aircraft states over a specified trajectory, a 2 dimensional intermediate point-mass model will be used. The emission impact is an output from the aircraft model, while the noise impact will be determined with an integrated noise model and a geographic information system. The uncertainty of state variables will be simulated with the use of a Monte Carlo simulation or approximated with a newly developed function. The Pareto front, containing all the optimal solutions, will be determined with a multi-objective evolutionary algorithm based on decomposition.

This report will start with a literature study (Ch. 2) which discusses multiple optimization techniques used in previous noise abatement studies, as well some methods how to model stochastic processes. Next, the trajectory simulation model will be explained in Ch. 3, where the aircraft model and the parameterization of the trajectory will be explained. In the following chapter (Ch. 4), the method for simulating the variation of aircraft state variables will be discussed, as well as the method used to estimate and approximate the resulting noise impact. Both models and the optimization algorithm will be verified and validated in Ch. 5. To see how the deterministic and stochastic approach will differ from each other, two case studies will be performed. The description of these case studies and the obtained results are stated in Ch. 6. Finally, the conclusions and recommendation for this thesis will be stated and elaborated on in Ch. 7.

2

LITERATURE STUDY

As was already concluded from previous noise abatement studies, an efficient way to decrease noise impact for communities surrounding airports is to redesign the terminal procedures. To achieve this, the literature review will start to explain those procedures consist of. Here, it will become clear for which aspects of the terminal procedures there is a need for further research. Apparently, there is error component present in the lateral navigation, which could be presented as a random variable. Therefore, literature about stochastic processes will be discussed, which will be used to simulate this lateral position error. Secondly, the constraints of noise abatement departure procedures will become clear. Between those limits, the departure could be optimized with respect to noise and environmental impacts. To accomplish this, methods for trajectory optimization will be discussed. One of the objective criteria for these optimization will be regarding the noise impact, so a proper understanding about aircraft noise and how to model it will be required. Literature about these subjects will be elaborated on in the final section of this chapter.

2.1. TERMINAL PROCEDURES

The flight of an aircraft between two airports consists of three major parts; the departure procedure, the arrival procedure and the part between those, the en-route part. During the later, the aircraft uses its Flight Management System (FMS) to navigate from waypoint to waypoint. When the aircraft is arriving or departing at the terminal area, the so called terminal procedures, the Air Traffic Control (ATC) will be in contact with the pilot to navigate the aircraft. This however, results in a significant amount of communication over the radio and in diversity between trajectories. Therefore, new methods and procedures are adapted during terminal procedures, which will be explained in this section.

2.1.1. NAVIGATION ROUTES

To reduce these above mentioned problems, Area Navigation (RNAV) is introduces to replace the conventional approach of navigation. With RNAV, the pilot may choose any course within a system of navigation waypoints, instead of being contained to an airway. The beginning of RNAV route is defined with an Initial Fix (IF), which is a 3 dimensional point is space, a waypoint. The route itself consists of set of legs which connect two waypoints. There are two types of legs: a Track-to-a-Fix (TF) and the Radius-to-a-Fix (RF). The TF leg is a straight leg between two waypoints. For turning in the route, the RF leg is used. Here, a constant turn radius is used to fly from one waypoint to the second one. The advantages of type of navigation with respect to the conventional method is that it conserves flight distances and reduce congestions.

Next to RNAV routes, which relies mainly on waypoints, a similar approach is available which uses on-board performance monitoring and alerting: Required Navigation Performance (RNP). This RNP is a Performance-Based Navigation (PBN) approach that allows the aircrew to fly the aircraft along a precise 3D flight path with the ability to determine aircraft position with both accuracy and integrity. This approach optimizes the use of the airspace, while it saves fuel and time. The RNP equipment is an addition to the RNAV method and and cannot be used without RNAV. Therefore, it is mostly referred to as RNP/RNAV. A schematic view of the conventional, RNAV and RNP/RNAV routes can be found in Fig. 2.1.

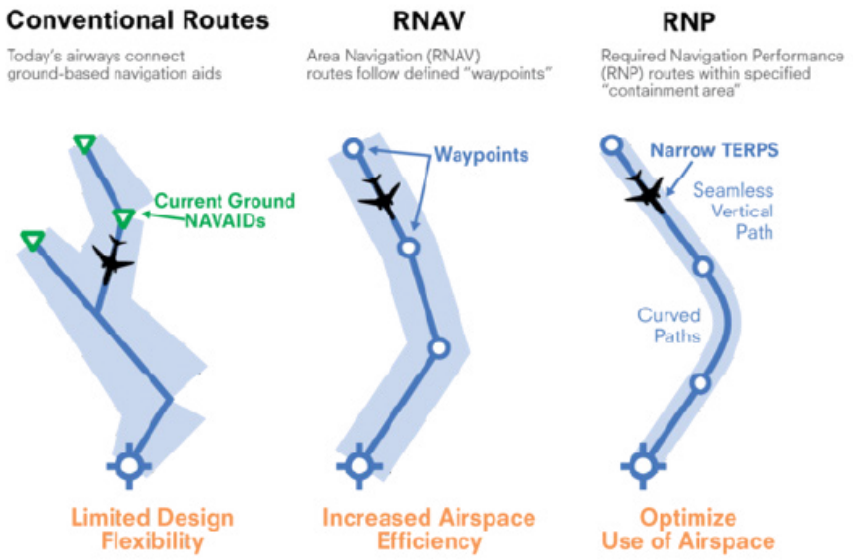

Figure 2.1: A schematic view of the conventional, the RNAV and the RNP/RNAV routes [4].

RNP also refers to the level of performance required for a specific procedure. An RNP level of 5 means that the FMS must be able to determine the position of the aircraft within a radius of 5 Nautical Miles (NM). In Europe, an RNP-1 is required for the terminal airspace, which is the equivalent to the Precision-RNAV (P-RNAV). This means that the required accuracy of the terminal procedures, within a 95 percent containment, should be equal to ±1.0 NM.

2.1.2. NAVIGATION ERRORS

The RNP/RNAV method has navigation error components, especially in lateral accuracy. The Total System Error (TSE) consists of the Path Definition Error (PDE), Flight Technical Error (FTE) and the Navigation System Error (NSE). For RNAV, the PDE is the error when the flight path does not correspond to the desired path. This can occur due to the fact that nearness to waypoints and the wind vector are not repeatable in turn and constant heading segments. With RNP/RNAV however, the PDE is assumed to be negligible. The FTE, which is the error corresponding to be ability of the aircrew or autopilot to fly the defined path, and the NSE, which is the difference between the estimated and the actual aircraft position, are both part of the TSE for the two navigation systems.

For RNAV, the distribution of the TSE is a mean zero Gaussian, since the distributions of the PDE, FTE and NSE are also Gaussian where the mean is equal to zero. For the RNP/RNAV, the accuracy requirements only define the bounds corresponding to 95 percent of the TSE. Therefore it is assumed the TSE distribution of the RNP/RNAV is also Gaussian.

2.1.3. DEPARTURE PROCEDURES

Next to procedures regarding the navigation of an aircraft, ICAO also establishes rules for the aircraft departures. Because in this thesis the focus is on reducing noise, the noise abatement procedures for the departure route will be applied. ICAO defines two different procedures: Noise Abatement Departure Procedure 1 (NADP 1) and Noise Abatement Departure Procedure 2 (NADP 2), presented in Fig. 2.2 and Fig. 2.3. respectively. With NADP 1, the focus is on reducing the noise impact for the noise-sensitive areas close to the runway, whereas with NADP 2, the focus is on the noise reduction for the areas located further away from the runway.

In the NADP 1, the aircraft starts its departure with a take-off thrust and a constant initial airspeed of V_2+10kts until it reaches an altitude h_1 of at least 800 ft. At this altitude, the thrust is reduced to a climb thrust while maintaining the airspeed of V_2+10kts until it reaches an height of 3000 ft. From here, the aircraft will continue to climb an accelerate smoothly until it reaches the en route altitude and velocity.

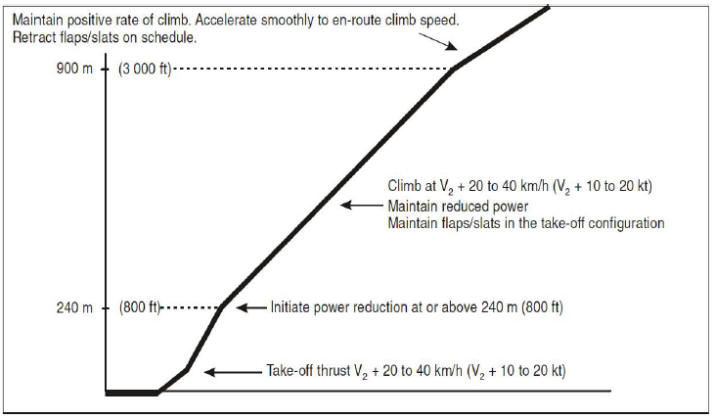

Figure 2.2: Noise Abatement Departure Procedure 1 [14].

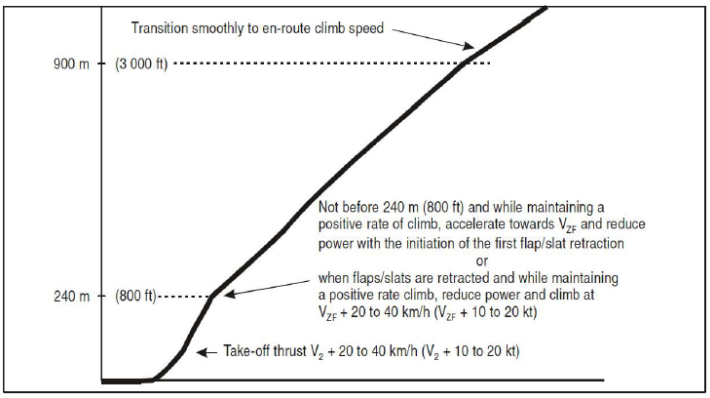

Figure 2.3: Noise Abatement Departure Procedure 2 [14].

The NAPD 2 starts the same as the first one, having a take-off thrust and constant velocity of $V_2 + 10$kts until an altitude of 800 ft. Here, the thrust is reduced to climb thrust, but now the aircraft is allowed to increase airspeed. This means that starting from 800 ft, the aircraft is no longer climbing at its maximum flight path angle. Now, the aircraft is climbing, accelerating or both, depending on the flight path angle. When it reaches an altitude of 3000 ft or the clean velocity of $V_{ZF} + 10$kts, the aircraft transits to a smooth en-route flight path angle and climb velocity.

With respect to the horizontal plane, ICAO distinguish two types of departure segments: straight segments where the turning angle is less than 15° or turn segments when turning angle is larger than 15°. The turning angle is defined as the angle between the centerline of the runway and the waypoint. Two restrictions are set by ICAO regarding a departure procedure. The first one is that the aircraft should at least fly in the same direction as the runway until it reaches an altitude of 410 ft. The second restriction is related to the bang angle μ. The maximum allowed bank angle depends on the altitude of the aircraft and is restricted as follows:

- $\mu_{\max} \leq 15°$ for altitudes below 1000 ft
- $\mu_{\max} \leq 20°$ for altitudes between 1000 ft and 3000 ft
- $\mu_{\max} \leq 25°$ for altitudes higher than 3000 ft

When an obstacle would be present within 295 ft, the maximum allowed bank angle should not be larger than 15°.

2.2. OPTIMIZATION

Within the constraints of noise abatement departure procedures, there are still many route designs possible. To identify this best suited route, an optimization is required. Typically in mathematical optimization, the minimum of a certain cost or objective function is sought, in a defined search space. The general notation for optimization is stated below:

$$\min_{x \in \Omega} : f(x) \tag{2.1}$$

As can be seen in Eq. 2.1, there is a single objective function $f(x)$. When more are present, it is called a multiple-objective optimization. The optimization is subject to a set of constraints Ω, which limits the decision space. An optimal solution x^* is a point in Ω that satisfies:

$$f(x^*) \leq f(x), \forall x \in \Omega \tag{2.2}$$

It is possible for solution x to contain multiple design variables. When this is the case, the solution is a vector of these variables:

$$\mathbf{x} = [x_1, x_2, ..., x_m]^{\mathrm{T}} \tag{2.3}$$

In a specified domain Ω, the optimal solution may not exist or may not be unique. When more than one optimal solution exists, these additional solutions are optimal with respect to their neighboring set of candidate solutions. This is a so called local optimum. When a solution is optimal for all possible solutions, it is a global optimum.

2.2.1. GRADIENT VERSUS NON-GRADIENT METHODS

In previous studies, different methods have been proposed to find this optimal solution. A tool called NOISHHH was developed by Visser and Wijnen [30, 31], which combined a dynamic optimization algorithm, a noise model and a geographic information system. The tool was able to design arrival and departure trajectories which were minimized with respect to environmental impact, while satisfying a set of relevant constraints. The tool was also able to optimize terminal procedures based on area navigation [27, 12]. A lexicographic optimization method was used by Prats et al. [20] for finding aircraft departure trajectories where the noise annoyance was minimized. A comparison of modeling methods when optimizing flight paths was done by Khardi and Abdallah [22]. Here, a direct and indirect method for solving a set of ordinary differential equations (ODEs) are presented and compared.

The above mentioned approaches all fall in the category of gradient based optimization methods. These approaches have proven to be quite efficient in finding optimal solutions, however gradient based methods have some limitations. Gradient methods solve problems where the function has to be minimized and where the search direction is defined by the gradient of the function. Since the algorithm uses gradient information, the objective function and the constraints have to be differentiable and its decision variables continuous. Moreover, due the fact that current optimization problems become more and more complex, it becomes more and more difficult to construct differentiable problems. Secondly, because you can only determine the gradient for a certain point or location, a gradient based optimization method always needs an initial solution. Therefore, their solutions have the tendency to converge to local optima when the problem has more optimal solutions. Finally, gradient based methods are suited for single-objective optimization problems, which means the solved problem will have one single solution.

Since the gradient based approach shows certain disadvantages, gradient-free optimization methods have also been used in noise abatement studies. The non-gradient optimizer called multi-objective mesh adaptive direct search (multi-MADS) has been used by Torres et al. to minimize the environmental footprint of departure procedures [7]. Hartjes and Visser [10] used a non-dominated sorting genetic algorithm (NSGA-II) in combination with a trajectory parameterization technique to design optimal departure trajectories with respect to noise and emissions criteria. The results form both [7, 10] have clearly shown that non-gradient methods are suited as well in noise abatement studies. These methods do not have to deal with most of the limitations from gradient based methods. Their ability to deal with discontinuous problems and discrete design variables, as well as finding a set of non-dominated optimal solutions makes them quite suitable for noise abatement studies. However, non-gradient methods have one major limitation: their computational

cost. The fact that non-gradient methods use a random search area, gives them the advantage of not needing an initial solution and to more likely converge to a global optimum, but also requires to do significantly more evaluations, which are time consuming.

2.2.2. MULTIPLE-OBJECTIVES

As stated in previous noise abatement studies [30, 31, 20, 10], optimizing terminal procedures should always be done for multiple objectives. This makes the designing of optimal routes a multiple-objective optimisation problem, as stated in Eq. 2.4.

$$\min_{\mathbf{x}\in\Omega} : \mathrm{F}(\mathbf{x}) = \left[f_1(\mathbf{x})), f_2(\mathbf{x}))...f_n(\mathbf{x})\right] \tag{2.4}$$

The main differences with respect to a single-objective optimization is that there exist two or more distinct goals and that normally the optimal set consists of more than one solution, see Eq. 2.5:

$$\mathbf{x}^* = \left[\mathbf{x^{(1)}}\mathbf{x^{(2)}}...\mathbf{x^{(n)}}\right] \tag{2.5}$$

A set of solutions are optimal when each solution is non-dominant to each other. A solution $\mathbf{x^{(1)}}$ is stated to be dominant to solution $\mathbf{x^{(2)}}$ if both conditions are true [6]:

- $f_i(\mathbf{x^{(1)}})$ is never better than $f_i(\mathbf{x^{(2)}})$, for all objective functions $[f_1, f_2, ..., f_n]$
- $f_i(\mathbf{x^{(1)}})$ is better than $f_i(\mathbf{x^{(2)}})$, for at least one objective function f_i, $i \in \{1, 2, ..., n\}$

Solution $\mathbf{x^{(1)}}$ does not dominate $\mathbf{x^{(2)}}$, if one of these conditions is not met. When the set of solutions is proven to be non-dominant, then the solutions are located on the so called Pareto front. This Pareto set of solutions, which is illustrated in Fig. 2.4, contains all the global optimal solutions for the multiple-objective optimization problem.

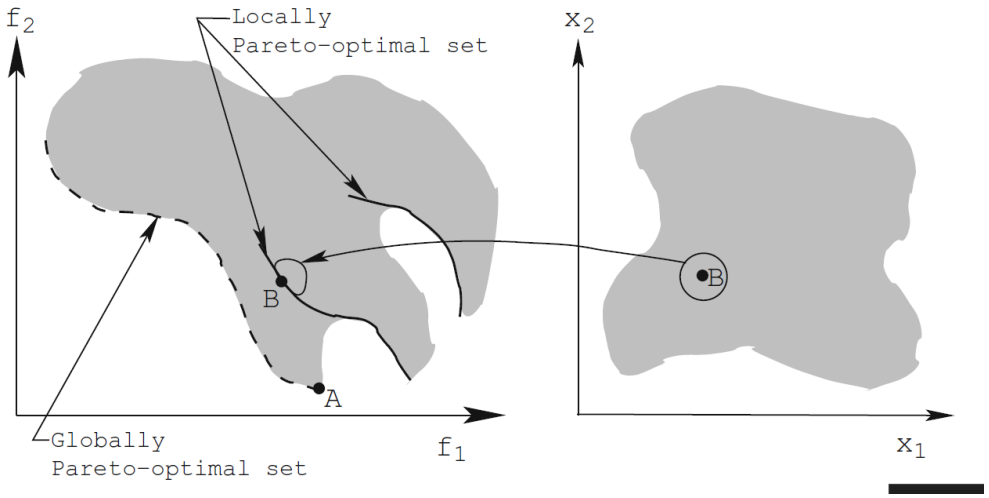

Figure 2.4: The Pareto-optimal solution curves for two objective functions. [6]

When the Pareto front is determined, a trade-off between the different solutions can be made with the use of higher level information about the problem. This information is often non-technical and experience driven and not always available. In a preferred scenario, higher level information is available before the optimization, so that the multiple-objective problem can be converted to a single-objective one. This is called *a priori* approach. In previous studies, such as [28, 11], additional information is used to estimate the relative importance of the objective functions. A weight factor is assigned to each criterion and they are combined together in one single objective function. This method is called the Weighted Sum Approach and looks as follows:

$$\min_{\mathbf{x}\in\Omega} : \mathrm{F}(\mathbf{x}) = \sum_{i=1}^{n} w_i f_i(\mathbf{x}) \tag{2.6}$$

Because the required higher level information is in most cases not completely available, it would be better to do the objective criteria trade off after the optimization. This approach is called *a posteriori*. To apply this approach, it is required to directly compute the Pareto front in the optimization. Hartjes [10] used this approach and was successful in creating the Pareto front with the use of an Evolutionary Algorithm, the NSGA-II. After the optimization, an analysis of the set of optimal solutions was done and a suitable route was selected.

2.2.3. MULTI-OBJECTIVE EVOLUTIONARY ALGORITHM BASED ON DECOMPOSITION

As stated previously, an evolutionary algorithm has the ability to converge almost directly to the globally Pareto-optimal set of solutions, while dealing with multiple objectives and complex, non-continuous problems. However, the major disadvantage is that to do so, the computation time is significantly long. This is due the fact that an EA is a search method based on the principles of genetics. The problem is encoded in a chromosomal manner and a fitness test (or objective function) is applied to determine if a found solution is better or worse than its previous one. After the fitness is determined, the solutions can start to evolve with the following steps:

- **Initialization:** The initial population (where the size is user selected) of possible solutions is generated at random across a certain search space Ω.
- **Selection:** Here, the new generation is evaluated by the objective functions $\mathrm{F}(\mathbf{x})$ and the population with better fitness values will have a higher change of repopulating. Therefore, making sure the algorithm converges to the desired solution.
- **Crossover:** From the initial population, an offspring population is created. Here, crossover between two parents occurs with a certain probability, which can be adjusted by the user. Without this crossover, the offspring will exactly be the same as the parents chromosomes.
- **Mutation:** With a probability, a portion of the new individuals will have a small change in their chromosome. This allows to induce a random walk through the search space. This mutation factor can also be adjusted by the user.
- **Replacement:** The offspring population created by the selection replaces the original parental one. Now the algorithm will run again, until the final population converges to the optimal solution $\mathbf{x}^*$.

Due to the fact that the creation of a population is partly random, it can take several iterations before the optimal solution is reached. For every iteration, the entire population has to be evaluated, which means the number of evaluations will be significant. In noise abatement studies, a complete simulation of the trajectory is required for each evaluation, which therefore results in a time-consuming process.
To still have the advantages of an evolutionary algorithm, but limit the computation time, this thesis will use a Multi-Objective Evolutionary Algorithm based on Decomposition (MOEA/D). The MOEA/D has recently been developed and proven to out perform the NSGA-II [32]. Ho-Huu and Hartjes [26] have improved the MOEA/D and used it successfully while designing noise abatement departure trajectories. In MOEA/D, the multiple-objective problem is decomposed into a number of scalar optimization sub-problems. The weighed Tchebycheff decomposition approach is used here, where the ideal point $\mathrm{F}(\mathbf{x}^*)$ is determined by:

$$\min_{\mathbf{x}\in\Omega} \mathrm{g}^{te}\left(\mathbf{x}|\mathbf{w},\mathbf{z}^*\right) = \max_{1\leq i\leq n}\left\{w_i|\mathrm{F}_i(\mathbf{x}) - \mathbf{z}_\mathbf{i}^*|\right\} \tag{2.7}$$

where $\mathbf{w} = [w_1,...,w_n]^{\mathrm{T}}$, where the weights are always positive ($w_j \geq 0$) and the sum of a set of weights is equal to 1 ($\sum_{i=1}^{n} w_i = 1$) [16]. The reference point $\mathbf{z}^* = [z_1^*, z_2^*, ..., z_n^*]$ is defined as set containing the minimal solution of each individual objective function: $z_i^* < \min\left\{f_i(\mathbf{x})|\mathbf{x}\in\Omega\right\}, i = 1,...,n$. The sub-problems are then optimized with the use of an evolutionary algorithm. The solutions of each scalar optimizations will form the Pareto-optimal front. A normalized scenario where this method is applied is shown in Fig. 2.5.

For a more detailed description of the MOEA/D algorithm, see App. B.

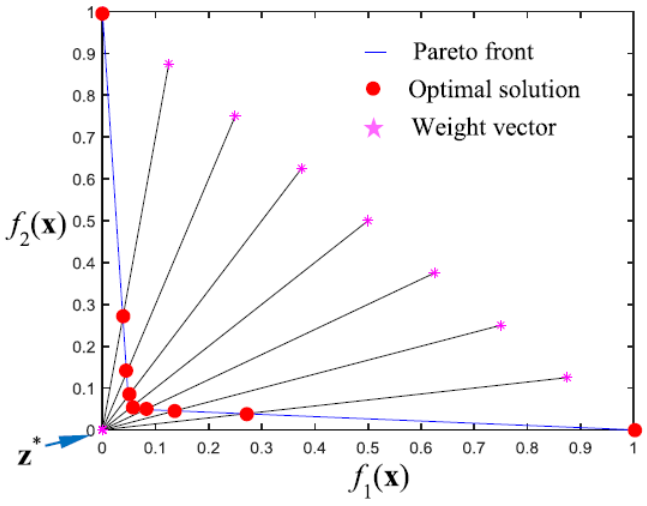

Figure 2.5: Distribution of optimal solutions op Pareto front by using $\mathbf{z}^*$ for two objective functions [24].

2.3. STOCHASTIC PROCESSES

Although new implementations are used for the navigation during terminal procedures, there still is a lateral position error present. This error can be represented as a random variable or a stochastic process. The general definition of a stochastic process $\{X_\theta\}$, with $\theta \in \Theta$ is a family of random variables, one for each $\theta \in \Theta$, or

$$\{X_\theta\} = \{X_\theta, \theta \in \Theta\} \tag{2.8}$$

Such a process can be continuous, denoted as $\{X_t\}$ or a discrete, denoted as $\{X_n\}$. The lateral position example would be a continuous stochastic process, since the error is distance from the nominal trajectory and can have any length.

When a model possesses some variables which have some inherent randomness , it is called a stochastic model. In a stochastic model, the same initial conditions and parameters can lead to set of different solutions. This in contrast with a deterministic model, where the output is fully determined by the input. In most previous noise abatement studies, a deterministic model was used to simulate an aircraft during terminal procedures. However, when the lateral navigation error would be taken into account, the simulation model would a stochastic one.

2.3.1. PROBABILITY THEORY

When simulation a sample of a random variable, like for instance a position error, the value is not in advance. However, it can be known how likely it is a certain value will occur. In general, this probability of occurrence of a stochastic process X can be stated in a mathematical function called the probability distribution. The distributions can be divided in two classes, discrete and continuous probability distributions. The discrete distribution, for scenarios where the outcome is a discrete number, can be encoded by a list consisting of the outcome probabilities named the probability mass function (PMF). Example of this kind of distributions are the Poisson distribution and the Bernoulli distribution. A continuous probability distribution is applicable to scenarios where the set of outcomes can take continuous range of values. Continuous distributions are generally described with the use of a probability density function (PDF), which can be denoted for an interval $[a, b]$ as:

$$P(a \leq X \leq b) = \int_a^b f_X(x)dx \tag{2.9}$$

The main difference with a discrete distribution is that a continuous distribution has a probability for a certain interval of values, while a discrete one has a probability of each value.

An example of a continuous probability distribution is the Gaussian or normal distribution, which is often used in natural and social sciences, but also to represent the lateral navigation error. The PDF of a normal distribution is stated as follows:

$$f_X(x) = \frac{1}{\sqrt{2\pi\sigma^2}} e^{-\frac{(x-\mu)^2}{2\sigma^2}} \tag{2.10}$$

The normal distribution is symmetrical and defined with two parameters: one for location ($\mu \in \mathbb{R}$) and one for the squared scale ($\sigma^2 > 0$). When a variable is normally distributed, it is often referred as $N(\mu,\sigma^2)$. In Fig. 2.6 multiple normal distributions with different parameter settings are plotted, where the effect of the parameters is visible.

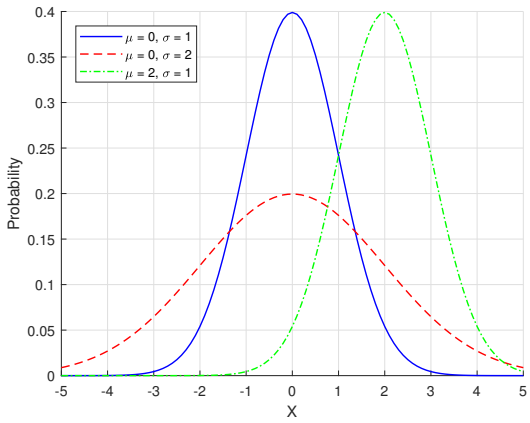

Figure 2.6: Normal distributions with different parameters settings.

The long-term average value of a distribution is called the expected value or the expectation. For discrete distributions, this would be equal to the sum of each possible value multiplied with its likelihood. For a continuous distribution, this would be the integral of the variable with respect to its probability density, see Eq. 2.11.

$$\mathrm{E}[X] = \int_{\mathbb{R}} x f_X(x) \tag{2.11}$$

A second characteristic of a probability distribution is the variance. The variance measures how fas a set of random variables are spread out with respect to their average of expected value. Therefore, when a distribution would have a lower variance, it would be more likely that a single generated value will be equal to the expected value. A distribution with a higher variance has therefore more uncertainty, so it would a less robust assumption to present the random variable just as the expected value. In general, the variance of X is defined as:

$$\mathrm{Var(X)} = \mathrm{E}[(\mathrm{X} - \mathrm{E(X)})^2] = \mathrm{E}[\mathrm{X}^2] - \mathrm{E}[\mathrm{X}]^2 \tag{2.12}$$

The expected value and the variance of a normal distribution can be calculated with Eq. 2.11 and Eq. 2.12 respectability, which results in for the expected value is equal to the average, $\mathrm{E(X)} = \mu$, and the variance is equal to the squared standard deviation, $\mathrm{Var(X)} = \sigma^2$. In Fig. 2.7 the average μ and standard deviation σ are pointed out in a normal distribution.

When sampling from a normal distribution $N(\mu,\sigma^2)$, it is possible to measure the sampled value X_i with respect to the mean. The number of standard deviations between the mean and a data point is called the Z-score or the standard score and is calculated as follows:

$$Z_i = \frac{X_i - \mu}{\sigma} \tag{2.13}$$

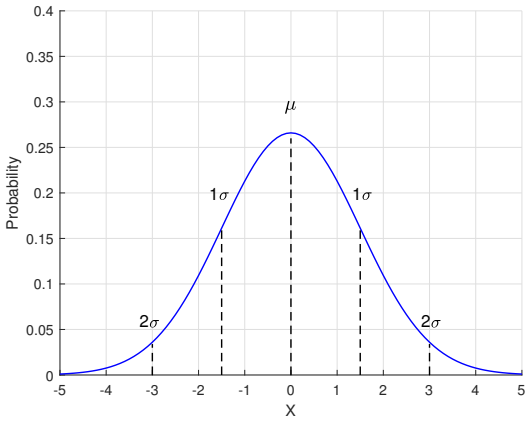

Figure 2.7: A normal distribution where μ and σ are highlighted.

The Z-score tells where the sample value is located on the distribution in number of standard deviations. When values are above the mean, the standard score has a positive value, otherwise a negative one. When multiple samples are generated, the mean of those samples $\bar{X}_n$ can also be tested again the Z-score with this equation:

$$Z_n = \frac{\bar{X}_n - \mu}{\frac{\sigma}{\sqrt{n}}} \tag{2.14}$$

where n is the number of samples drawn from the distribution $N(\mu, \sigma^2)$. Now, the Z-score will tell how many standard errors there are between the sample mean and the overall distribution mean. When the sample size increases, this error will become smaller. This is covered in the Central Limit Theorem (CLT), which states that average of the samples will be equal to the distributions mean when the n reaches infinity, or in other words:

$$\lim_{n\to\infty} \mathrm{P}(Z_n \leq a) = \mathrm{P}(Z \leq a) \tag{2.15}$$

for all $a \in \mathbb{R}$ and where $Z \sim N(0,1)$.

2.3.2. MULTIPLE STOCHASTIC VARIABLES

It can be possible that a stochastic model consists of multiple random variables. Although it is not always possible to predict the shape of the overall distribution, the expected value of the total model can be determined. For two random variables X and Y, it is calculated as follows:

$$\mathrm{E[X+Y]} = \mathrm{E[X]} + \mathrm{E[Y]} \tag{2.16}$$

To determine the expected value of more than two distributions, the sum of the expected value of each distribution is taken due to the fact that the expected value operator is linear.

To measure the joint variability of two random distributed variables, the covariance should be determined. In contrast with the variance, the covariance tells how two distributions vary together. The covariance of X end Y is calculated as follows:

$$\mathrm{Cov(X,Y)} = \mathrm{E[(X - E[X])(Y - E[Y])]} \tag{2.17}$$

For this, the two distributions have to be dependent of each other. They are if the occurrence of the one effect the probability of occurrence of the other value. If this it not the case, they are independent to each other and the covariance is equal to zero. If the covariance of a set of probability distributions $\mathbf{X} = [\mathrm{X}_1 ... \mathrm{X}_n]^{\mathrm{T}}$ should be determined, the so called covariance matrix is required:

$$\mathbf{S} = \mathrm{Cov}[\mathbf{X},\mathbf{X}] = \begin{bmatrix} \mathrm{Cov}[X_1,X_1] & \dots & \mathrm{Cov}[X_1,X_n] \\ \vdots & \ddots & \vdots \\ \mathrm{Cov}[X_n,X_1] & \dots & \mathrm{Cov}[X_n,X_n] \end{bmatrix} \tag{2.18}$$

When determining the variance of that set of distributions **X**, the total sum of all the elements of the covariance matrix **S** can be used. This can be simplified by taken into account that the covariance of two identical distributions is equal to the variance of that distribution. The variance becomes:

$$\mathrm{Var}[\mathbf{X}] = \sum_{i=1}^{n} \mathrm{Var}[X_i] + 2 \sum_{1 \le i < j < n} \mathrm{Cov}[X_i, X_j] \tag{2.19}$$

2.4. NOISE

One of the main objectives when designing optimal departure procedures, is noise impact reduction. This noise, just like all sound, comes from a source, which in this case is an aircraft. The sound production can be divided in two relevant categories: mechanical noise, which relates to the engine parts, and aerodynamic noise, caused by the airflow around the surface of the aircraft. Overexposure to this noise can have health consequences, like sleep disturbance, heart diseases and stress. To minimize this noise impact caused by a single departure, a method is required to determine it. In this section, the model to estimate the noise will be explained. Next to that, the method for determining the impact caused by that noise will also be discussed.

2.4.1. NOISE MODEL

Noise, or sound, is caused by a vibration and that energy can be transmitted through solids, liquids or gas in the from of waves or sound pressure. That pressure, that impinges on the ear, is the sound people hear. The sound can be measured by comparing the sound pressure of the source with a reference pressure. For example, the source could be an aircraft flyover and the quietest sound audible the reference one. This ratio is called decibel (dB) and since the range of sound pressure rations is quite large, a logarithmic scale is used. The noise generated by an aircraft has many frequencies and cannot all be completely heard by a human ear. Therefore, to better quantify aviation noise with respect to the characteristics of the human ear, weighting filters will be applied. Although more filters exists, the A-Weighted filter is mostly used in aviation to correct the raw noise measurements for frequencies less effective for humans. This filter together with the B-, C- and D-weightings are plotted in Fig. 2.8 .

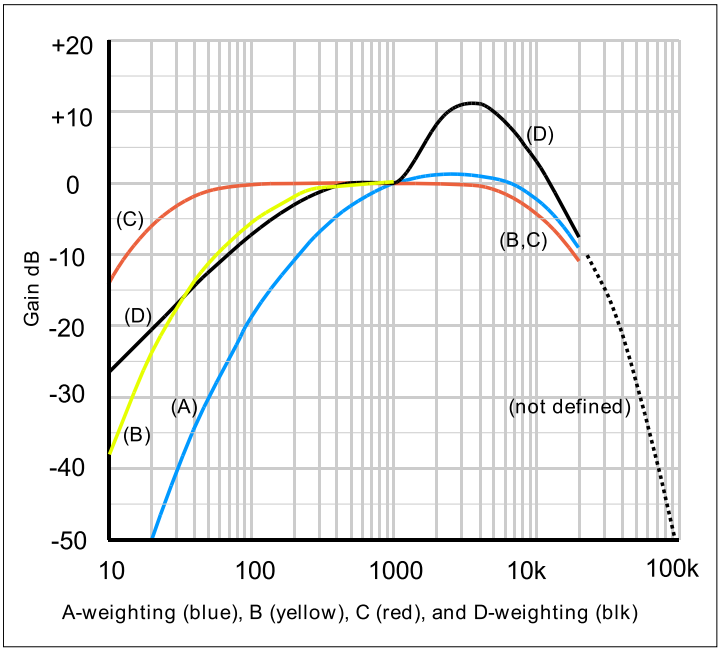

Figure 2.8: Acoustic weighting curves [1]

Next to the sound level, its exposure time is also important to take into account when determining the noise impact on an environment. Their exits many cumulative noise exposure metrics, but for a single aircraft flyover the Sound Exposure Level (SEL) is most commonly used. SEL is a logarithmic measure of sound exposure relative to a reference value. Mathematically, SEL the sum of the sound energy over the duration of a noise event and normalized to one second:

$$\mathrm{SEL} = 10\log_{10}\left[\frac{1}{t_1}\int_0^{t_f} 10^{\frac{L_A(t)}{10}}\,dt\right] \tag{2.20}$$

where L_A is the A-weighted sound level, t_f the total exposure time and t_1 the reference time (one second). For a visual representation of SEL, see Fig. 2.9.

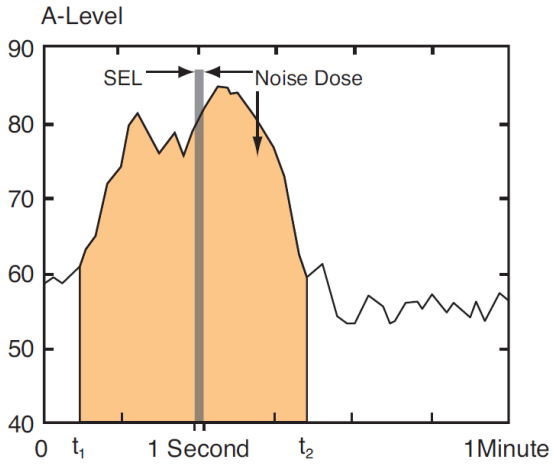

Figure 2.9: The sound exposure level [3]

To determine the SEL (dB) at a given location, i.e., the aircraft flyover noise at a location, multiple noise models have been developed. However, the Integrated Noise Model (INM) will be used in this study, since it was designed by the Federal Aviation Administration (FAA) and is seen as a standard tool for noise impact assessments [9]. The tool itself requires a trajectory represented as a sequence of straight segments with finite length in three dimensions (See Fig. 2.10). Next to the position, it also needs the airspeed and the net corrected thrust for each segment. For a specific observer location, INM uses the Noise-Thrust-Distance (NTD) table to determine the corresponding sound level. The noise exposure levels in the NTD database are based on infinite long segments directly flying over the observer with a constant airspeed of 160 kts, for multiple aircraft types. To correct the noise values in the database, several adjustments are applied. Based on the geometry of the flight segment relative to the observer, a noise-fraction adjustment is applied to accommodate for the finite length segments. To account for non-reference airspeeds, the duration time is adjusted. Finally, a lateral attenuation adjustment is taken into account for observer points located astride from the flight path. So, the output of the INM will be the SEL values caused by a defined finite trajectory on a specified grid of observer points.

2.4.2. NOISE IMPACT

With the use of INM, the sound exposure level experienced at an observer can be predicted. However, impact needs to be defined as a single objective criterion to be able to be used in a (multi-objective) optimization. A possible approach to accomplish this is to determine the number of awakenings for near-airport communities caused by a single night time fly over. The relationship between the percentage of people that wake up and the aircraft noise was initially proposed by the Federal Interagency Committee on Aviation Noise (FICAN) in [3]. However, in 2008 the American National Standards Institute (ANSI) [2] proposed a new criterion which is defined as follows:

$$\mathrm{P_{Awak}} = \frac{1}{1+e^{-(-6.8884+0.04444\mathrm{SEL_{indoor}})}} \tag{2.21}$$

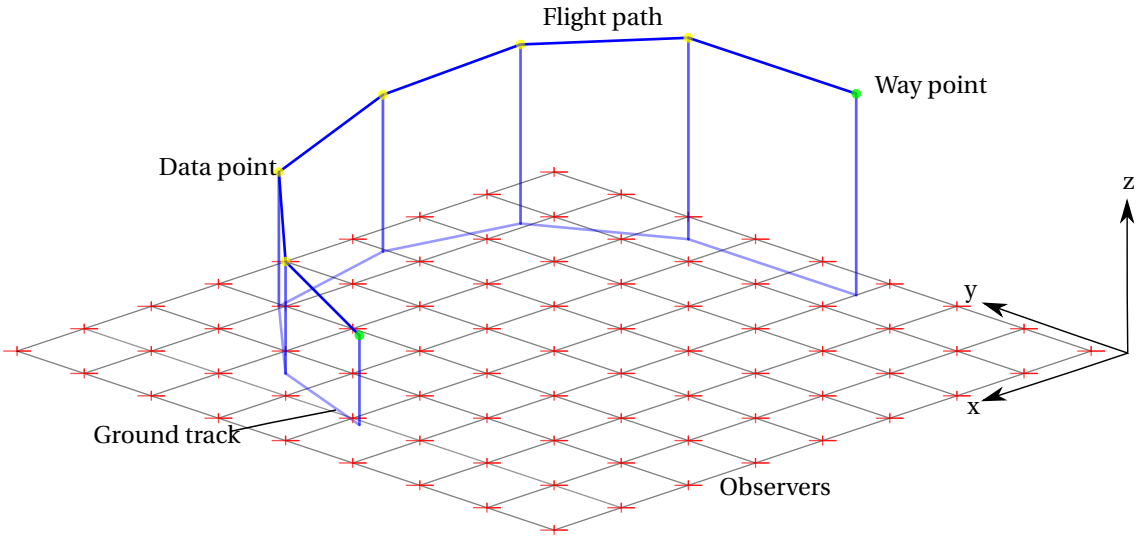

Figure 2.10: Schematic view of the required input for the integrated noise model.

As can be seen, the SEL values received indoors is required to determine the percentage of awakening, while INM determines the SEL outdoors. To estimate the SEL_{indoor}, 15 dB is subtracted from the $SEL_{outdoor}$. The total number of awakenings is then determined with the population density data received from the Geographic Information System (GIS). Here, the population density extracted for the grid observer points.

3

Modeling Method

This chapter will discuss the methods used to model departure trajectories and their environmental impact, so each trajectory can be evaluated in the optimization algorithm. First, the model to simulate the aircraft equations of motions is discussed. Secondly, it is explained how a trajectory is defined and which parameters are required. How the environmental impact of a trajectory is determined will also be explained in this chapter. Finally, how all these models are used together in the optimization framework will be clarified.

3.1. Aircraft Model

To determine the impact of a trajectory, several aircraft states will have to be simulated. For the modeling of the aircraft states during terminal procedures, this thesis will use an intermediate point-mass model [10]. With in mind that the model will be used in an optimization environment, it will be preferable to limit the complexity of the model as much as possible. Therefore, the simulation will be done in a 2-dimensional space, namely the distance flown $s(t)$ and the altitude $h(t)$. Next to the 2D position of the aircraft, the equivalent airspeed $V_{\text{EAS}}(t)$ is required to determine the noise impact for a departure trajectory. Finally, the aircraft weight $W(t)$ will be a required for the calculation of other states and the determination of the emission impact.

To limit complexity, several assumptions were made for this model: there is no wind present (1) the Earth is flat and non-rotating (2) the flight is coordinated (3) and the flight path angle is considered sufficiently small ($\gamma < 15\,\text{deg}$) (4). Additionally, for this intermediate model it is assumed that there is an equilibrium present for the forces normal to the flight path. With these assumptions taken into account, the equations of motion for the required states can be represented by a set of ordinary differential equations (ODE):

$$\frac{\mathrm{d}s}{\mathrm{d}t} = V_{\text{EAS}}\sqrt{\frac{\rho}{\rho_0}}\cos(\gamma) \tag{3.1}$$

$$\frac{\mathrm{d}h}{\mathrm{d}t} = V_{\text{EAS}}\sqrt{\frac{\rho}{\rho_0}}\sin(\gamma) \tag{3.2}$$

$$\frac{\mathrm{d}V_{\text{EAS}}}{\mathrm{d}t} = \left\{ g_0\left[\frac{T-D}{W} - \sin(\gamma)\right] + \frac{1}{2\rho}\frac{\partial\rho}{\partial h}V_{\text{TAS}}^2\sin(\gamma)\right\}\sqrt{\frac{\rho}{\rho_0}} \tag{3.3}$$

$$\frac{\mathrm{d}W}{\mathrm{d}t} = -\dot{m}_{\text{f}}g_0 \tag{3.4}$$

where the equivalent airspeed follows from;

$$V_{\text{EAS}} = V_{\text{TAS}}\sqrt{\frac{\rho}{\rho_0}} \tag{3.5}$$

In Eq. 3.3, $\frac{\partial \rho}{\partial h}$ is the derivative of the ambient air density with respect to the altitude and is determined form the standard atmosphere. The trust T, drag D and the fuel mass flow $\dot{m}_f$ used in Eq. 3.4 are a result of an aircraft specific model.

The states in this mode are now time dependent, which would mean that they have to be integrated over time. For a predefined trajectory which is required to be simulated, the end time t_f is not known beforehand. However, as will be demonstrated in Sec. 3.2, the total distance flown s_f can be determined. Therefore, to solve the set of ordinary differential equations, they have to be rewritten so that they are dependent of the distance flown. This can be done in the following way:

$$\frac{\mathrm{d}}{\mathrm{d}s} = \frac{\mathrm{d}}{\mathrm{d}t} \cdot \frac{\mathrm{d}t}{\mathrm{d}s} \tag{3.6}$$

By multiplying with the inverse of $\frac{\mathrm{d}s}{\mathrm{d}t}$,the ODEs can now be solved in steps of $\mathrm{d}s$. This is done with an adjusted Fourth Order Runge-Kutta method. Let the set of ordinary differential equations together be denoted as follows:

$$\frac{\mathrm{d}\bar{\mathbf{y}}}{\mathrm{d}s} = \left[\frac{\mathrm{d}t}{\mathrm{d}s}, \frac{\mathrm{d}h}{\mathrm{d}s}, \frac{\mathrm{d}V_{\mathrm{EAS}}}{\mathrm{d}s}, \frac{\mathrm{d}W}{\mathrm{d}s}\right]^{\mathrm{T}} = f(s, \bar{\mathbf{y}}) \tag{3.7}$$

with the initial conditions:

$$\bar{\mathbf{y}}(s_0) = \bar{\mathbf{y}}_0 \tag{3.8}$$

For a selected step size $\mathrm{d}s$, the solution is approximated with the previous solution plus the weighted average of four increments:

$$\bar{\mathbf{y}}_{n+1} = \bar{\mathbf{y}}_n + \frac{1}{6}(k_1 + 2k_2 + 2k_3 + k_4) \tag{3.9}$$

with the increments:

$$\begin{aligned} k_1 &= \mathrm{d}s \cdot f\left(s_n, \bar{\mathbf{y}}_n\right) \\ k_2 &= \mathrm{d}s \cdot f\left(s_n + \tfrac{\mathrm{d}s}{2}, \bar{\mathbf{y}}_n + \tfrac{k_1}{2}\right) \\ k_3 &= \mathrm{d}s \cdot f\left(s_n + \tfrac{\mathrm{d}s}{2}, \bar{\mathbf{y}}_n + \tfrac{k_2}{2}\right) \\ k_4 &= \mathrm{d}s \cdot f\left(s_n + \mathrm{d}s, \bar{\mathbf{y}}_n + k_3\right) \end{aligned} \tag{3.10}$$

This step size $\mathrm{d}s$, or the number of steps for specified distance, will be user selected. Naturally, a smaller step size will results in better accuracy, but also higher computational cost.

To solve the equations of motion for a segment of s, two control input variables are required: the flight path angle γ and the thrust setting η which will follow from the vertical trajectory (3.2.2).

3.2. TRAJECTORY

To simulate the aircraft states with the previous stated model, the trajectory of the aircraft had to be described. To again reduce the computational time of the model, Hartjes and Visser [10] introduced a novel trajectory parameterization technique. This technique decomposes the trajectory in a horizontal and vertical track. By this decoupling, the number of parameters to define a trajectory will be decreased without compromising the accuracy or the degrees of freedom. An other advantage of this technique is that it can handle the operational constrains in the problem formulation. Both these characteristics will reduce the computational cost significantly. First the parameterization for the ground track will be explained and secondly the approach for the vertical profile.

3.2.1. HORIZONTAL TRAJECTORY

The ground tracks considered in this thesis will be composed of two types of legs: track-to-a-fix (TF) and radius-to-a-fix (RF) legs. This is based on the requirements from the RNP/RNAV system, which consists of these types of legs due to their ability to minimize flight track spreading and avoid noise-sensitive areas. A ground track will therefore be generated of segments of straight flight legs or constant radius turns. An example can be found in Fig. 3.1, where a departure is plotted consisting of three TF legs and two RF legs. Since

the initial position (x_0, y_0) and the final position at a waypoint (x_f, y_f) are known, only five optimal design $(L_1, R_2, \Delta\chi_2, L_3, R_4)$ variables are required to compute the complete ground track. The remaining parameters $\Delta\chi_4$ and L_5 can be determined through a geometric calculation, shown in this section. When all the segments are known, the 3-dimensional position (x, y, h) and the heading angle χ for the complete trajectory can be determined, which will be required for future calculations.

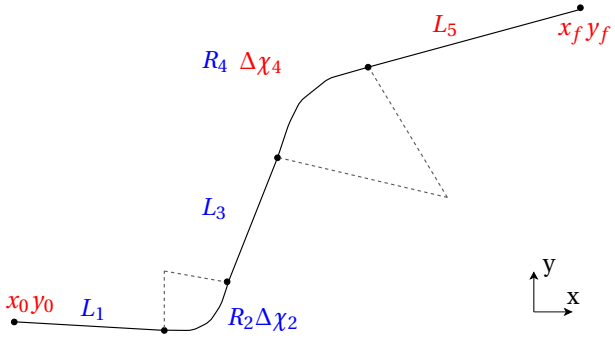

Figure 3.1: Schematic view of a departure, consisting of 3 TF legs and 2 RF legs.

The initial position (x_0, y_0) and heading χ_0 for a SID are set by the runway and since the first three legs are given, the position at point 3 can be calculated. First, determine the position at the end of the first TF segment:

$$\begin{aligned} x_1 &= x_0 + \sin(\chi_0) L_1 \\ y_1 &= y_0 + \cos(\chi_0) L_1 \end{aligned} \tag{3.11}$$

With the heading change in second segment $\Delta\chi_2$ and the radius of the turn R_2 known, the position of the turn center C_1 can be calculated:

$$\begin{aligned} x_{C_1} &= x_1 + \sin(\chi_1 + \alpha) R_2 \\ y_{C_1} &= y_1 + \cos(\chi_1 + \alpha) R_2 \end{aligned} \tag{3.12}$$

with $\chi_1 = \chi_0$ due that the first leg is a straight flight and $\beta_1 = +90°$ when the turn is to the right $(\Delta\chi_2 > 0)$ and $\beta_1 = -90°$ when the turn is to the left $(\Delta\chi_2 < 0)$. The position of the end of the second segment is determined as follows:

$$\begin{aligned} x_2 &= x_{C_1} + \sin(\chi_1 + \Delta\chi_2 - \beta_1) R_2 \\ y_2 &= y_{C_1} + \cos(\chi_1 + \Delta\chi_2 - \beta_1) R_2 \end{aligned} \tag{3.13}$$

The heading of the third leg is determined with the initial heading and the heading change in the first turn:

$$\chi_3 = \chi_1 + \Delta\chi_2 \tag{3.14}$$

and the position of the end of the third (TF) leg is determined by:

$$\begin{aligned} x_3 &= x_2 + \sin(\chi_3) L_3 \\ y_3 &= y_2 + \cos(\chi_3) L_3 \end{aligned} \tag{3.15}$$

Now, to determine if the second turn should be to the left or to the right, the heading of leg 2−3 and the virtual heading between point 2 and the final point f are compared. Three scenarios could occur:

- if $\chi_{23} > \chi_{2f}$: $\Delta\chi_4$ is positive, right turn
- if $\chi_{23} < \chi_{2f}$: $\Delta\chi_4$ is negative, left turn
- if $\chi_{23} = \chi_{2f}$: $\Delta\chi_4 = 0$, no turn required

See Fig. 3.2 for a illustration of the right and left turn scenarios.

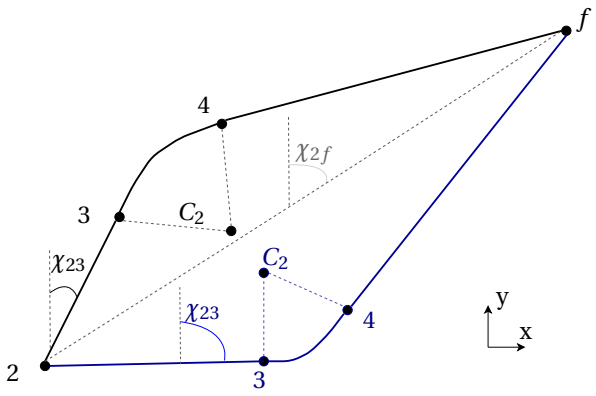

Figure 3.2: Schematic view of the scenarios where positive, right turn is required (black) and where a negative, left turn is required (blue).

To calculate the remaining optimal variables $\Delta\chi_4$ and L_5, the position of the center of the second turn C_2 needs to be determined first:

$$\begin{aligned} x_{C_2} &= x_3 + \sin(\chi_3 + \beta_2)R_4 \\ y_{C_2} &= y_3 + \cos(\chi_3 + \beta_2)R_4 \end{aligned} \tag{3.16}$$

where $\beta_2 = +90°$ for a positive turn and $\beta_2 = -90°$ for a turn to the left. Now, the distance from C_2 to f can be determined with the distance formula, derived from the the Pythagorean Theorem:

$$d(A,B) = \sqrt{(x_A - x_B)^2 + (y_A - y_B)^2} \tag{3.17}$$

If $d(C_2, f)$ is smaller than the turn radius R_4, the suggested ground track can not reach the final way point and is therefore not feasible. If it is greater or equal, point f can be reached.

To calculate $\Delta\chi_4$, two scenarios have to be identified: one where $\Delta\chi_4 \leq 90°$ (Fig. 3.3 left) and where $\Delta\chi_4 > 90°$ (Fig. 3.3 right). Since at this point, it is not yet known which scenario is true, the first scenario ($\Delta\chi_4 \leq 90°$) is assumed, so:

$$\Delta\chi_4 = \angle 3C_2 f - \angle 4C_2 f \tag{3.18}$$

where $\angle 4C_2 f$ can be determined with the tangent function, and $\angle 3C_2 f$ can be calculated with the Cosine-rule in triangle $\triangle 3C_2 f$. Here, $d(3, f)$ can be calculated with Eq. 3.17 and $d(3, C_2)$ is equal to the turn radius R_4.

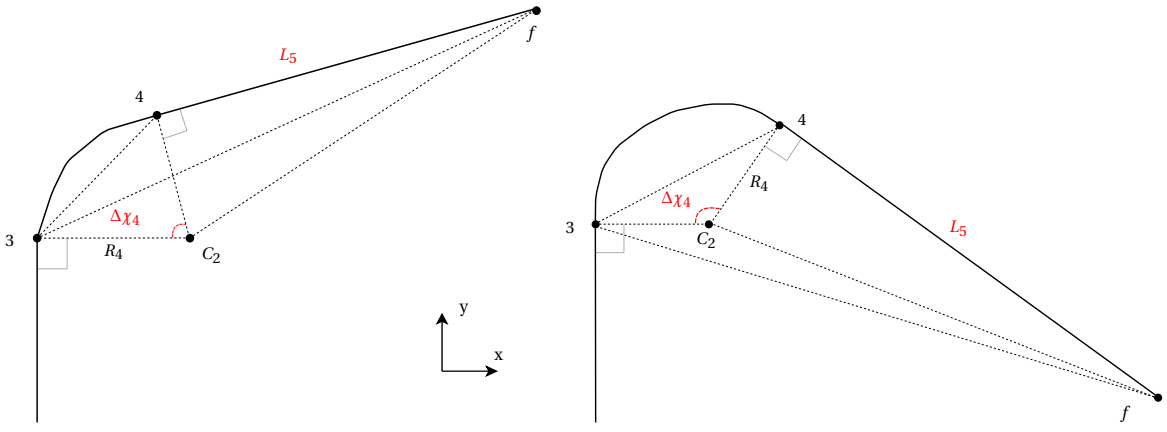

Figure 3.3: Schematic view of the scenario where $\Delta\chi_4 < 90°$ (left) and where $\Delta\chi_4 \leq 90°$ (right).

With $\Delta\chi_4$ known, the position of point 4 can be determined as follows:

$$\begin{aligned} x_4 &= x_{C_2} + \sin(\chi_3 + \Delta\chi_4 - \beta_2)R_4 \\ y_4 &= y_{C_2} + \cos(\chi_3 + \Delta\chi_4 - \beta_2)R_4 \end{aligned} \tag{3.19}$$

To check if the first scenario ($\Delta\chi_4 \leq 90°$) is correctly assumed, the angle between lines C_2-4 and $4-f$ should be perpendicular. If this is not the case, $\Delta\chi_4$ is larger than 90° and should be calculated as follows:

$$\Delta\chi_4 = 180° - \angle 3C_2f - \angle 4C_2f \tag{3.20}$$

The position of point 4 should be recalculated with Eq. 3.19 for the new $\Delta\chi_4$. With (x_4, y_4) and (x_f, y_f) known, L_5 can be determined since it is equal to $d(4, f)$ with the distance formula:

$$L_5 = d(4,f) = \sqrt{(x_4 - x_f)^2 + (y_4 - y_f)^2} \tag{3.21}$$

If the turn would be to the left, the calculations would be the same with $\beta = -90°$.

Since the equations of motion only include the 2D position of the aircraft, the x- and y-coordinates and the heading angle at every integration step had to be determined. For the first straight leg L_1, the coordinates are calculated as follows:

$$\begin{aligned} x_i &= x_0 + \sin(\chi_i)s_i \\ y_i &= y_0 + \cos(\chi_i)s_i \end{aligned} \tag{3.22}$$

with $\chi_i = \chi_1$ for the complete segment, since it is a TF leg.

For the second leg, which is a turn with a fixed radius, the heading angle and the coordinates have to be determined for each integration step:

$$\chi_i = \chi_1 + \frac{s_i - L_1}{R_2} \tag{3.23}$$

$$\begin{aligned} x_i &= x_{C1} + \sin(\chi_i - \alpha)R_2 \\ y_i &= y_{C1} + \cos(\chi_i - \alpha)R_2 \end{aligned} \tag{3.24}$$

with (x_{C1}, y_{C1}) are the coordinates of the center of the turn circle and α is equal to ±90°, depending if the turn is to the left or right.

For the third leg L_3, the x- and y-coordinates are determined with the same principle as in the first leg:

$$\begin{aligned} x_i &= x_2 + \sin(\chi_i)s_i \\ y_i &= y_2 + \cos(\chi_i)s_i \end{aligned} \tag{3.25}$$

with $\chi_i = \chi_3$ for the entire segment.

For the second turn of the trajectory, the same method is applied as for the first turn:

$$\chi_i = \chi_3 + \frac{s_i - (L_1 + L_2 + L_3)}{R_4} \tag{3.26}$$

$$\begin{aligned} x_i &= x_{C2} + \sin(\chi_i - \beta)R_4 \\ y_i &= y_{C2} + \cos(\chi_i - \beta)R_4 \end{aligned} \tag{3.27}$$

where $L_2 = R_2\Delta\chi_2$ and (x_{C2}, y_{C2}) are the coordinates of the center of the second turn circle. If the turn is to the right (positive), $\beta = +90°$, otherwise $\beta = -90°$.

For the final segment L_5, the coordinates at each integration step are calculated as follows:

$$\begin{aligned} x_i &= x_4 + \sin(\chi_i)s_i \\ y_i &= y_4 + \cos(\chi_i)s_i \end{aligned} \tag{3.28}$$

where χ_i is equal to χ_5 for the entire leg, which is determined by:

$$\chi_5 = \chi_3 + \Delta\chi_4 \tag{3.29}$$

In the end, the lateral position and heading of the aircraft over the complete trajectory can be determined, without being included in the equations of motion. By applying this approach, the complexity and computational cost of the aircraft model is reduced, while acquiring all the required input for further calculations.

3.2.2. VERTICAL TRAJECTORY

The vertical profile is based on the standard procedures from ICAO [19] and is divided in N segments. For the entire trajectory, there are performance requirements present which depend on the varying state variables of the aircraft and are therefore not constant. The flight procedures derived from ICAO present some operational constrains. For instance, during departure the aircraft is not allowed to descend ($\dot{h} \geq 0$) nor to decelerate ($\dot{V}_{\text{EAS}} \geq 0$). To ensure that the vertical profile is still feasible and can directly be implemented in the optimization, parameterization is applied. For each segment, there are two control inputs: flight path angle γ_i and trust T_i. However, because these variables will not remain constant over an entire segment, the control inputs are normalized. These normalized parameters will be the optimal design variables for the vertical trajectory and determine the actual control inputs. This will be required to be done at each integration step, since the states of the aircraft will vary. For each integration step, the control inputs are determined by adjusting the normalized parameters $\gamma_{n,i} (0 \leq \gamma_{n,i} \leq 1)$ and $\eta_{n,i} (0 \leq \eta_{n,i} \leq 1)$ as follows:

$$\gamma_i = \left(\gamma_{\text{max},i} - \gamma_{\text{min},i}\right) \gamma_{n,i} + \gamma_{\text{min},i} \tag{3.30}$$

$$T_i = \left(T_{\text{max},i} - T_{\text{min},i}\right) \eta_{n,i} + T_{\text{min},i} \tag{3.31}$$

where the subscript $_{max,i}$ and $_{min,i}$ represent the maximum and minimum allowed values for that integration step, based on the operational requirements. For the entire trajectory, these maximum and minimum values will have to be determined, since they are dependent on the state variables of the aircraft. For this ICAO regulated departure, the aircraft is not allowed to descend, so $\gamma_{\text{min},i}$ is set to zero. The maximum climb thrust were no declaration is occurring is determined with the aircraft specific model and is set as $T_{\text{max},i}$. With the assumption that the airspeed is maintained constant and $\gamma_{\text{max},i}$ is already selected, $\gamma_{\text{max},i}$ can be determined with Eq. 3.3:

$$\gamma_{\text{max}} = \sin^{-1}\left[\frac{-2\rho g_0 \left(T_{\text{max}} - D\right)}{W\left(\frac{\partial \rho}{\partial h} V_{\text{TAS}}^2 - 2\rho g_0\right)}\right] \tag{3.32}$$

Finally, $T_{\text{min},i}$ can be determined by the given fact that when flying at a climb angle, the aircraft should maintain its airspeed. Therefore, the minimum thrust at each step is determined as follows:

$$T_{\text{min}} = D - \frac{W}{2\rho g_0} \frac{\partial \rho}{\partial h} V_{\text{TAS}}^2 \sin(\gamma) + W \sin(\gamma) \tag{3.33}$$

Now, the upper and lower bound for the two control parameters can be determined over the entire trajectory, therefore ensuring its feasibility. The bounds however can get overruled when the aircraft reaches the exit conditions of the departure. When the altitude of the aircraft is equal of higher than the final altitude h_{final}, the normalized climb angle $\gamma_{n,i}$ will be set to zero and therefore the actual climb angle γ_i will be zero. If the aircrafts airspeed reaches the final velocity $V_{\text{EAS},final}$, the normalized thrust setting will be set to zero. This will results the thrust of the aircraft will be equal to T_{min} and therefore will not accelerate anymore.

3.3. ENVIRONMENTAL IMPACT

With a complete trajectory defined and simulated, the environmental impact can be modeled. The noise can be estimated with the use of the INM. For this thesis, a replication will be used, named INMTM v3.0, which calculated the noise exposure on a user-defined grid [5]. The input required for this model is the position of the aircraft (x, y, h), the velocity (V_{TAS}) and the net corrected thrust (T_{net}) at specific points along the trajectory. The net corrected thrust is the thrust one eninge would generate at sea level for a given engine setting η_i:

$$T_{net} = \frac{T_i}{n_{eng}} \frac{P}{P_0} \tag{3.34}$$

where T_i is the thrust at point i, n_{eng} is the number of engines the aircraft has and $\frac{P_0}{P}$ is the air pressure ratio between at sea level and the ambient air pressure. The output of the noise model is the sound exposure level (SEL) for each point at the specified grid.

To reduce the computational cost of the noise simulation, it is possible to reduce the number of data points from the input. This is due to the fact that the INM model works with segments of trajectories, see Sec. 2.4. When the states of the segments do not change that rapidly, mostly at the end of a departure trajectory, less data points are required to do the noise calculations with a similar accuracy. For the first two segments (the first TF and RF), the number of data points are not reduced, because the legs are relatively short. For the second TF and RF, only half of the data points are considered. This is due the fact the aircraft states vary less than in the first two legs. For the final leg (last TF), only a third of the data points are considered. In most cases, the final altitude and airspeed are reached in the beginning of this leg, so longer segments will generate the same result. How much the computational cost is reduced varies for each trajectory, because the data points can be divided differently over the legs. However, the cost will be reduced significantly for each trajectory.

To estimate the noise impact, a criterion function by the ANSI is used to determine the percentage of awakenings for given SEL [2], see Eq. 2.21. Here, $\text{SEL}_{\text{indoor}}$ is indoor sound exposure level in decibel and is equal to the outdoor simulated SEL minus 15 dB. SEL values lower than 50 dB are ignored and their probabilities are set to zero. With the use of geographic information system (GIS), which provides the population density at the specified grid, the number of awakenings can be determined.

The amount of fuel consumed per trajectory can be derived from the aircraft weight, see Eq. 3.4. The total amount of fuel burnt m_f is assumed to be equal to the difference between the initial weight and the final weight of the aircraft.

3.4. OPTIMIZATION FRAMEWORK

A trajectory solution can now be described with a set of $6+2N$ optimization design variables: 5 for the ground track, 1 for the first decision altitude, N different climb angles and N trust settings:

$$\text{Solution} = \left[\bar{\mathbf{x}}, h_1, \gamma_1, ..., \gamma_n, \eta_1, ..., \eta_n\right]^{\text{T}} \tag{3.35}$$

where $\bar{\mathbf{x}}$ represent the set of the ground track variables.

The impact corresponding to a trajectory is now described as the total number of awakenings (Awak) and the total amount of fuel burnt (Fuel). Those will be the objective criteria for this optimization problem. Although some constraints were covered with use of the parameterization technique, three more will be considered. There is a maximum allowed bank angle μ_{max}, which is specified by ICAO [19]. Also, the final altitude h_{final} and velocity $V_{\text{EAS, final}}$ are prescribed by the flight procedures. Combining all, the multi-objective optimization problem can be formulated as:

$$\begin{aligned} \min_{\bar{\mathbf{x}},\gamma_{\mathbf{n}},\eta_{\mathbf{n}}} : \quad & \{\text{Awak}, \text{Fuel}\} \\ \text{s.t.} \quad & \mu \leq \mu_{\text{max}} \\ & h_{\text{f}} = h_{\text{final}} \\ & V_{\text{EAS,f}} = V_{\text{EAS, final}} \end{aligned} \tag{3.36}$$

Here, the number of awakenings and the amount of fuel consumed are both minimized for a set of optimal values, where $\bar{\mathbf{x}}$ is the vector of the track variables, γ_n is the set of normalized flight path angle settings and η_n the set containing the trust settings for each segment. The bank angle μ for each integration step follows from the defined ground track and is calculated with this equation:

$$\mu = \pm \tan^{-1}\left(\frac{V_{\text{TAS}}^2}{g_0 R}\right) \tag{3.37}$$

To solve this multi-objective optimization problem, an adjusted version of the MOEA/D presented in Sec. 2.2.3 will be used. New implementations are introduced to reduce the computational cost of the algorithm. This cost is mainly spent on (1) the simulation the trajectory and so evaluating the fuel objective function and generating the input for the noise model, (2) on determining the noise impact and so evaluating the noise objective function and (3) evaluating the constrains of the optimization problem. While for the first task its computational cost is not significant and the cost for the last is already reduced with the use of the parameterization technique, for the second task it is quite considerable. To reduce the computation time, the following scenarios were identified where a suited adjustment could be implement:

- In the ground track calculation, it is checked if the track obtained from $\mathbf{x}$ is a feasible. This is done by checking if $d(C_2, f) > R_4$. If not, both the trajectory simulation and the noise calculation are not executed.
- When the trajectory of a solution is simulated and it violates the constraints set in Eq. 3.36, while the solution of its previous generation was feasible, the algorithm will not execute the noise calculations.
- When both the previous solution and the new one are infeasible, the level of constraint violation is compared. When the new one is at a higher level, the noise calculations will not be executed.

With these implementations, the computational cost of the optimization algorithm is spent on either feasible solutions or solutions that are infeasible, but have the lowest level of constraint violation. In that way, together with the parameterization technique (3.2) and the data point reduction for the noise model imput (3.3), the total required time of the optimization will be reduced significantly.

4

STOCHASTIC MODEL

Next to the deterministic model that was presented in Ch. 3, an additional stochastic model will be used to simulate the uncertainty of certain state variables. In this chapter the focus will be mainly on the simulation of the lateral position error. First, the stochastic model will be presented, which will be used in the Monte Carlo simulation. Secondly, how the overall noise impact will be determined as a result of this simulation will be explained. With in mind that the stochastic analysis should also be taken into account within the optimization, a method is developed to approximate the stochastic noise impact. In the next section it will be discussed how this stochastic analysis of the noise impact will be implemented in the optimization framework. Finally, a similar approach will be presented to model the initial weight deviation and how this could be used in the optimization.

4.1. SIMULATION MODEL

As was stated in Sec. 2.1, even with the modern RNP/RNAV used, there still exists a lateral position error during the terminal procedures of a flight. Based on the RNP requirements and the characteristics of RNAV, the overall distribution of this error can be determined. To investigate the effect of the lateral deviation, that error will be simulated over the nominal flight track s derived from Eq. 3.1. The track consists of n amount of data points i, where an error ϵ_i has to be simulated. For this, three approaches have been identified.

The first approach is that a new error would be simulated for each data point, without taking into account the previous error:

$$\epsilon_{i+1} = 0 \cdot \epsilon_i + \phi \tag{4.1}$$

where ϕ is a random variable with a certain distribution, which would be a Gaussian in this case. The second approach would be the complete opposite of the previous approach, namely the same error for each data point:

$$\epsilon_{i+1} = \epsilon_i + 0 \cdot \phi \tag{4.2}$$

where the first error ϵ_1 is picked from the distribution ϕ and the error of all the upcoming data point would be equal to the initial one.

Although the overall error distribution of both approaches will be the same, there are some significant differences present. For the first approach, where the error on each data point is independent of previous errors, a lot of heading changes will occur. How big each change will be, depends on how far each data point is located from the next one and on the difference in lateral error between the two data points. In extreme cases, this would result in unrealistic trajectories with respect to performance. The second approach, where the lateral deviation is assumed constant over the complete trajectory, was also deemed to be not a suitable representation of the actual lateral position error. When analyzing radar data, it was clear that in most cases some heading changes due occur during terminal procedures and that the deviation from the nominal track is not constant.

Therefore, a third approach is identified to represent the lateral deviation where the error is simulated at certain waypoints along the trajectory, and the error at intermediate data points results from an interpolation. Along the track, a set of way-points k are selected, which are all located on a certain data point i. For these locations s_i^k with $i = 1,...,n$ represent the data points and $k = 1,...,m$ represent the waypoints, a lateral position error ϵ_i^k is denoted as follows:

$$\epsilon_{i+l}^{k+1} = 0 \cdot \epsilon_i^k + \phi \tag{4.3}$$

where $\phi \sim N(0, \sigma_\phi^2)$ is a random variable and l denotes the number of data points between waypoints k and $k+1$. This results in an independent error at each waypoint. The error for the remaining intermediate points will be determined with a cubic interpolation, to ensure the complete trajectory is continuous and smooth and no abrupt heading changes will occur. However, due to that a cubic interpolation method is used, a minimum of four waypoints is required. The selection of the waypoints is done in the following way:

- The initial position (x_0, y_0) is selected as the first waypoint
- The last data point of a RF segment is selected as waypoint
- The final position (x_f, y_f) is selected as the last waypoint
- When a TF leg is longer than 20 km, the data point half way the leg is selected as additional waypoint

Since the departures considered in this study always consist of two turn segments, it is guaranteed that there will be at least four waypoint selected on every trajectory.

In addition to just simulating the error on a selection of waypoints, an smoothing factor α is applied. By partially taking into account the previous error, unrealistic large heading changes can be prevented. The lateral position error ϵ_i^k is denoted as follows:

$$\epsilon_{i+l}^{k+1} = \alpha \epsilon_i^k + (1-\alpha)\phi \tag{4.4}$$

with $\alpha \in [0,1]$ the smoothing factor, $\phi \sim N(0, \sigma_\phi^2)$ is a random variable and l denotes the number of data points between waypoints k and $k+1$. See Fig. 4.1 for a schematic illustration of the lateral position error.

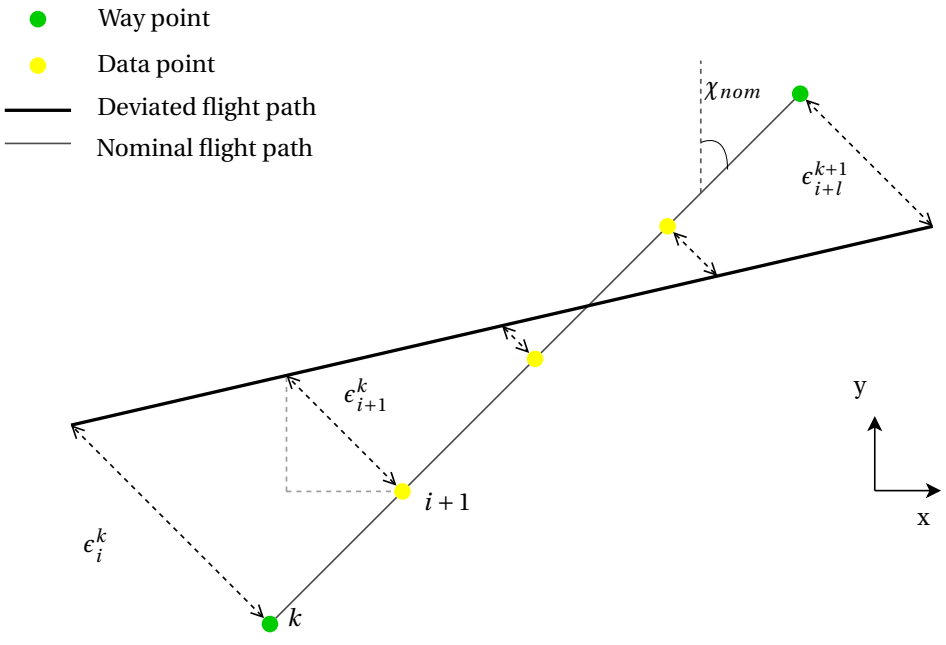

Figure 4.1: Lateral Position Error

For this model, the initial error ϵ_1^1 is set to zero. The variance of stochastic variable ϕ results from the RNP requirements and the smoothing factor α. Assuming that the variance of the overall lateral position error should be equal to the variance according to the RNP, the variance of ϕ is determined as follows:

$$\begin{array}{rcl} \mathrm{Var}\left[\epsilon_{i+l}^{k+1}\right] & = & \sigma_{\mathrm{RNP}}^2 \\ \mathrm{Var}\left[\epsilon_{i+l}^{k+1}\right] & = & \mathrm{Var}\left[\alpha\epsilon_i^k + (1-\alpha)\phi\right] \\ \sigma_{\mathrm{RNP}}^2 & = & \alpha^2\sigma_{\mathrm{RNP}}^2 + (1-\alpha)^2\sigma_\phi^2 \\ \sigma_{\mathrm{RNP}}^2(1-\alpha^2) & = & (1-\alpha)^2\sigma_\phi^2 \end{array} \tag{4.5}$$

which results in that standard deviation of ϕ can be determined as follows:

$$\sigma_\phi = \sigma_{\mathrm{RNP}}\sqrt{\frac{(1-\alpha^2)}{(1-\alpha)^2}} \tag{4.6}$$

Since the lateral position error is defined as perpendicular to the flight track, the error for the x and y components and so the new coordinates can be determined as follows:

$$\begin{array}{l} \hat{x}_i = x_{nom,i} + \epsilon_i \cos(\chi_i) \\ \hat{y}_i = y_{nom,i} + \epsilon_i \sin(\chi_i) \end{array} \tag{4.7}$$

where the nominal positions coordinates x_{nom} and y_{nom} and the heading angle χ_i are obtained with the approach presented in Sec. 3.2. To compute a deviated trajectory, a set of m amount of errors has to be generated, corresponding to the m number of waypoints selected along the trajectory. The errors for intermediate data points are computed as a result of a cubic interpolation. The deviated 2D positions $\hat{x}_i$ and $\hat{y}_i$, together with the altitude, airspeed and thrust profile of the nominal track will be the input for the noise model.

Based on the literature reviewed in Sec. 2.1, it is assumed that the lateral position error distribution is Gaussian with a zero mean $N(0, \sigma_{\mathrm{RNP}}^2)$. The standard deviation of that distribution is based on the required navigation performance. According to the Performance Based Navigation specifications of Schiphol Airport [18] a RNP of ±1 is required during the arrival and departure phase. A RNP ±1 means the aircraft is allowed to deviate for 95 per cent of the time 1 NM to the left and 1 to the right. For a two-tailed 95% confidence interval, the Z-score is equal to $Z_{0.95} \approx 2$, so 2 standard deviations. Therefore, the standard deviation for the lateral position error should be equal to a 0.5 NM (926 m). The lateral position error ϵ can now be simulated as a normal distribution $N(\mu_{\mathrm{RNP}}, \sigma_{\mathrm{RNP}}^2)$, with $\mu_{\mathrm{RNP}} = 0$m and $\sigma_{\mathrm{RNP}} = 926$m.

The effect on the noise impact caused by the lateral position error will be determined with the use of a Monte Carlo simulation. To determine how many samples needs to be simulated to obtain useful results, the Central Limit Theorem is used. With the use of the CLT, the sample size can be determined where the sample mean is located within a specified interval with a certain confidence level. As an example for a two tailed test, where the confidence level α corresponds to a certain Z-score value, the following is true:

$$\mathrm{P}\left(\bar{X}_N - Z_\alpha \frac{\sigma}{\sqrt{N}} \leq \mu \leq \bar{X}_N - Z_\alpha \frac{\sigma}{\sqrt{N}}\right) = \alpha \tag{4.8}$$

where the allowable error between the mean of the samples $\bar{X}_n$ and the mean of the distribution μ should satisfy the following statement:

$$\bar{X}_N - \mu > Z_\alpha \frac{\sigma}{\sqrt{N}} \tag{4.9}$$

If a defined error is allowed, the required sample size N can be determined to meet a certain confidence level as follows:

$$N > \left(\frac{Z_\alpha \sigma}{\bar{X}_n - \mu}\right)^2 \tag{4.10}$$

For a confidence level α of 95 %, the standard deviation of 926 meter and an allowed error equal to 5 % of that standard deviation, the required sample size for the Monte Carlo simulation should be approximately equal to 1500.

4.2. NOISE IMPACT

To determine the noise impact of a trajectory with a lateral position deviation, a Monte Carlo simulation is conducted with the stochastic model from Sec. 4.1. For every randomly generated trajectory, the INM model is used to determine the noise level. The noise level is computed for each grid point, as defined in 3.3. It is assumed that the thrust setting, altitude and airspeed profile of the trajectory of the deviated trajectories will be unchanged with respect to the nominal one. Therefore, only the x- and y-coordinates have to be re-generated for every stochastic simulation.

The difference with the deterministic noise impact calculations is that now for every grid point $g^{i,j}$ there is a set of N amount SEL data, instead of just a single SEL value. Since the lateral position error is represented as a normal distribution, it is assumed that the SEL is also normally distributed with different distribution parameters for each grid point. The mean, which equals the expected value, is determined by filling in Eq. 2.11 and results in:

$$\mu_{\mathrm{SEL}}^{i,j} = \mathrm{E}\left[\mathrm{SEL}^{i,j}\right] = \frac{1}{N}\sum_{k=1}^{N}\mathrm{SEL}_k^{i,j} \tag{4.11}$$

where N is the number of Monte Carlo simulation runs. The variance of the SEL at each grid point is determined by rewriting Eq. 2.12 into:

$$\left(\sigma_{\mathrm{SEL}}^{i,j}\right)^2 = \mathrm{Var}\left(\mathrm{SEL}^{i,j}\right) = \frac{1}{N}\sum_{k=1}^{N}\left(\mathrm{SEL}_k^{i,j} - \mu_{\mathrm{SEL}}^{i,j}\right)^2 \tag{4.12}$$

With the distribution of the SEL $N(\mu_{SEL}, \sigma_{SEL}^2)$ at each grid point $g^{i,j}$ known, the distribution of the number of awakenings can be estimated. Again, the criterion function from ANSI [2] is used to determine the percentage of awakenings for a given SEL, see Eq. **??**. To speed up the calculations, the SEL distribution is discretized in $q = 12$ segments. For each segment, an expected value $\mathrm{E}[X]_q$and probability $P(X)_q$ is defined, with $q = (1,2,...,12)$. The width of each segment is equal to 0.5 Z-score, or 0.5σ, for a range of $[-3,3]$. The segments $\langle-\infty,-3]$ and $[3,\infty\rangle$ are neglected, since their probability is assumed to be equal to zero. The probability for the remaining segments are determined with the use of Eq. 2.9:

$$P(X)_q = P\left(X_q - 0.25\sigma \leq X \leq X_q + 0.25\sigma\right) = \int_{X_q-0.25\sigma}^{X_q+0.25\sigma} f_X dx \tag{4.13}$$

The expected value for each segment is assumed to be equal to the value located in the center of each segment, so

$$\mathrm{E}[X]_q = X_q \tag{4.14}$$

For an example of a normal distribution which is discretized, see Fig. 4.2 .
After the discretization, there is now a set of 12 $\mathrm{SEL}_q^{i,j}$ values with corresponding probability $P(\mathrm{SEL}_q^{i,j})$ for every grid point $g^{i,j}$. To determine the distribution of the number of awakenings, the number of awakenings $\mathrm{Awak}_q^{i,j}$ corresponding to a discretized SEL value has to be calculated with the use of the percentage of awakenings and the population density at that grid point:

$$\mathrm{E}\left[\mathrm{Awak}\right]_q^{i,j} = \mathrm{P}_{\mathrm{Awak}}(\mathrm{SEL}_q^{i,j}) \cdot P(\mathrm{SEL}_q^{i,j}) \cdot \mathrm{pop}^{i,j} \tag{4.15}$$

The total expected number of awakenings per grid point is determined by summing the 12 segments:

$$\mathrm{E}\left[\mathrm{Awak}\right]^{i,j} = \sum_{q=1}^{12}\mathrm{E}\left[\mathrm{Awak}\right]_q^{i,j} \tag{4.16}$$

To determine the variance of the total number of awakenings, the following equation is used:

$$\mathrm{Var}\left(\mathrm{Awak}\right)^{i,j} = \frac{1}{12}\sum_{q=1}^{12}\left(\mathrm{Awak}_q^{i,j} - \mathrm{E}\left[\mathrm{Awak}\right]^{i,j}\right)^2 \tag{4.17}$$

For the variance of the total number of awakenings, it is required to determine first if the distributions of SEL at the different grid points are dependent or independent of each other. It is easily arguable that grid points

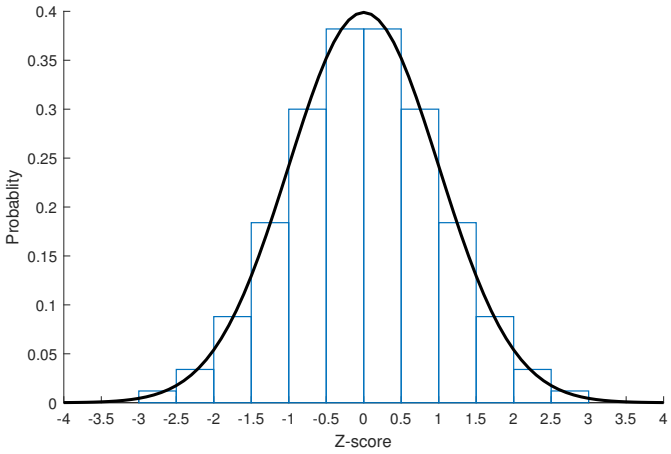

Figure 4.2: Continuous and discretized normal distribution

next to each other dependent on each other and grid points located at either side of the total grid are independent. A threshold distance is assumed, based on the RNP requirements, when grid points are independent or not. When the distance between two grid points is smaller than 2 NM (or 3704 m), the distributions of SEL are considered dependent of each other. This means that most grid points located in the same city are dependent, but points located in neighboring cities are not. The variance of the number of awakenings is determined with the use of the covariance matrix from Eq. 2.18. The total variance is then the sum of all the elements in the matrix:

$$\text{Var}(\text{Awak}) = \sum_{i=1}^{n} \text{Var}(\text{Awak}^{i,i}) + 2 \sum_{1 \le i < j < n} \text{Cov}(\text{Awak}^{i,j}, \text{Awak}^{i,j}) \tag{4.18}$$

When two grid points are considered to be independent, the element in the matrix Cov(Awak, Awak) = 0. Otherwise, the covariance of that element is calculated with Eq. 2.17. The corresponding expected total number of awakenings is just the sum of the expected awakenings across all grip points:

$$\text{E}[\text{Awak}] = \sum_{1 \le i < n} \sum_{1 \le j < n} \text{E}[\text{Awak}]^{i,j} \tag{4.19}$$

With this approach, the distribution of the number of awakenings can be estimated when the distribution of the SEL at each grid point is obtained.

4.3. APPROXIMATION FUNCTION

With the use of the Monte Carlo simulation, the variation of the noise impact caused by the lateral position deviation can be estimated. However, when this variation would be implemented in an evolutionary optimization algorithm, the computational cost of the entire process would increase significantly. Therefore, the same variation of the noise impact will be approximated with the use of the following 'approximation' function:

$$\sigma_{\text{SEL}}^{i,j} = f\left(d_i^{i,j}, h_i^{i,j}\right) \cdot C_{turn} \tag{4.20}$$

where $d_i^{i,j}$ denotes the minimum distance from a grid point to the flight track:

$$d_i^{i,j} = \min d\left(g^{i,j}, [x_i, y_i, h_i]^{\text{T}}\right) = \min \sqrt{\left(x^{i,j} - x_i\right)^2 + \left(y^{i,j} - y_i\right)^2 + \left(z^{i,j} - h_i\right)^2} \tag{4.21}$$

$h_i^{i,j}$ denotes the altitude of the track segment corresponding to the minimum distance between a grid point and the trajectory:

$$h_i^{i,j} = \min d\left(g^{i,j}, [x_i, y_i, h_i]^{\text{T}}\right) - \min d\left(g^{i,j}, [x_i, y_i]^{\text{T}}\right) = d_i^{i,j} - \min \sqrt{\left(x^{i,j} - x_i\right)^2 + \left(y^{i,j} - y_i\right)^2} \tag{4.22}$$

and C_{turn} represents the correction term which will be added when $d_i^{i,j}$ corresponds to a turn segment of the trajectory. This correction is determined with the following function:

$$C_{turn} = f\left(h_i^{i,j}, R_i, g^{i,j}\right) \tag{4.23}$$

Here, the $h_i^{i,j}$ is the altitude of the turn segment and R_i is the radius of the turn. $g^{i,j}$ is required to determine if the minimum $d\left(g^{i,j}, [x_i, y_i]^{\mathrm{T}}\right)$ corresponds to a turn segment and if the grid point $g^{i,j}$ is located inside or outside of the turn. To check if grid point is located in or outside of the turn, the distance to the turn center (x_C, y_C) has to be compared with the turn radius R_i. So when

$$d\left(g^{i,j}, [x_C, y_C]^{\mathrm{T}}\right) < R_i, \tag{4.24}$$

then $g^{i,j}$ is located inside of the turn. Otherwise, it is outside the turn.

In total, it is required to generate, by using the simulation, three data sets to apply the approximation function:

- a distance-altitude (d, h) table with σ_{SEL} data
- a radius-altitude $(R, h)_{in}$ table with C_{turn} correction factors, for points located inside the turn
- a radius-altitude $(R, h)_{out}$ table with C_{turn} correction factors, for points located outside the turn

These approximation tables will be generated with the use of Monte Carlo simulation of just a generic segment of a trajectory. The lateral position error on a straight level flight segment will be simulated at different altitudes. The σ_{SEL} values are determined at multiple distances from the nominal track and stored in separate column for each altitude. For a schematic overview of this table, see Tab. 4.1.

	1000 ft	1500 ft	h ⋯ h	6000 ft	6500 ft
0 m	8.041	6.913	σ_{SEL} ⋯ σ_{SEL}	3.124	2.771
250 m	8.039	6.911	σ_{SEL} ⋯ σ_{SEL}	3.124	2.770
d	σ_{SEL}	σ_{SEL}	σ_{SEL} ⋯ σ_{SEL}	σ_{SEL}	σ_{SEL}
⋮	⋮	⋮	⋮ ⋱ ⋮	⋮	⋮
d	σ_{SEL}	σ_{SEL}	σ_{SEL} ⋯ σ_{SEL}	σ_{SEL}	σ_{SEL}
39750 m	0.168	0.169	σ_{SEL} ⋯ σ_{SEL}	0.183	0.188
40000 m	0.169	0.168	σ_{SEL} ⋯ σ_{SEL}	0.181	0.187

Table 4.1: Look up table with σ_{SEL} for different altitudes h at different distances r.

For the turn correction, a segment of a turn will be simulated with different radii at multiple altitudes. The C_{turn} are stored in a table for locations at the inner side of the turn and for at the outer side of turn segment. In this table, the rows correspond to the different turn radii, while the columns represent different altitudes of the turn segment.

Due to that only the perpendicular distance to the segment is required, he grid with observer points will be just the points located on the cross section of the segment. See Fig. 4.3 for a schematic view of the setup for both simulations.

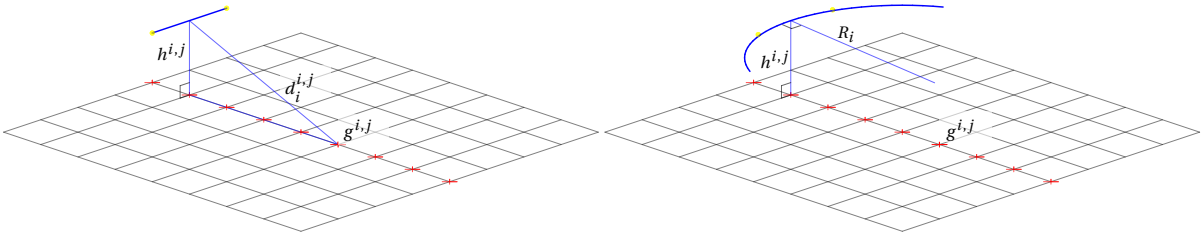

Figure 4.3: Schematic view of the set up for the straight segment simulation (left) and the turn segment simulation (right).

To conclude, the approximation function will consists of lookup tables and requires the minimum distance from a grid point to the flight track, the altitude of that corresponding altitude and the turn radius when the minimum distance is to a turn segment of the trajectory. Since the table only has discrete data, not all the required data will be included. The remaining data will be generated with the use of a linear interpolation. The data that was generated can only used when the same distribution of the lateral position error $N(0, \sigma^2_{\text{RNP}})$ is used. The output of the approximation function is the standard deviation of SEL ($\sigma^{i,j}_{\text{SEL}}$) over a specified grid. The mean of the SEL ($\mu^{i,j}_{\text{SEL}}$) is assumed to be equal to the SEL values obtained from the deterministic simulation. The further noise impact calculations is done with the same approach as presented in Sec. 4.2.

4.4. OPTIMIZATION IMPLEMENTATION

To take into account the effect of lateral deviation on the noise impact, the approximation function will be used to determine the distribution of the SEL for a specified grid. With Eq. 4.18 and Eq. 4.19, the distribution of the number of awakenings can be estimated. The input for the approximation function will be the lateral position x_i and y_i, the altitude h_i of the aircraft, the turn radius R_i, and the a specified grid of receiver points $g^{i,j}$. The output of the function will be the expected number of awakenings and its variance. The multi-objective optimization problem statement will have to be adjusted to:

$$\begin{aligned} \min_{\bar{\mathbf{x}},\gamma_{\mathbf{n}},\eta_{\mathbf{n}}}: \quad & \{\text{E}[\text{Awak}], \text{Fuel}\} \\ \text{s.t.} \quad & \mu \leq \mu_{\max} \\ & h_{\text{f}} = h_{\text{final}} \\ & V_{\text{EAS,f}} = V_{\text{EAS, final}} \end{aligned} \tag{4.25}$$

Due to that the variance of the number of awakenings is also known, the optimization can also be executed by taken into account the uncertainty of this number of awakenings. As an alternative objective criterion, the Z-score value of particular uncertainty level α could be used. This Z_α can be expressed with μ_{Awak} and σ_{Awak}, which both are already determined with Eq. 4.11 and Eq. 4.20. The optimization problem can then be formulated as:

$$\begin{aligned} \min_{\bar{\mathbf{x}},\gamma_{\mathbf{n}},\eta_{\mathbf{n}}}: \quad & \{Z^{\text{Awak}}_{\alpha}, \text{Fuel}\} \\ \text{s.t.} \quad & \mu \leq \mu_{\max} \\ & h_{\text{f}} = h_{\text{final}} \\ & V_{\text{EAS,f}} = V_{\text{EAS, final}} \end{aligned} \tag{4.26}$$

The constraints for both problems will remain unchanged with respect to the deterministic optimization problem.

4.5. WEIGHT ERROR MODEL

To investigate what the effect would be when other state variables show deviation from their nominal value, the stochastic behavior of the starting aircraft weight will be modeled. As can be seen in the equations of motion in Sec. 3.1, the weight state affects the velocity and so also the altitude state, which both considered not to be affected by the lateral navigation error. Therefore, by modeling an error for the starting weight, a possible variation of these other states can be simulated and its effect on the noise impact can be estimated.

The contributions to the total aircraft weight can divided in several categories. The Operating Empty Weight (OEW) consists of the aircraft structure, including the propulsion systems, on-board equipment and the crew. When the passengers and the cargo are added, it is called the Zero Fuel Weight (ZFW). The Maximum Take-Off Weight (MTOW) is when the trip and reserve fuel is added to the ZFW, see Fig. 4.4 for a simplified diagram. Although the components of the OEW are set, the payload (passengers and cargo) could easily vary and the amount of fuel is depending on that payload and the destination it has to reach. Therefore, the actual starting weight could have some deviation.
In the deterministic model, an initial mass for the aircraft is selected as a percentage of the MTOW, namely 85 %. In this stochastic model, a Gaussian distribution is assumed to represent the possible variation of this initial mass, with the 85 % MTOW as the average value. To ensure that the initial weight will ever exceed the MTOW and be significantly more than the OEW, the standard deviation is set equal to 3 % of the MTOW, as shown in Fig. 4.5.

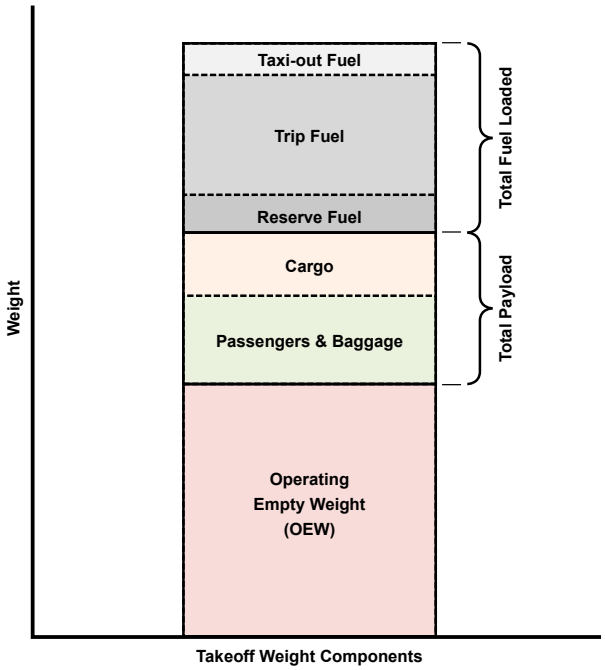

Figure 4.4: Takeoff weight diagram [23]

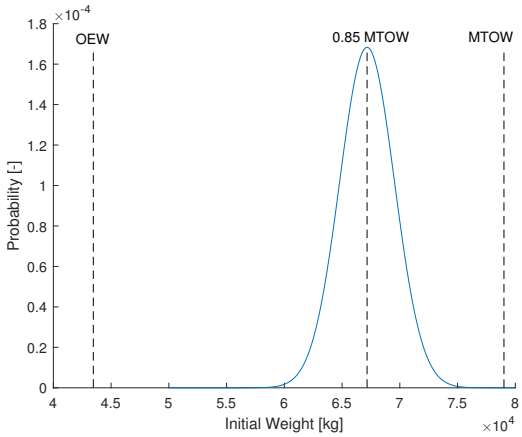

Figure 4.5: The initial weight distribution assumed, with the MTOW highlighted

Two of the main reasons to use a normal distribution for this model is to reduce the complexity and that the expected value is equal to the weight used in the deterministic model. It could be argued that the actual weight is distributed differently, but in this research the focus is more on how to use the stochastic behavior of a state variable in an optimization, rather than to perfectly model the actual distribution of that variable. Therefore for this research, a deeper analysis on how the starting weight is distributed is considered to be out of the scope and the focus will be on the methodology that is developed.

To determine the effect on the noise impact caused by the deviation of the initial aircraft weight, a Monte Carlo simulation will be set up. However, due to the fact that the initial weight W_0 affects multiple states, the complete trajectory has to be simulated for each drawn value. This is in contrast with the lateral position error model, where only the x- and y-position had to be redetermined. For this model, all states could be effected by a different starting weight and so have to be redetermined with the aircraft model presented in Sec. 3.1. The output of the trajectory simulation will provide the required input for the noise model, so that the noise impact caused by the selected initial weight can be determined. The required number of simulations is

again based on the CLT and is therefore determined with Eq. 4.10. Since the same confidence interval of 95 % is used and the allowable error from the mean is again 5 %, the required sample size for the Monte Carlo simulation is again approximately equal to 1500.

Just as with the lateral position error, the Monte Carlo simulation of the starting weight will result in a set of N SEL values for each grid point $g^{i,j}$. The expected SEL value and variance of SEL at each grid point is calculated with Eq. 4.11 and Eq. 4.12, the same method that was used as for the lateral position deviation simulation. Since at this point it is not known how the initial weight deviation will affect the different states and therefore the received SEL, no distribution for the SEL is assumed at this point. Instead, the deterministic expected number of awakenings is selected as an additional output from the Monte Carlo simulation. This results directly in a set of N Awak values, where the overall expected value is determined as follows:

$$\mathrm{E}\left[\mathrm{Awak}\right] = \sum_{k=1}^{N} \mathrm{Awak}_k \tag{4.27}$$

And the variance of the overall number of awakenings with:

$$\mathrm{Var}\left(\mathrm{Awak}\right) = \frac{1}{N} \sum_{k=1}^{N} \left(\mathrm{Awak}_k - \mathrm{E}\left[\mathrm{Awak}\right]\right)^2 \tag{4.28}$$

Again, no distribution is assumed at this point. Therefore, only the expected value and variance of the number of awakenings will be determined.

For the optimization implementation, the same problem is present as with the lateral position error. Running a Monte Carlo simulation for every trajectory that needs to be evaluated will result in a too high computational cost, so is therefore no option. Creating again a function to approximate the awakenings distribution is also not possible, because the actual probability distribution due to the weight deviation is not known. Therefore, an 'online' method is proposed, where before the optimization the initial weight distribution is discretized in Q segments. For each segment, a corresponding expected weight and probability can be determined, depending on the assumed distribution for the starting weight. An example is shown in Fig. 4.6, where the normal distribution for the initial weight is divided in 5 segments.

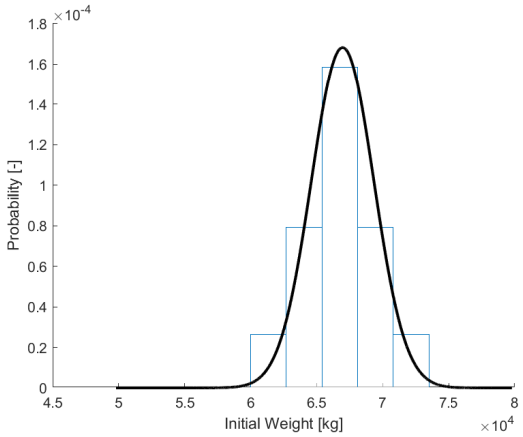

Figure 4.6: The initial weight distribution discretized with $Q = 5$

After the discretization, there is a set of initial weights $[W_0^1, W_0^2, ..., W_0^q]$ with a corresponding set of probabilities $[\mathrm{P}_W^1, \mathrm{P}_W^2, ..., \mathrm{P}_W^q]$. During the evaluation of a trajectory in the optimization, the trajectory gets simulated Q times with a different initial weight W_0, resulting in q sets of state variables. Those sets will be the input for the noise model, resulting in set of number of awakenings values $[\mathrm{Awak}_W^1, \mathrm{Awak}_W^2, ..., \mathrm{Awak}_W^q]$. Since the set of probabilities is unchanged, the expected value of the number of awakenings can be determined as follows:

$$\mathrm{E}\left[\mathrm{Awak}_W\right] = \sum_{q=1}^{Q} \mathrm{Awak}_W^q \mathrm{P}_W^q \tag{4.29}$$

The variance of the number of awakening can also be calculated in the following way:

$$\mathrm{Var}\left(\mathrm{Awak}_W\right) = \sum_{q=1}^{Q} \left(\mathrm{Awak}_W^q - \mathrm{E}\left[\mathrm{Awak}_W\right]\right)^2 \mathrm{P}_W^q \tag{4.30}$$

Similar as with the lateral deviation approach, the expected value of number of awakenings will be used as an objective function in the optimization. As second objective, the total amount of fuel will again be used. Also the constraints for this problem will not differ with respect to the deterministic one, so the multi-objective optimization can be stated as follows:

$$\begin{aligned} \min_{\bar{\mathbf{x}},\gamma_\mathbf{n},\eta_\mathbf{n}} : \quad & \left\{\mathrm{E}\left[\mathrm{Awak}_W\right], \mathrm{Fuel}\right\} \\ & \mu \leq \mu_{\max} \\ \text{s.t.} \quad & h_\mathrm{f} = h_{\mathrm{final}} \\ & V_{\mathrm{EAS,f}} = V_{\mathrm{EAS,\,final}} \end{aligned} \tag{4.31}$$

5

VERIFICATION AND VALIDATION

In this chapter, the models and tools used in this thesis will be verified and validated. First, the aircraft simulation model output will be compared with the results from Ho-Huu [24] for three departure routes. The optimization algorithm will be verified by performing the same case study as was executed by Ho-Huu [24], namely the Spijkerboor departure route of AAS. The assumptions made for the simulation of the lateral position error will be validated with ABS-B flight data. Finally, the approach to approximate the distribution of the number of awakenings due a lateral position variation will be verified by comparing them with the results from the Monte Carlo simulation.

5.1. TRAJECTORY SIMULATION

For the verification of the trajectory simulation model, the results of the model will be compared with the results from the model used by Ho-Huu [24]. Here, a similar model was used to simulate a departure trajectory, which could then be optimized with an evolutionary algorithm. Besides that the model from Ho-Huu has one vertical segment less, the input to model is similar to the one used in this thesis. Three test cases will be selected from the optimization results from the case study by Ho-Huu: the optimal departure with minimum number of awakenings (1), the optimal departure with minimum amount of fuel burnt (2) and an optimal departure which is in the middle of those two (3). In Fig. 5.1 the three optimal solutions are highlighted on the Pareto front.

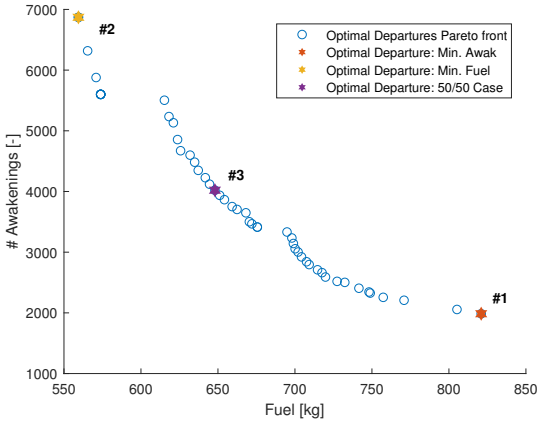

Figure 5.1: The Pareto front containing the optimal departure routes for the Spijkerboor case study from Ho-Huu [24].

The input data for the three cases is presented in Tab. 5.1. Since the model for this thesis uses one more segment, it requires an additional climb angle and thrust setting. For all three cases, they are assumed to be zero, due to the fact the maximum altitude and velocity is already reached at the start of the final segment.

	Case 1: Min Awak	Case 2: Min Fuel	Case 3: 50/50
L_1 [m]	6455.83	615.882	740.705
R_2 [m]	9894.89	4990.04	6057.69
$\Delta\chi_2$ [rad]	2.25547	2.70911	1.41017
L_3 [m]	39923.1	3292.58	10610.4
R_4 [m]	9674.44	9206.68	9784.86
h_1 [m]	262.78	247.8655	266.3251
$\gamma_{n,2}$ [-]	0.027188	0.127054	0.218584
$\gamma_{n,3}$ [-]	0.003215	0.166934	0.011245
$\gamma_{n,4}$ [-]	0.134559	0.633833	0.293531
$\gamma_{n,5}$ [-]	0.306427	0.514784	0.724666
$\gamma_{n,6}$ [-]	0.372327	0.690991	0.344921
$\gamma_{n,7}$ [-]	0.520826	0.487045	0.506183
$\gamma_{n,8}$ [-]	0.751058	0.558842	0.595639
$\gamma_{n,9}$ [-]	0.694733	0.20134	0.401242
$\gamma_{n,10}$ [-]	0.395692	0.159596	0.744709
$\gamma_{n,11}$ [-]	0	0	0
η_3 [-]	0.180738	0.989569	0.594573
η_4 [-]	0.936912	0.691292	0.859164
η_5 [-]	0.891184	0.880454	0.732374
η_6 [-]	0.540103	0.832011	0.708034
η_7 [-]	0.484581	0.144468	0.070289
η_8 [-]	0.997541	0.784709	0.350983
η_9 [-]	0.535053	0.569216	0.08056
η_{10} [-]	0.391706	0.725643	0.701088
η_{11} [-]	0	0	0

Table 5.1: The input design variables for the three cases used in the verification of the trajectory simulation model.

First, the ground track for the three departures is generated with both simulation models and is plotted in Fig 5.2. As can be seen, both tracks for the three case align almost perfectly, with an error always smaller than $\epsilon \pm 10^{-5}$ m. Therefore, it can be concluded that the ground tracks generated with both simulates are similar. Results regarding the vertical profile can be found in Tab. 5.2, where the final altitude and velocity for both simulation models are stated. As can be seen, the difference is not significant and therefore neglected.

	Case 1: Min Awak		Case 2: Min Fuel		Case 3: 50/50	
	Smits	Ho-Huu	Smits	Ho-Huu	Smits	Ho-Huu
h_{final} [m]	1849.134	1845.253	1849.108	1845.486	1842.011	1841.939
V_{final} [m/s]	140.991	140.941	140.973	140.9474	141.986	141.3009

Table 5.2: Simulation results for the three test cases compared with the results from Ho-Huu [26].

Results regarding the environmental impact can be found in Tab. 5.3. With respect to awakenings, there is a difference between the two simulation models present of ±1% of the total number of awakenings. For the total amount of fuel burnt, this difference is ±0.2% of the total amount. These errors could be explained due the fact that for the vertical segments are differently chosen for the simulations. Therefore, it is assumed that the differences for the two simulation methods with respect to the objective criteria are negligible.

5.2. OPTIMIZATION ALGORITHM

To check if the multi-objective optimization algorithm works properly, the same optimization case study from Ho-Huu [26] will be performed. Here, the Spijkerboor SID is optimized for the total number of awakenings and the total amount of fuel burnt. For this departure, the constrains are based on the ICAO procedures. The bounds for the ground track and the vertical profile paramters can be found in Tab. 5.4. For a more detailed

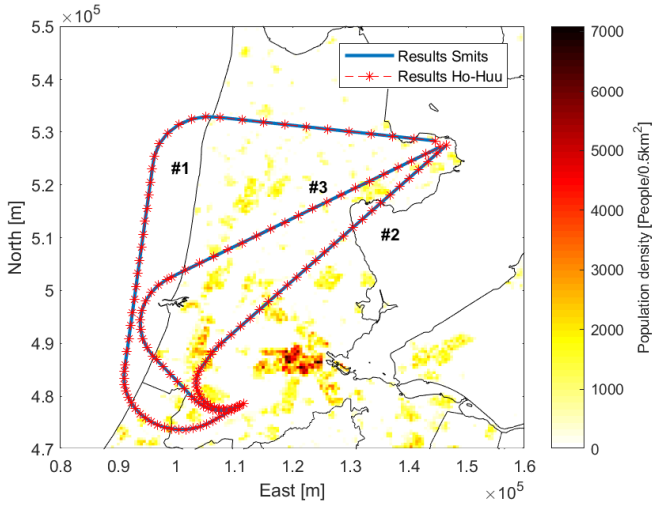

Figure 5.2: The ground track for the Spijkerboor departure route

	Case 1: Min Awak		Case 2: Min Fuel		Case 3: 50/50	
	Smits	Ho-Huu	Smits	Ho-Huu	Smits	Ho-Huu
Awakenings [-]	1995	1986	6924	6870	4021	4044
Fuel [kg]	819.71	820.95	558.63	559.41	648.03	647.15

Table 5.3: Simulation results for the three test cases compared with the results from Ho-Huu [26].

description, see Sec. 6.2.1. where a comparable case study is performed.

	Lower bound	Upper bound
L_1 [m]	614	10000
R_2 [m]	2000	10000
$\Delta\chi_2$ [deg]	32	170
L_3 [m]	1000	40000
R_4 [m]	2000	10000
h_1 [ft]	800	1500
$\gamma_{n,1}$ [-]	1	1
$\gamma_{n,2-N}$ [-]	0	1
η_1 [-]	1	1
η_2 [-]	1	1
η_{3-N} [-]	0	1

Table 5.4: Bounds for the ground track parameters used in the Spijkerboor case study.

Due to the ICOA procedures, the aircraft is required to have a maximum climb angle and thrust setting until it reaches the altitude of h_1. Therefore, the normalized settings are set to 1 for the first segment. The second segment ends until the aircraft reaches an altitude of 3000 ft or an clean velocity of 190 kts, where it is required to still fly at maximum thrust settings. From there, the remaining $N-2$ segments are divided in equally distances flown and both the climb angle and the thrust settings are free to vary. The optimization problem self cna be stated as follows:

$$\begin{aligned} \min_{\mathbf{x},h_1,\gamma_\mathbf{n},\eta_\mathbf{n}}: \quad & \{\text{Awak, Fuel}\} \\ & \mu \leq \mu_{\max} \\ \text{s.t.} \quad & h_\text{f} = 6000\text{ft} \\ & V_{\text{EAS,f}} = 250\text{kts} \end{aligned} \tag{5.1}$$

The results of the optimization are presented with a Pareto-front in Fig. 5.3. As can be seen, the fronts are located close to each other and both consists of the same three curves. These three curves correspond to the three groups of trajectories, which are plotted in Fig. 5.4. Again, the solutions from both optimizations are almost similar, with no noticeable differences present. Therefore, it is safe to assume the proposed optimization algorithm works properly.

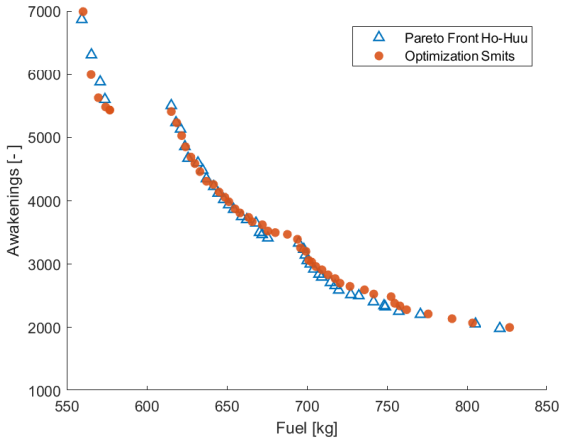

Figure 5.3: Optimization results compared with the results from Ho-Huu [26].

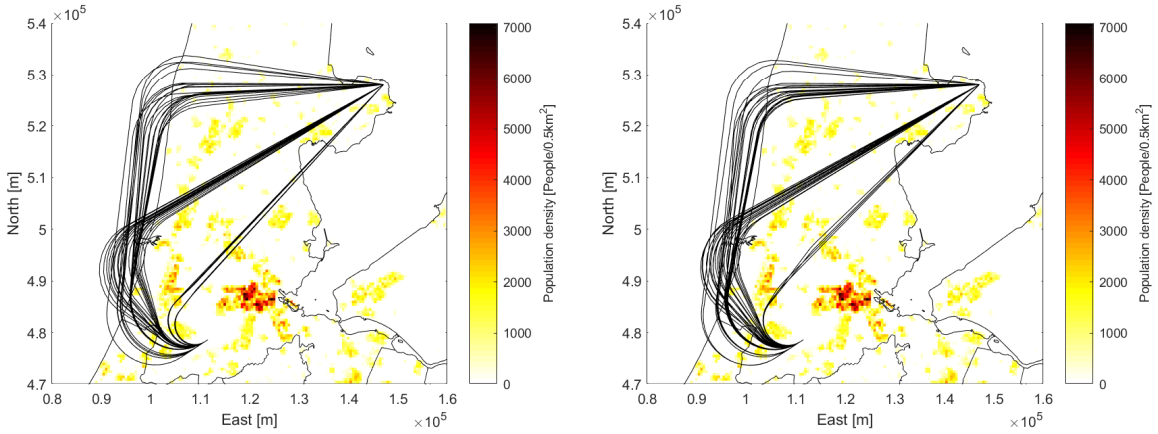

(a) Smits (b) Ho-Huu

Figure 5.4: Ground track results from Spijkerboor case study performed by this thesis and Ho-Huu.[26].

5.3. LATERAL POSITION ERROR SIMULATION

When developing the model for the simulation of the lateral position error, a couple of assumptions were made. To check if these assumptions were valid, the simulation model will be compared with actual Automatic Dependent Surveillance- Broadcast (ADS-B) data obtained at the Delft University of Technology [25]. Over 200 departure flights for the Spijkerboor route were recorded on the same day and plotted in Fig. 5.5. In the same plot, the bounds of the RNP 1 are also shown. As can be seen, most of the flights satisfy the navigational requirements. Especially in the beginning of the departure, the tracks remain in between the bounds. However, after the first turn, more lateral deviation occurs. Also, it seems that when the aircraft is deviated, no correction is made and it continues to fly to way point ANDIK.

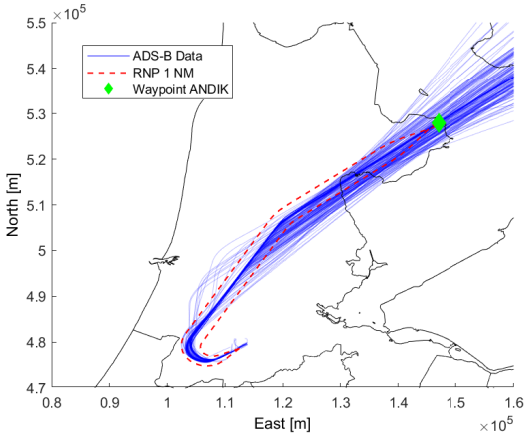

Figure 5.5: ADS-B data for departures from Runway 24 at AAS

For this thesis, the assumptions regarding the lateral position error are accepted. Although the ADS-B data shows the a RNP of 1 NM is an over estimation at the beginning of the departure, for the remaining part it seems as a sufficient representation of the data.

5.4. SEL DISTRIBUTION APPROXIMATION FUNCTION

Since a Monte Carlo simulation for every track evaluation would increase the computational cost significantly for the optimization, an approximation function was developed to obtain similar results as the simulation would generate. As a verification of that approximation function, its results are compared with that of the Monte Carlo simulation for four trajectories. The first one is the standard Spijkerboor departure, which follows the ICAO procedures. The other test cases will be three solutions from the Pareto front from the Spijkerboor departure optimization. The first one will be the solution for the minimum number of awakenings (Min Awak), the second for the minimum amount of fuel burnt (Min Fuel) and the third one will a solution between those two extremes (50/50), see Fig. 5.6.

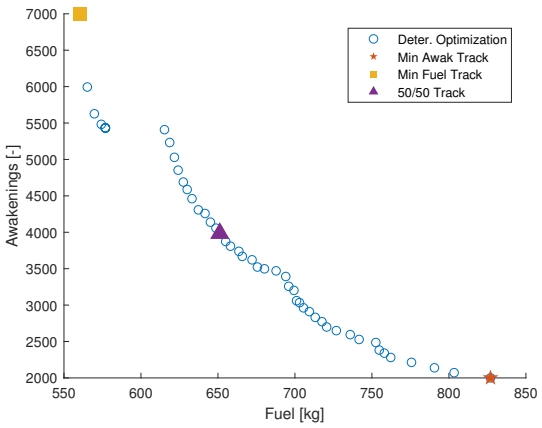

Figure 5.6: The results from the deterministic optimization, with the three test cases highlighted.

For those tracks, the lateral position error will be simulated with the use of a Monte Carlo simulation. For the distribution of the lateral deviation, the normal distribution based on the RNP 1 will be used, $N(\mu_{\text{RNP}}, \sigma^2_{\text{RNP}})$. The sample size will be based on the Central Limit Theory and will be equal to $N = 1500$. The data used in the approximation function will be based on the same lateral error distribution. For both calculations, the same grid of 80x80 km will be used, with a grid size of 500 m. The output for both approaches will be the standard

deviation $\sigma_{\text{SEL}}^{i,j}$ of the SEL at each grid point. The relative and absolute difference between the simulation and the approximation can be found in Fig. 5.7, 5.8, 5.9 and 5.10 .

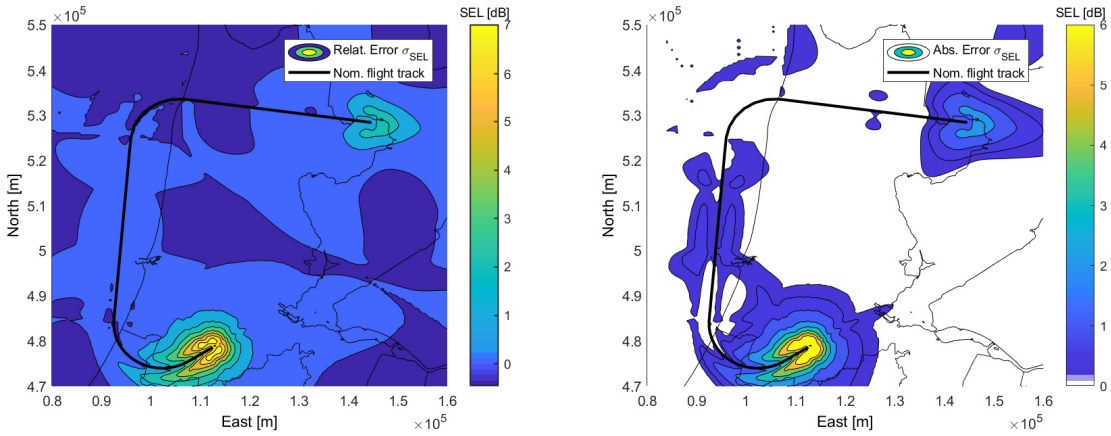

(a) Relative difference in σ_{SEL} (Approx. - Monte Carlo) (b) Absolute difference in σ_{SEL}

Figure 5.7: Comparison of the σ_{SEL} results between the Monte Carlo simulation and the approximation function for the Min Awak track.

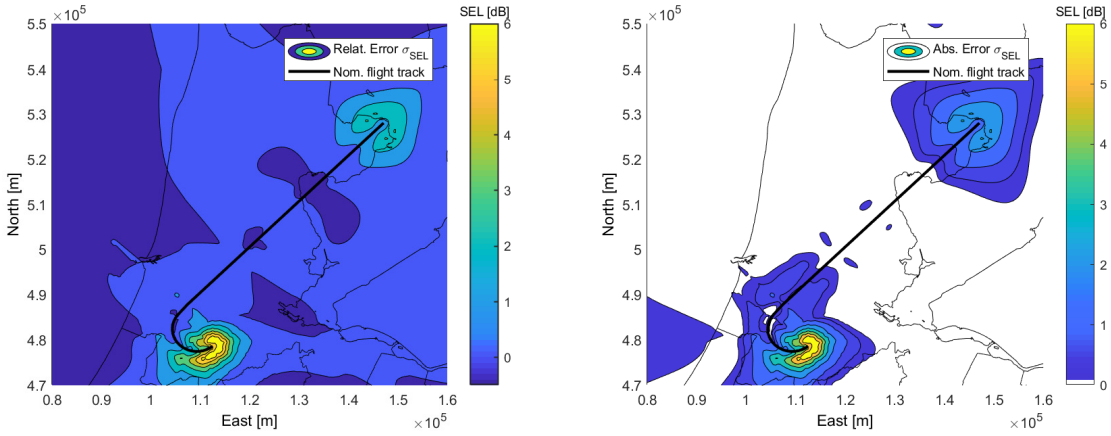

(a) Relative difference in σ_{SEL} (Approx. - Monte Carlo) (b) Absolute difference in σ_{SEL}

Figure 5.8: Comparison of the σ_{SEL} results between the Monte Carlo simulation and the approximation function for the Min Fuel track.

As can be seen in all three test cases, the biggest error occurs at the beginning of the departure. This is mainly due to that at the start of trajectory no lateral position error is simulated. Also, the lookup table from the estimation function starts at an altitude of 1000 ft, so the $\sigma_{\text{SEL}}^{i,j}$ is probably over estimated for grid points surrounding the beginning of the trajectory. For the third test case however, significant errors also occur right of the third leg. This could be explained by the fact that grid points right of L_3 are also effected by two turns $R_2\Delta\chi_2$ and $R_4\Delta\chi_4$.

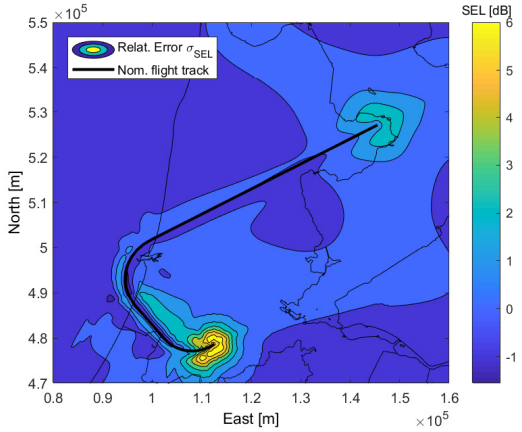

(a) Relative difference in σ_{SEL} (Approx.- Monte Carlo)

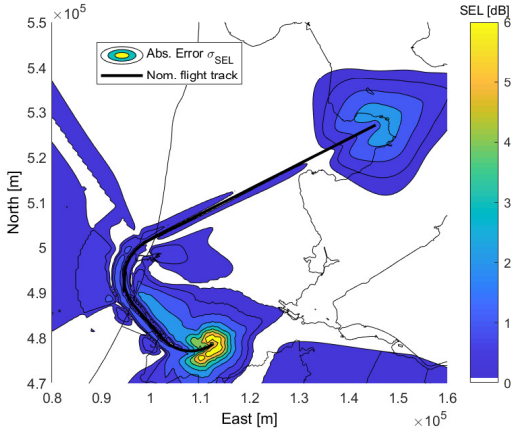

(b) Absolute difference in σ_{SEL}

Figure 5.9: Comparison of the σ_{SEL} results between the Monte Carlo simulation and the approximation function for the 50/50 track.

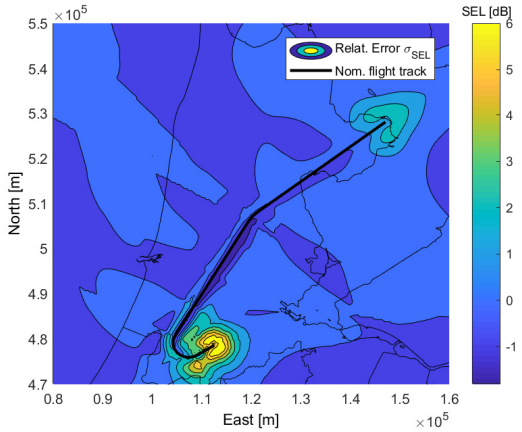

(a) Relative difference in σ_{SEL} (Approx.- Monte Carlo)

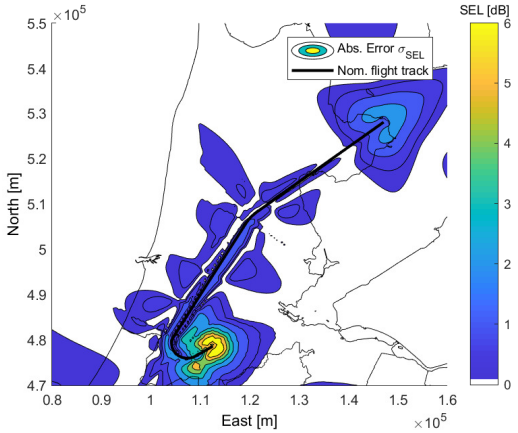

(b) Absolute difference in σ_{SEL}

Figure 5.10: Comparison of the σ_{SEL} results between the Monte Carlo simulation and the approximation function for the SID.

5.5. NORMALITY TEST OF SEL DISTRIBUTION

To check if the set of $SEL^{i,j}$ data is normally distributed, the Kolmogorov-Smirnov Test for Normality (KS-test) will be performed. A Monte Carlo simulation of a segment will be set up, and the cross section SEL data will be generated. For this test, a straight level flight at an altitude of 5000 ft. is simulated with a lateral position error $N(0,\sigma^2_{RNP})$. The setting of the remaining parameters can be found in Tab. 5.5.
The cross section grid will be 55 km long, ranging from -5 km from the nominal flight segment to a distance of 50 km. The grid size will be 250 m, so in total there will be 220 data points. The sample size N is derived with the use of the Central Limit Theory and is equal to $N = 1500$. The results for the average and the standard deviation of the SEL are plotted in Fig. 5.11.

As expected, the average SEL has highest value directly beneath the flight track and declines when the distance increases. However,for the standard deviation the peak occurs at a distance of $d \approx 2.5$ km from the nominal track. From that peak, the standard deviation decreases when getting closer the nominal track until it reaches a local minimal value directly beneath the trajectory. When performing the KS-test for this area, it was clear that there the SEL values are not normally distributed. This can also be clearly seen when the SEL values at 5 different distances are plotted, see Fig. 5.12.
For distances further away ($d > 2.5$) the SEL looks like it is normally distributed, while the average value and spreading decreases when the distance increases. This concurs with results presented in Fig. 5.11. The distributions at grid points closer than 2.5 km are clearly not normally distributed. Also, it seams that the

Parameters	Initial value
h	5000 ft.
V_{EAS}	130 m/s
η	0
γ_n	0
W	63000 kg
R	0 m

Table 5.5: The parameters values for the straight level flight segment.

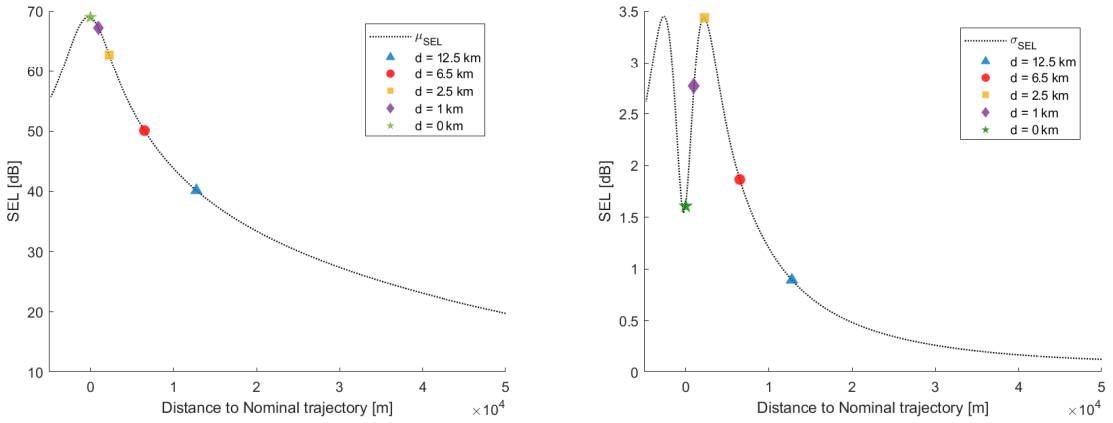

(a) The average SEL at a distance from the nominal flight segment.

(b) The standard deviation of SEL at a distance from the nominal flight segment.

Figure 5.11: Results for the lateral position error simulation of a straight flight segment at an altitude of 5500 ft.

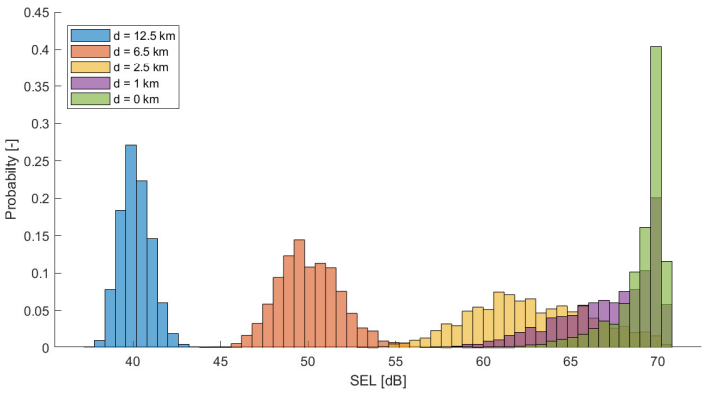

Figure 5.12: Distributions of SEL as a result of the Monte Carlo simulation at 5 different distances d.

distributions not exceed a SEL of 71 dB. Although at first this may seems strange, this observation can easily be explained. When a receiver is close the nominal track, the lateral deviation can cause the aircraft to be further away from the receiver instead of closer. Therefore, a maximum SEL value that could occur is already observed and cannot be exceeded by deviating the lateral position. So what happens is that instead getting a higher value than the maximum SEL value, the same maximum SEL value is observed. This creating the peak at the right end of the distribution and therefore also the decrease in the variance of SEL. And when taking in mind that with the assumed distribution of the lateral position error, 99% of the cases the deviation is between $3\sigma_{RNP}$, the location of the standard deviation peak can be explained. The distance value $d \approx 2.5$ is close to the distance corresponding of $3\sigma_{RNP} \approx 2.8$ km. Therefor, it is concluded that SEL values observed at $d < 2.8$ km are not normally distributed, but have a custom distribution.

Although completely estimating this custom distribution is rather difficult, the principle can be taken into account in the approximation function. Due to the fact the SEL distributions are discretized, they can easily be modified. For a discretized SEL distribution located close to the nominal trajectory, if $SEL_k^{i,j} > SEL_{\max}^{i,j}$, then set $SEL_k^{i,j}$ equal to that maximum SEL. The maximum SEL value that could occur on a cross section for certain set of parameter settings can be determined with the nominal flight track cross section results. For the discretized distribution, the average SEL value will remain the same, but the maximum σ_{SEL} on that cross section will be used as the standard deviation. This corrected approximation approach is applied on the distribution at $d = 1$ km and the results are plotted in Fig. 5.13.

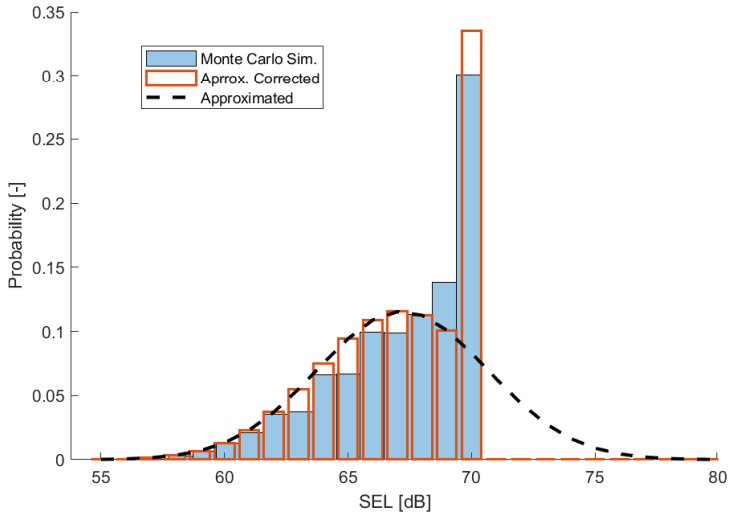

Figure 5.13: Distributions of SEL at $d = 1$ km, as a result of the Monte Carlo simulation, the approximation function and the corrected approximation function.

As can be seen, the normal approximated distribution does exceed the maximum SEL value that could occur for that cross section. The corrected approximation function however is more similar to the data obtained with the Monte Carlo simulation. Therefore, the corrected approximation function will be implemented in the optimization framework.

5.6. NUMBER OF AWAKENINGS DISTRIBUTION

Finally, in Sec. the distribution of the number of awakenings is estimated based on the distribution of the SEL over a certain grid. For this, the assumption had to be made that SEL data at grid points close together are depended on each other, and at points further away they are independent. Also, the distributions of the noise were discretized to apply the ANSI criterion function. To verify this approach and check if the assumptions hold up, the approximated distribution of awakenings is compared to the estimated distribution obtained with a Monte Carlo simulation.

In Fig. 5.14 the results from the Monte Carlo simulations for the three test cases are presented, together with the approximated distribution of Awakenings. For the approximation distribution, it is assumed that grid points are independent of each other when they are located further away that 1 NM. When the grid points are closer to each other, the Awakenings values are assumed to dependent to each other. For the Monte Carlo simulation, a sample size of $N = 1500$ is used. For the lateral deviation error, the normal distribution $N(0, \sigma_{\text{RNP}}^2)$ is applied, see 4.1.

As can be seen, the shape of the simulated distributions is not quite symmetrical for the Min Awak and the 50/50 track. However, the simulated distribution for the Min Fuel track is symmetrical, and therefore fits the approximated normal distribution almost perfectly. An explanation for the asymmetrical shapes could be that the population left and right of the track are not equally divided. When these trajectories would deviate more to the left, they would fly more over the sea where no population is present. Therefore, there is a peak for lower number of awakenings, because deviating further in that direction will not result is less awakenings.

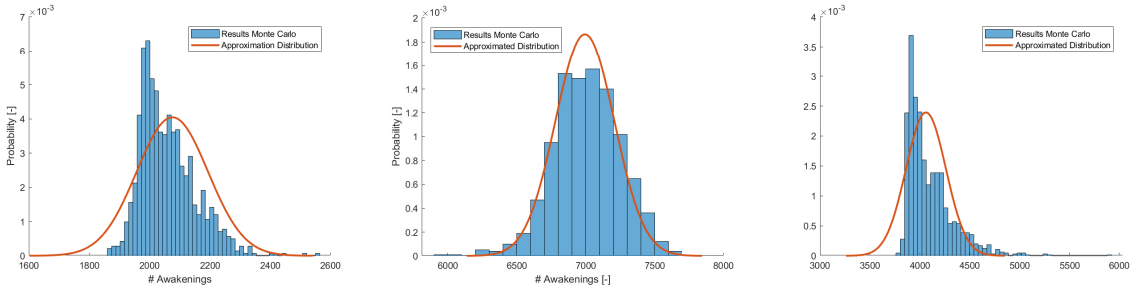

(a) Minimum Awakenings track (b) Minimum Fuel track (c) 50/50 Awaks/Fuel track

Figure 5.14: The approximated distribution of awakenings compared with the results from the Monte Carlo simulation.

The trajectory with minimum fuel burnt is set directly over the populated area, so there would deviation left or right result in less awakenings. Although the shape may not always match the approximated distribution, the variance seems to do for all three cases. For the Min Awak and 50/50 track, the variance is a little over estimated, because the approximation does not take into account the peak that occurs for those two cases.

6

CASE STUDY

Now that the models and optimization algorithm are verified, their capabilities will be illustrated by performing several case studies. The case studies are all related to Amsterdam Airport Schiphol, due to the fact it is an airport located close to inhabited areas and its growth is restricted partly due noise regulations. Two departures will be described, which will be used for both the stochastic analysis and the multi-objective optimization. The results obtained from the stochastic analysis of the lateral position error will be presented and discussed, followed by the results from the initial weight analysis. Next, the two departures will be optimized with respect to the noise and emission impact. This chapter will conclude with an adjusted case study, where a different cutoff value for the ANSI criterion is used, which effects the noise impact calculations.

6.1. PROBLEM DESCRIPTION

To test the full potential of the stochastic model and the optimization algorithm, a case study is required which has an relative busy airport located close to inhabited areas. Amsterdam Airport Schiphol, which was also used in some previous noise abatement studies [28],[10],[26], is selected for this research because it is located close to several communities and is one of the busiest airports in Europe []. Next to that, AAS is an airport which is restricted to grow due to noise regulations. Because AAS attempted to increase their capacity, their was a significant increase in noise complaints in the year 2017 [29]. Therefore, minimizing the noise impact for AAS would have a positive effect for both the airport itself as well for the communities nearby.

The case study scenarios will be based on two SIDs from Amsterdam Airport Schiphol: the Spijkerboor departure from runway 24 and the the ARNEM departure from runway 09. The first one is selected due the fact the trajectory passes over a couple of inhabited areas and was used in previous noise abatement studies. The second departure also encounters some inhabited areas, but was actually selected to illustrate that the optimization framework and the stochastic model could be applied on all different kind of trajectories. Next to that, both SIDs are two of the most flown departures at AAS in 2017, as can be seen in Fig. 6.1, and have therefore a significant amount effect on the overall noise impact. Both departure trajectories will be described, as well as their bounds and constrains regarding the optimization framework.

6.1.1. SPIJKERBOOR 2K FROM RUNWAY 24

The standard instrumental departure Spijkerboor takes off from runway 24 at AAS. It passes by the cities of Haarlem and Hoofddorp, where most of the noise annoyance occurs. For the optimization, the screen height of 50 ft is where the trajectory starts, with a take-off safety speed of $V_2 + 10$ kts. At this point, the landing gear is retracted and the departure flaps are selected. The exit conditions, at waypoint ANDIK, are an airspeed $V_{\text{EAS}} = 250$ kts at an altitude $h_f = 6000$ ft. Between these starting and exit point, the ground track consists of three straight (TF) legs and two constant radius (RF) legs. See App. A for the standard instrument departure chart.

With respect to the vertical profile, this is subdivided in 11 segments, while it complies with the NADP-1 procedures. For the first vertical segment, it is prescribed that full take-off thrust should be applied, while maintaining the take-off safety speed. The segments ends when the cutback altitude h_1 is reached. For the

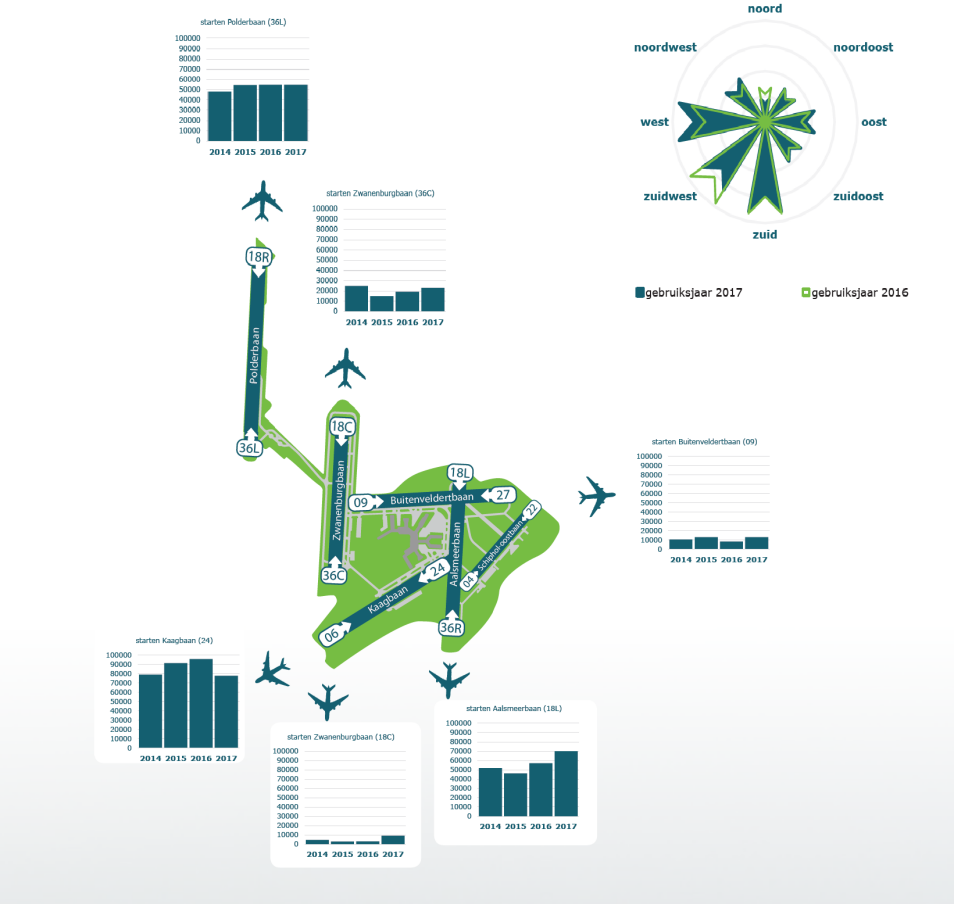

Figure 6.1: The number of departures per runway for Amsterdam Airport Schiphol in the year 2017 [29]

second segment the aircarft can fly at a reduced flight path angle, but still at a maximum thrust setting. The end of the second segment is either when the altitude $h_2 = 3000$ ft or the airspeed $V_{clean} = 220$ kts is reached. From that point, both the trust setting and the climb angle setting are an optimal design variable, but the aircraft is not allowed to decelerate or descend. The remaining segments are divided in equal distance segments. The ground track parameters for the current SID, as well the bounds used in this optimization, are stated in Tab. 6.1. The vertical parameters bounds can be found in in Tab. 6.2.

	Current SID	Lower bound	Upper bound
L_1 [m]	4100	614	10000
R_2 [m]	3183	2000	10000
$\Delta\chi_2$ [deg]	152.4	32	170
L_3 [m]	29150	1000	40000
R_4 [m]	7500	2000	10000

Table 6.1: Bounds for the ground track parameters used in the Spijkerboor case study.

In total there are 25 optimal design variables used as an input for the trajectory evaluation. The grid used here is a 80×80 km with a grid size of 500 m, which corresponds to 25600 grid points. This number is reduces 7269 points, by filtering out points where the population density is less than 500 people per 0.5km^2. See Fig.6.13 for the bounds of the grid.

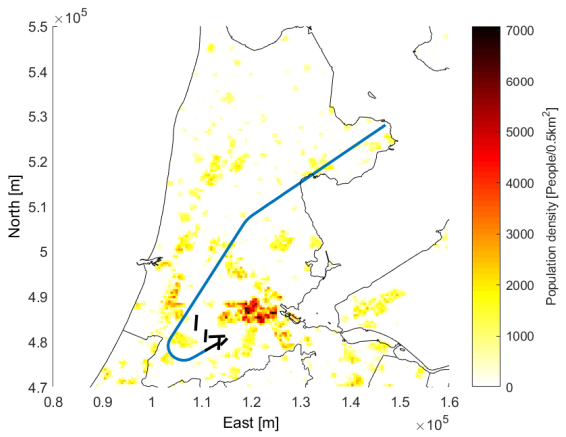

Figure 6.2: The Spijkerboor SID with population density.

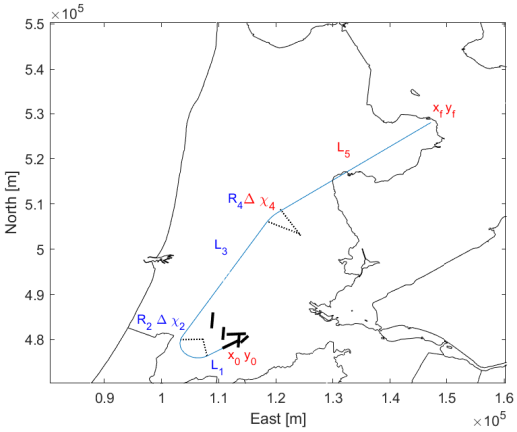

Figure 6.3: The ground track parameterization for the Spijkerboor departure route

	Lower bound	Upper bound
h_1 [ft]	800	1500
$\gamma_{n,1}$ [-]	1	1
$\gamma_{n,2-11}$ [-]	0	1
η_1 [-]	1	1
η_2 [-]	1	1
η_{3-11} [-]	0	1

Table 6.2: Bounds for the vertical parameters used in the Spijkerboor case study.

6.1.2. ARNEM 3E FROM RUNWAY 18L

The ARNEM departure starts at runway 18L of Schiphol Airport and ends at the IVLUT waypoint. For this trajectory, the communities surrounding Hilversum recieved the most of the noise impact. The trajectory itself starts at the same screen height as the Spijkerboor departure and exists also at h_f = 6000 ft. The standard ground track consists of two straight (TF) legs and one constant radius (RF) leg. For the optimization however, the trajectory is allowed to have a second constant turn and therefore a third TF leg. For the parameters of the gound track, see Tab. With respect to the vertical profile, the same procedure is applied as for the Spijkerboor departure, so the same vertical parameters are used in the optimization (Tab. 6.3). For the standard instrument departure chart of ARNEM 3E route, see App. A .

	Current SID	Lower bound	Upper bound
L_1 [m]	1000	614	10000
R_2 [m]	4000	2000	8000
$\Delta\chi_2$ [deg]	90	60	130
L_3 [m]	28500	1000	12000
R_4 [m]	0	2000	10000

Table 6.3: Bounds for the ground track parameters used in the Spijkerboor case study.

Therefore, the same number of 25 optimal design parameters will be used as an input for the trajectory optimization. A grid of 60 × 60 km with a grid size of 500 m will be used for the noise calculations. However, by filtering out data points based on GIS, the number of data points is reduces to 5661. See Fig.6.4 for the current ARNEM 3E SID and the bounds of the grid.

6.2. STOCHASTIC ANALYSIS: LATERAL POSITION

With the use of the stochastic model presented in Ch. 4, a stochastic analysis is performed for both the Spijkerboor 2K and ARNEM 3E case study. The lateral position deviation will be simulated with the use of a Monte Carlo simulation and the results for SEL and number of awakenings will be discussed. These results

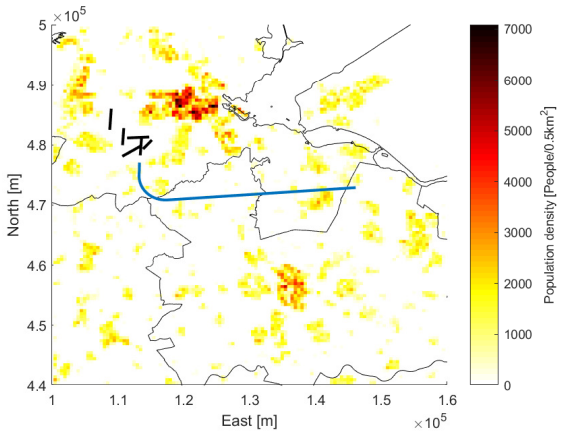

Figure 6.4: The ARNEM 3E SID with population density.

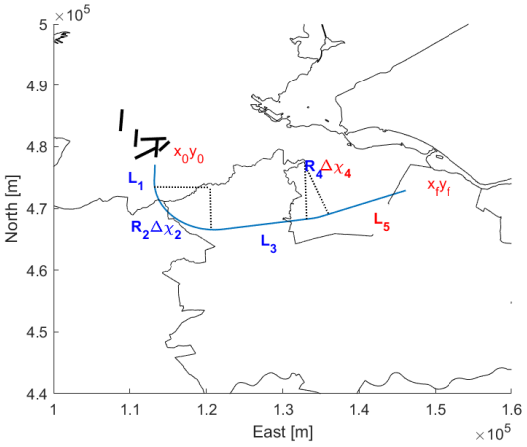

Figure 6.5: The ground track parameterization for a ARNEM departure route

will also be compared to the ones generated with the deterministic aircraft model (Ch. 3), to get a better understanding of the effect when taking into account a lateral position error. A similar analysis will be performed for the ARNEM 3E case study, to investigate if the findings concur and therefore could be accepted.

6.2.1. SPIJKERBOOR 2K

The lateral position error is simulated over the standard instrument departure of the Spijkerboor 2K route, described in Sec.6.2.1. The lateral position error distribution is a normal distribution $N(0, \sigma^2_{\text{RNP}})$, where σ_{RNP} is equal to 926 m. For this simulation, a smoothing factor α of 0.3 is chosen, which results in a corrected standard deviation σ_ϕ of 1326 m, according to Eq. 4.6. For the required number of simulations, the Central Limit Theory is used, which resulted in $N = 1500$. To reduce computation time, the adjusted grid for just population areas is used. Finally, six locations along the trajectory are selected as waypoints according to the approach presented in Sec. 4.1, which are illustrated in Fig. 6.6. In the figure, the nominal track and a set of deviated tracks are plotted.

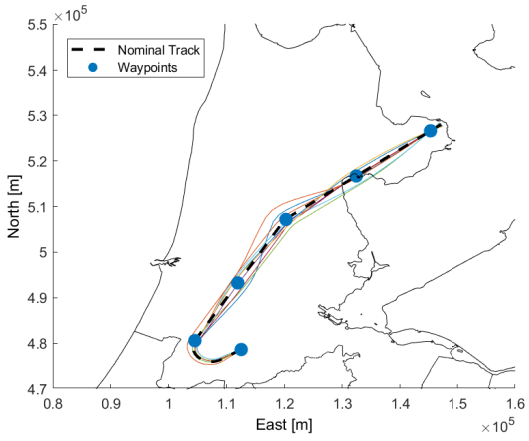

Figure 6.6: A set of results from Monte Carlo simulation of the Spijkerboor 2K case with the selected waypoints and nominal trajectory.

For the 1500 deviated trajectories, the noise impact is calculated with the INMTM v3 tool [5]. In this case, where 53 trajectory data points and 7296 grid points were used, the computation time was 1.486 h. The SEL data computed for each trajectory is stored in 1500×7269 matrix. For each grid point, the mean $\mu^{i,j}_{\text{SEL}}$ is determined. Due to the assumption that the SEL per grid point is normally distributed, or has an adjusted normal distribution, the expected SEL is assumed equal to the mean. The results for the $\text{E[SEL]}^{i,j}$ are presented in Fig. 6.7.

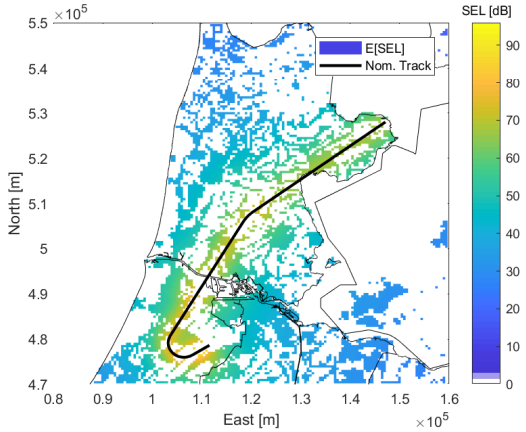

Figure 6.7: The expected SEL for the Spijkerboor SID, resulted from the lateral error simulation

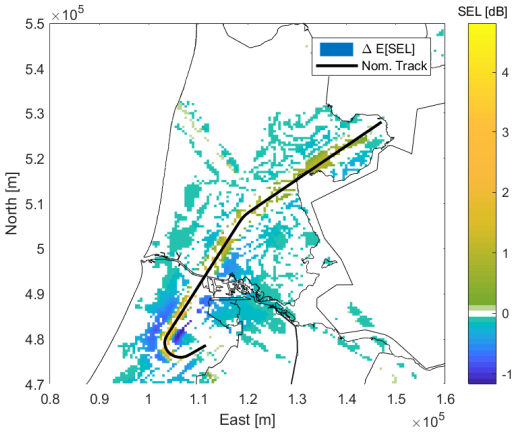

Figure 6.8: The difference in SEL between the lateral error and nominal track simulation for the Spijkerboor SID

As expected, the SEL values are relatively high close to the trajectory and decrease when grid points are located further away. Also, due to the fact that the altitude of the aircraft at the start of the trajectory is lower, the SEL values are there higher than at the end of the trajectory. When comparing the results of the Monte Carlo simulation with the ones from the deterministic simulation, SEL values close to the trajectory are lower when a lateral deviation is present. This is clearly visible in Fig. 6.8, where it seams that the area of overestimation matches with the 1 RNP bounds. This is of course understandable, since in that area the aircraft deviates symmetrically in lateral position, the average received SEL is always lower that for the nominal track. For the areas just outside of that border, the SEL simulated with the deterministic model is underestimated. This is again what was expected. In this area, there is now a probability that the aircraft trajectory is closer than normal, resulting in slightly larger average SEL values. Basically, the received noise gets spread out, resulting in over- and underestimated areas close to the trajectory with respect to expected SEL.

Next to the mean, the standard deviation of the SEL at each grid point ($\sigma^{i,j}_{\text{SEL}}$) is calculated. Because it is assumed that the SEL is normally distributed over the entire grid, except for grid points located close the nominal trajectory as was stated in Sec. 5.5, the standard deviation is equal to the square root of the variance. The results are plotted in Fig. 6.9.

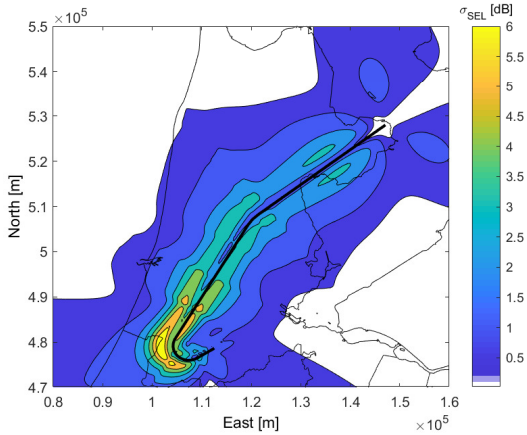

Figure 6.9: The standard deviation of SEL for Spijkerboor, resulted from the lateral error simulation

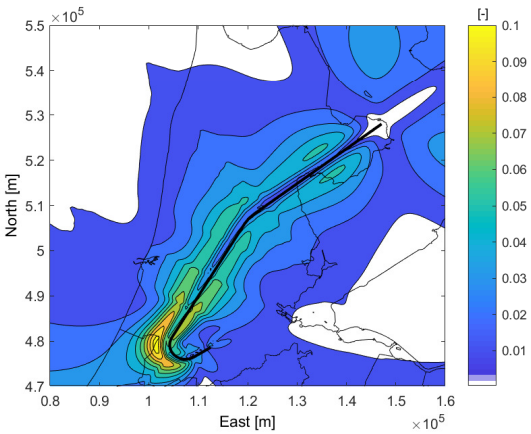

Figure 6.10: The normalized standard deviation divided for Spijkerboor, resulted from the Monte Carlo simulation

The first conclusion which can be made is that in overall, the standard deviation is higher closer to the trajectory. This is due to the fact that, as already stated before, the lateral deviation has more effect on areas closer to the trajectory. It could be argued that the standard deviation is higher, because the SEL values them self have higher values closer to the trajectory. However, when the deviation would be normalized by dividing it

by the mean of the SEL, the finding still holds up as can be seen in Fig. 6.10 . The second thing that is noticeable , is that the contours of the $\sigma^{i,j}_{\text{SEL}}$ are waving in and out. When observing the final straight part of the trajectory, the values of the standard deviation are not constant, while the distance to the trajectory remains the same. The bubbles in the contour seems to occur around the selected waypoints. Since the lateral position error is only determined at these waypoints and interpolated for the remaining data points, the deviation slightly decreases at the data points far away from a selected waypoint. Therefore, the standard deviation of the noise also decreases around those areas. Finally, it can be observed that the standard deviation of the SEL is higher at areas located outside of the turn than for the areas inside. An explanation for this could be that in this simulation the lateral position error in a turn segment almost remains constant. Therefore deviations to the outer side of the turn will result in larger distances flown, while deviations to the inner side will results in shorter trajectories. A lateral deviation has more impact on the longer turn segments than a shorter segment, so the aircraft deviates relatively more on the outer side of the turn. This of course will results in a larger deviation in received noise.

Due to the fact that the distribution of the SEL at each grid point can be represented as normal distribution $N(\mu_{\text{SEL}}, \sigma^2_{\text{SEL}})$, the expected number of awakenings can be determined with the approach discussed in Sec. 4.2. The results regarding the number of awakenings is plotted in Fig. 6.11.

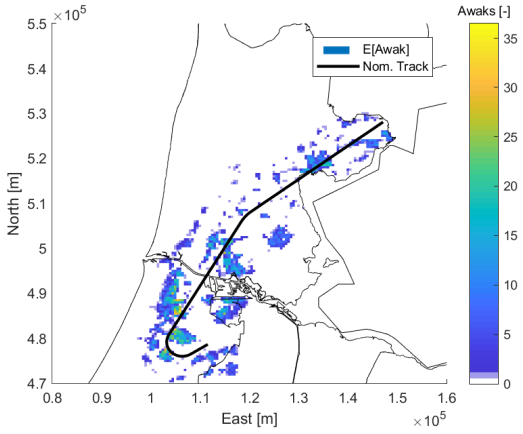

Figure 6.11: he expected Awak for the Spijkerboor SID, resulted from the lateral error simulation

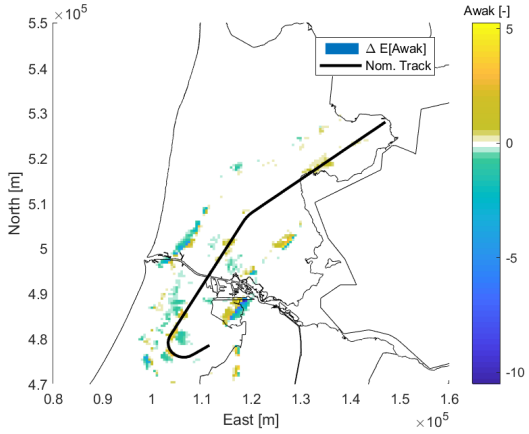

Figure 6.12: The difference in Awak between the lateral error and nominal track simulation for the Spijkerboor SID

Since the number of awakenings does not only depend on the distribution of SEL, but also on the population density, there is no clear correlation between the distance from the trajectory and the number of awakenings. Also, when looking at the difference between the expected number of awakenings and the results from the deterministic simulation in Fig. 6.12, the results appear to be minimal. When comparing the expected total number of awakenings (8297) with the the awakenings caused by the nominal trajectory (8246), the difference of 51 awakenings seems to be negligible. However, when the absolute difference in awakenings per grid point is summed, the total difference will be 1823 awakenings. Apparently, when comparing just the total number of awakenings, the over- and underestimated areas almost cancel each other out. Therefore, the results for both simulations look almost similar, but in fact there is a significant difference present. This phenomenon has to be kept in mind when comparing the optimization results for both the stochastic and deterministic simulation method, since there only the total number of awakenings is a criterion.

This absolute difference can be further explained when the area where an awakening could occur, is determined and analyzed. According to the ANSI function, which determines the percentage of awakenings, an awakening can only occur if the SEL is higher a certain cutoff value. For this analysis, a cutoff $\text{SEL}_{\text{Outdoor}}$ of 50.5 dB is used. The probability that a SEL value is higher than this cutoff value can be determined, since the distribution of $\text{SEL}^{i,j}$ is known. These probabilities per grid point are plotted in Fig. 6.13.

In the relatively big area around the trajectory, the probability that $P(\text{SEL}^{i,j} > 50.5\text{dB})$ is equal to 100 per cent. This is logical, because in that area the average SEL is much higher than the threshold level, there is no scenario where a SEL value will be lower than 50.5 dB. For a small region around this area, the probability

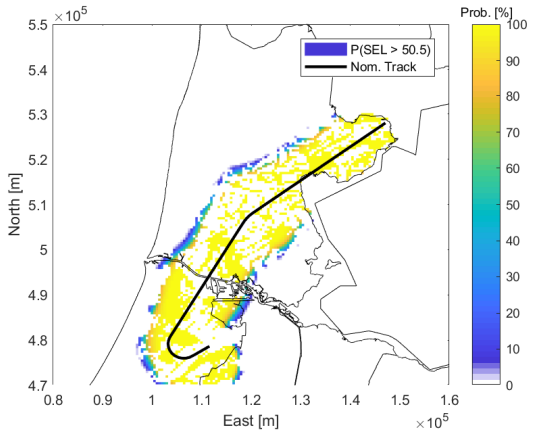

Figure 6.13: Probability that SEL is higher than 50.5 dB as a result of the lateral deviation for the Spijkerboor SID

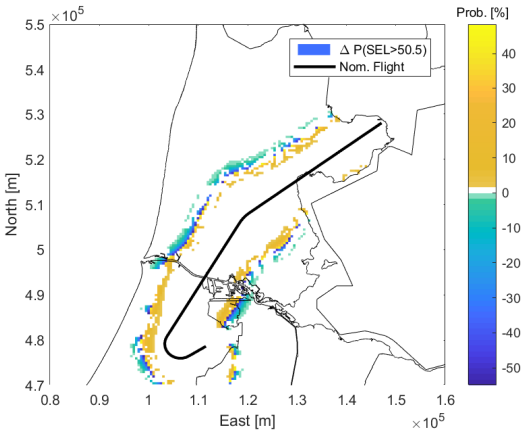

Figure 6.14: Difference in probability that SEL is higher than 50.5 dB for the Spijkerboor SID

declines when the distance to the trajectory increases. In the deterministic simulation, there is no variation in the noise levels, so the probability that a SEL value is above the threshold is either 100 % of 0 %. When the probability obtained with the Monte Carlo simulation is subtracted from that, an insight is generated where it is visible where the deterministic simulation over- or underestimates the probability. The results from that relative difference in probability is presented in Fig. 6.14. Here, positive values indicate when the deterministic approach overestimates the change that awakenings occur, and negative values for when an underestimation occurs. As can be seen, for a large area there is either a over- or underestimation present. However, due the fact that both occur, they cancel each other out and this difference is not noticeable when looking at the total number of awakenings.

6.2.2. ARNEM 3E

For the ARNEM 3E route a similar stochastic analysis is executed as for the Spijkerboor 2K SID. The same set of parameters is used regarding the lateral position errors, so $\sigma_{\text{RNP}} = 926$ m, $\sigma_{\phi} = 1326$ m, $\alpha = 0.3$ and $N = 1500$. The adjusted grid, discussed in Sec. 6.1.2, will be used for this Monte Carlo simulation. For this case study howeve, not the standard instrument departure will be used, but a solution from the optimal Pareto front. This decision is made because this additional case study is executed to substantiate the findings from the first case study. The selected trajectory has a wider first turn and a second turn, so the effect of a turn can be illustrated. Since this departure is still a lot shorter than the Spijkerboor SID, four grid points were selected along the trajectory. These waypoints, along with a couple of deviated trajectores, are shown in Fig. 6.15.

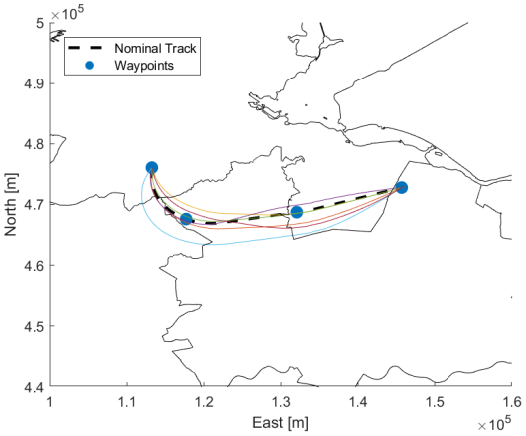

Figure 6.15: A set of results from Monte Carlo simulation of an optimal ARNEM 3E departure with the selected waypoints and nominal trajectory.

As for the first case study, the noise impact is determined with the INMTM v3 tool for the 1500 trajectories. Here, the trajectory consists of 46 data points and the grid of 5661 points. With the generated data, the $E[SEL]^{i,j}$ can be computed and compared to the results from the deterministic solution. The relative difference between the stochastic and deterministic simulation can be seen in Fig. 6.18. Just as in the first case study, the SEL seems to more spread out due to the lateral deviation. This resulting in that close to the trajectory the deterministic noise impact is higher than for the stochastic one, while a bit further away it is the other way around. When calculating the expected number of awakenings, it was clear that both the observed SEL as the population density both influences them. A correlation between the distance from the trajectory and the number of awakenings was again not present. For difference in $E[Awak]^{i,j}$ between both approaches, 3880 for the stochastic one and 3991 for the deterministic one, seems also to be insignificant. However, as also can be seen in Fig. 6.17, the absolute difference in awakenings per grid point is definitely present. In total, the absolute difference per grid is 453 awakenings, which is substantial.

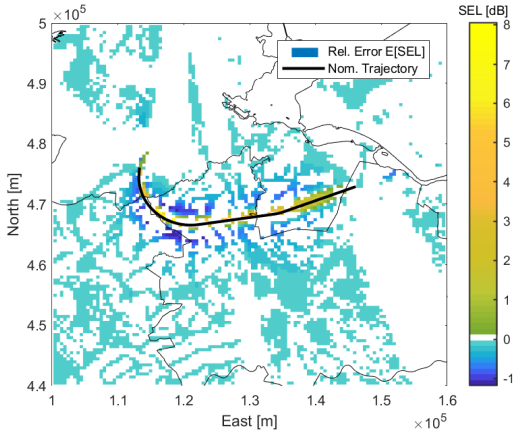

Figure 6.16: The expected SEL for the ARNEM SID, resulted from the lateral error simulation

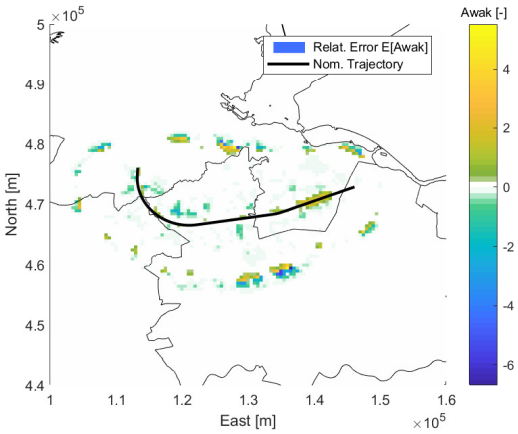

Figure 6.17: The difference in SEL between the lateral error and nominal track simulation for the ARNEM SID

When analyzing the distribution of the SEL in this case study, the same conclusions as in the first case study can be made. First, the standard deviation of the SEL is higher when closer to the trajectory. For grid points located closer to the beginning of the trajectory, the σ_{SEL} is even higher due the fact the altitude of the aircraft is lower. The bubble effect occurs due the fact the lateral position error is simulated at selected waypoint and the error for intermediate points is determined with an interpolation. Finally, the area located on the outside of the turn has a higher standard deviation than the area located on the inside. All these conclusions are illustrated in Fig. 6.18 and Fig. 6.19.

Last, the probability that awakenings occur when a lateral deviation is present is calculated, since both $\mu_{SEL}^{i,j}$ and $\sigma_{SEL}^{i,j}$ is known. Similar results as for the Spijkerboor case study can be seen in Fig. 6.20, where again for an area close the the trajectory the probability is 100 per cent. Also, in a region located around that area, the probability decreases when increasing the distance to the trajectory. In Fig. 6.21 the relative probability that awakenings occur for the stochastic and deterministic approach are presented. As can be seen, the results are comparable with the results from the first case study. Therefore, the conclusions made in the Spijkerboor case study are confirmed with the findings of the stochastic analysis of the ARNEM departure.

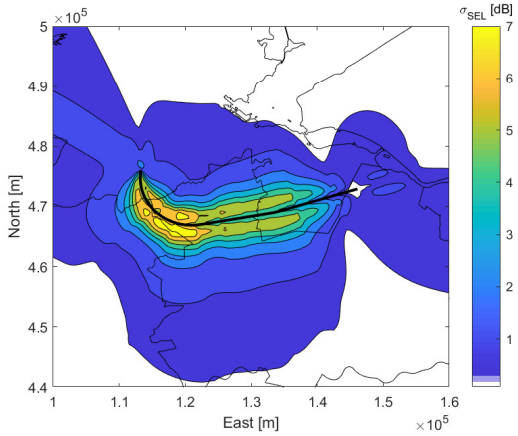

Figure 6.18: The standard deviation of SEL for ARNEM 3E, resulted from the Monte Carlo simulation.

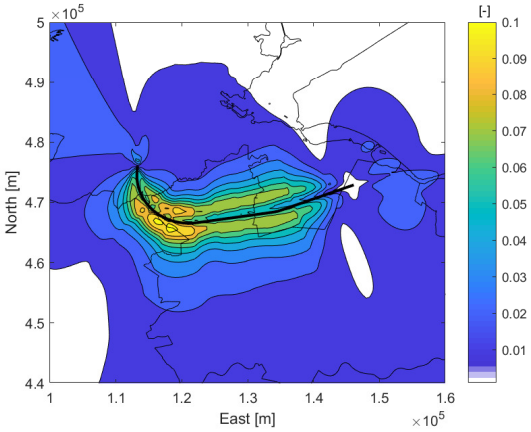

Figure 6.19: The normalized standard deviation divided for ARNEM 3E, resulted from the Monte Carlo simulation

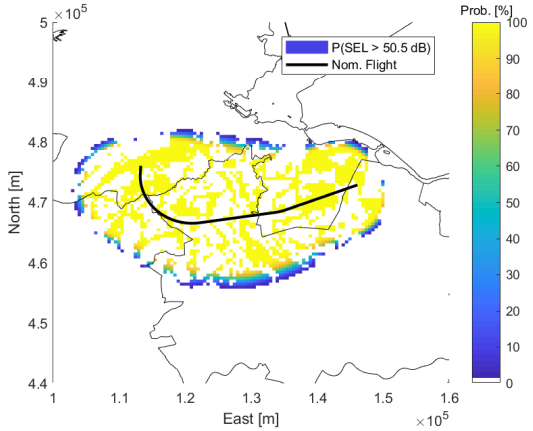

Figure 6.20: Probability that SEL is higher than 50.5 dB as a result of the lateral deviation for the ARNEM 3E SID

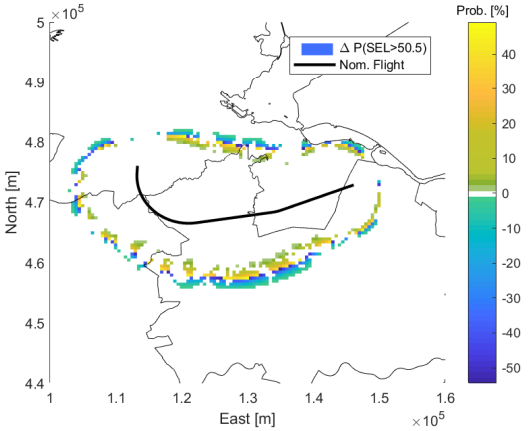

Figure 6.21: Difference in probability that SEL is higher than 50.5 dB for the ARNEM 3E SID

6.3. STOCHASTIC ANALYSIS: INITIAL WEIGHT

Next to the lateral position, a stochastic analysis is performed for the initial aircraft weight. To simulate the effect of the starting weight deviation on the noise impact, the model from Sec. 4.5 is applied for the Spijkerboor 2K SID. As previously stated, a Monte Carlo simulation with a sample size $N = 1500$ will be executed to estimate the distribution of the received noise and the number of awakenings. For the distribution of the initial weight, a normal distribution $N(\mu_W, \sigma_W^2)$ is assumed with an average of $\mu_W = 67164$ kg (0.85 % of MTOW) and a standard deviation $\sigma_W = 2371$ kg (0.03 % of MTOW). The remaining setup of this case study is the same as was presented in Sec. 6.2.1, including the departure route and the population grid.

In Fig. 6.22 the average SEL values resulting from the initial weight distribution simulation are plotted. When comparing it to the SEL values from the nominal trajectory, no significant differences were visible. Just as with the noise calculations for the nominal track, higher SEL values are observed closer to the trajectory and decrease when moving further away from the source.

When analyzing the variance of the SEL caused by the weight distribution, which squared root are plotted in Fig. 6.23, it can be noted that there are some areas present where the SEL can vary. There can be four areas identified where this is true, where the area before the second turn is the largest. To explain why this occurs, the altitude profile and corrected netto thrust profile are plotted for a set of different initial weights in Fig. 6.24 and Fig. 6.25. In both figures it can be seen that the largest differences between the five trajectories occur around a time of 250 seconds. The trajectory with the lowest starting weight reaches the final altitude

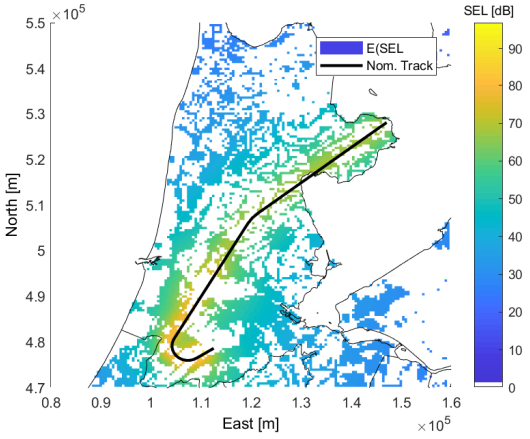

Figure 6.22: The expected SEL values resulted from the Monte Carlo simulation for the initial weight deviation

first and can therefore cut its thrust back earlier. For a heavier aircraft the moment when the final altitude is reached comes later and so the moment when the thrust is changed occurs later. This moment corresponds to the area where the variance of the SEL is high in Fig. 6.23. Before the 250 seconds time mark, there are some smaller differences present in the altitude and thrust profile, which probably correspond to the smaller areas where a variance of SEL is present.

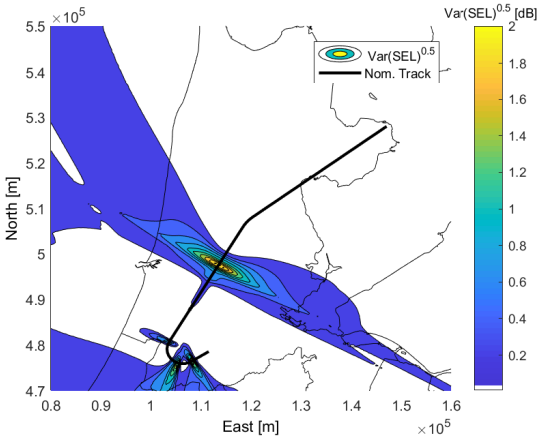

Figure 6.23: The square root of the variance of the SEL resulted from the Monte Carlo simulation for the initial weight.

However, although there are some areas where the SEL deviates, these are small compared to the variance caused by the lateral position deviation. Also the magnitude of the variance is significantly smaller. This results that there are also no large differences present when comparing the number of awakenings for the five trajectories. As can be seen in Tab. 6.4, the variance of the number of awakenings is not significant. Even for the extreme deviated starting weights like the 91 % of MTOW, the difference in awakenings is only 7 %. In comparison to the e lateral position error, the variance causes by the initial weight deviation seems to negligible.

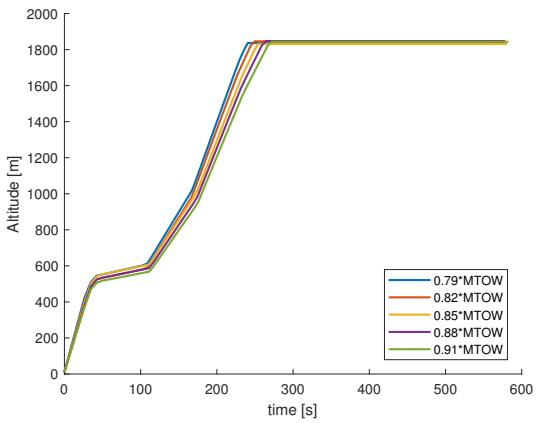

Figure 6.24: The altitude profile for 5 different W_0.

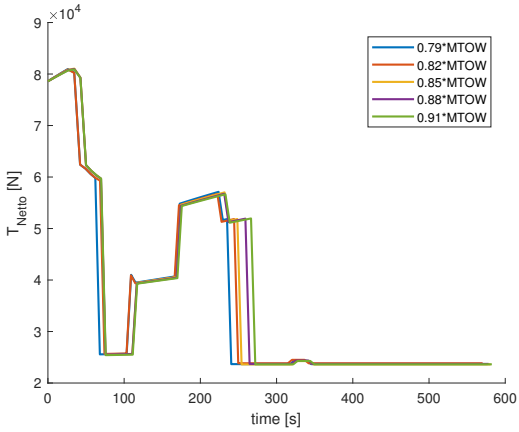

Figure 6.25: The netto correct thrust profile for 5 different W_0.

W_0	Awakenings
0.79 % MTOW	7881
0.82 % MTOW	8184
0.85 % MTOW	8246
0.88 % MTOW	8523
0.91 % MTOW	8863

Table 6.4: The number of awakenings per initial weight W_0 for the Spijkerboor 2K SID

6.4. OPTIMIZATION

Besides the stochastic analysis that was performed, a trajectory optimization shall be executed for both case studies. Although the objectives for the optimization will always be related to the noise and environmental impact, three different optimizations will be set up. The first one will be regarding with the deterministic simulation of the trajectory, similar to the case study performed by Ho-Huu [26]. Here, the objective functions will be the total number of awakenings and the amount of fuel burnt. The constrains and bounds will be based on the ICAO procedures, as was described in Sec. 6.1. For this first optimization, the lateral deviation is not yet taken into account. This multi-objective optimization problem can then be stated as follows:

$$\begin{aligned} \min_{\bar{\mathbf{x}},\gamma_{\mathbf{n}},\eta_{\mathbf{n}}}: \quad & \{\text{Awak}, \text{Fuel}\} \\ & \mu \leq \mu_{\max} \\ \text{s.t.} \quad & h_{\text{f}} = 6000\text{ft} \\ & V_{\text{EAS,f}} = 250\text{kts} \end{aligned} \tag{6.1}$$

The second optimization will take into account the lateral position error and its effect on the noise impact. Therefore, the noise related objective criteria will be the total expected number of awakenings E[Awak]. The emission related objective will remain the total amount fuel burnt, since it is assumed the deviation in lateral position will not effect the fuel consumption. Furthermore, the same set of boundaries and constraints are used as for the first optimization. The optimization problem statement then becomes:

$$\begin{aligned} \min_{\bar{\mathbf{x}},\gamma_{\mathbf{n}},\eta_{\mathbf{n}}}: \quad & \{\text{E[Awak]}, \text{Fuel}\} \\ & \mu \leq \mu_{\max} \\ \text{s.t.} \quad & h_{\text{f}} = 6000\text{ft} \\ & V_{\text{EAS,f}} = 250\text{kts} \end{aligned} \tag{6.2}$$

For the third optimization, the lateral position error is again taken into account, but the expect value of the number of awakenings will not be an objective criteria related to noise. Here, the attempt will be made to optimize for the number of awakenings where 90 % of the awakenings is equal or lower than that value. This value will then be equal to the Z-score corresponding to this left side 90 % confidence level. In this case $Z_{0.9}^{\text{Awak}} \approx 1.28$, which means that the objective value will be: $\text{E[Awak]} + 1.28\sigma_{\text{Awak}}$. The second objective function, the constrains and the bounds will remain the same as for the other two optimizations, so the problem can be stated as follows:

$$\begin{aligned} \min_{\bar{\mathbf{x}},\gamma_{\mathbf{n}},\eta_{\mathbf{n}}}: \quad & \{\text{E[Awak]} + 1.28\sigma_{\text{Awak}}, \text{Fuel}\} \\ & \mu \leq \mu_{\max} \\ \text{s.t.} \quad & h_{\text{f}} = 6000\text{ft} \\ & V_{\text{EAS,f}} = 250\text{kts} \end{aligned} \tag{6.3}$$

In the end, the three optimization problems will only differ in the objective criterion related to the noise impact and to the simulation of that noise impact. The second criterion regarding the fuel consumption will be the same for all three problems.

Although Sec. 4.5 described the approach to determine a noise related objective function which takes into account possible deviation of the starting weight, the decision was made not to perform a case study for that optimization problem (Eq. 4.31). As was concluded in Sec. 6.3, the effect of varying the initial weight on the number of awakenings was less than previously anticipated. To then apply the methodology presented in Sec 4.5, which requires Q times a trajectory and noise impact simulation, would not be beneficial. Therefore, the case studies for this research are only optimized with stochastic objective function related to the lateral deviation, not the aircrafts initial weight.

Regarding the settings of the MOEA/D, the parameters are selected so that the optimization algorithm will almost definitely converges to a set of optimal solutions, while limiting the computational time. The population size is normally twice the solution size, so it set to 50 for this optimization. A high mating neighborhood size ensures diversity in the generation of solutions, but also increases the computational cost. A large size of replacements neighborhood will help ensuring the convergence of the optimization, but also effects the computational cost. The maximum iteration is basically just an assumption on when the algorithm would be finished. Therefore, the selection of these parameters is based on a trail and error approach and can be found in Tab. 6.5.

Parameter	Value
Population size : Pop	50 [-]
Mating neighborhood size : T_m	15 [-]
Size of replacement neighborhood : T_r	10 [-]
Maximum iteration : $MaxIter$	1000 [-]

Table 6.5: Parameters settings for the MOEA/D

The three optimization problems will be solved and its results compared for both the Spijkerboor 2K and the ARNEM 3E case study. For the remaining of this chapter, the first problem with the deterministic simulation and optimization approach will be denotes simply as 'Det'. The second approach, with the stochastic simulation and the optimization that has the expected number of awakenings as objective criterion, will be denotes as 'Sto'. Finally, the third problem, with has the stochastic simulation but optimizes for the $Z_{0.9}^{\text{Awak}}$ value, will be referred to as 'StoZ'.

6.4.1. SPIJKERBOOR 2K

With the multi-objective optimization problems as previously described executed for the Spijkerboor case study, the obtained Pareto fronts can be compared. First, the optimal solutions from the deterministic approach (Eq. 6.1) will be compared with the ones from the stochastic approach where is optimized for the expected number of awakenings (Eq. 6.2). Both the Pareto fronts, containing all the optimal solutions, are shown in Fig. 6.28.

Although the objective functions for the noise impact are not the same, the fronts seem to be almost identical. Both exist of three separate curves, corresponding to the three groups of optimal trajectories. The reason that the optimal solutions are so close together is that when the noise impact of a trajectory is determined with a deterministic and a stochastic approach, the results will not differ significantly. To check if the trajectories of two identical solution are also similar, a test Case A is selected to compare the solutions. Since the criterion for the emission impact is for both optimization the same, two solutions will be selected with the same amount of fuel burnt. See Fig. 6.28 for where the solutions are location on the Pareto front. Both trajectories have a fuel consumption of 705 kg, where the deterministic solution has 2964 Awakenings and the stochastic one

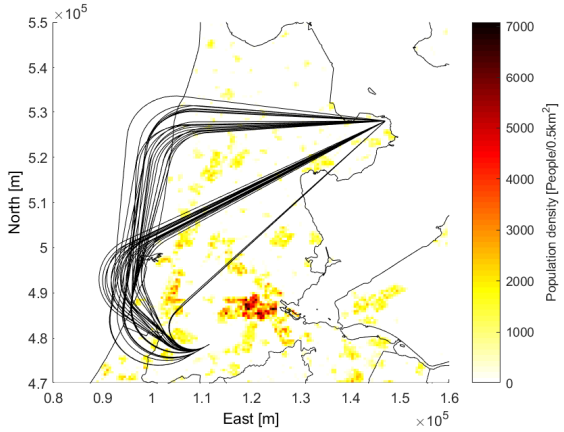

Figure 6.26: Optimal ground tracks from the deterministic (Det) approach.

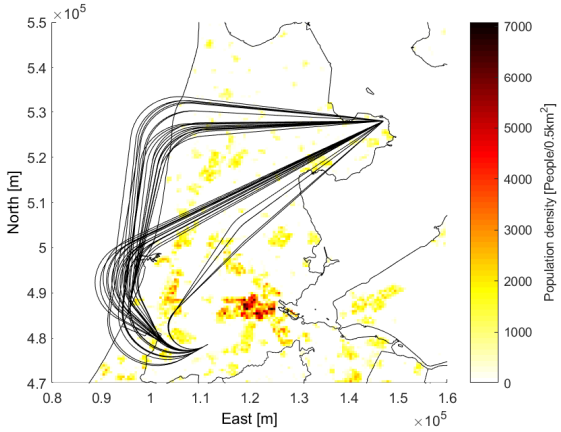

Figure 6.27: Optimal ground tracks from the first stochastic (Sto) approach.

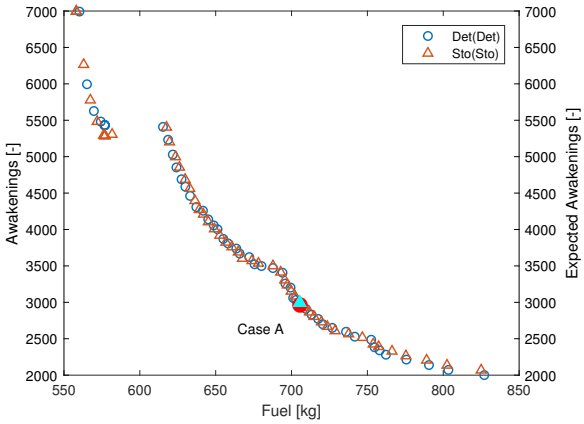

Figure 6.28: The Pareto fronts for the deterministic results obtained with the deterministic objective function and the stochastic results obtained the stochastic objective function.

has 2994. The solutions from Case A also do not differ significantly with respect to awakenings. Therefore, it would be expected that the trajectories are similar to each other. When comparing the ground tracks in Fig. 6.29, it can be seen this is true. The same applies for the airspeed profiles, plotted in Fig. 6.30. There is a small difference in altitude profiles visible, which could explain the 30 awakenings difference. Overall however, the trajectories are almost identical, while being the result of two different optimization approaches.

Now that the sets of optimal solutions are compared with their respectively objectives criteria, they will also be compared with the same criteria. First, the 'Det' and 'Sto' solutions will both simulated with the stochastic approach and the expected number of awakenings will be objective criterion related to the noise impact. The Pareto fronts are plotted in Fig. 6.31.

As can be seen, the stochastic simulation results with the deterministic set of solutions is almost identical to the stochastic optimization approach. The same three curves can be identified, just as for the first comparison. To again check if the trajectories are similar when their solutions are identical, test Case B is selected. The amount of fuel consumed for both solutions is equal to 633 kg. The expected awakenings for the 'Det' and 'Sto' solutions is 4545 and 4562 respectively. Here, the expected numbers of awakenings almost do not differ, which is understandable when the trajectories are compared. Although the first turn is a little bit different, the ground tracks are very similar as can be seen in Fig. 6.32. For the altitude and airspeed profile of Case B, presented in Fig. 6.33, also no significant differences are present.

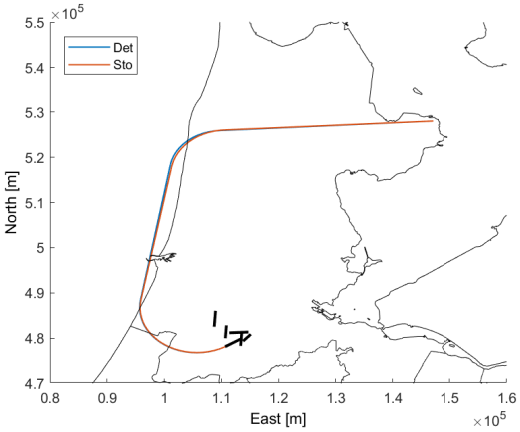

Figure 6.29: The ground tracks for the solutions of test Case A.

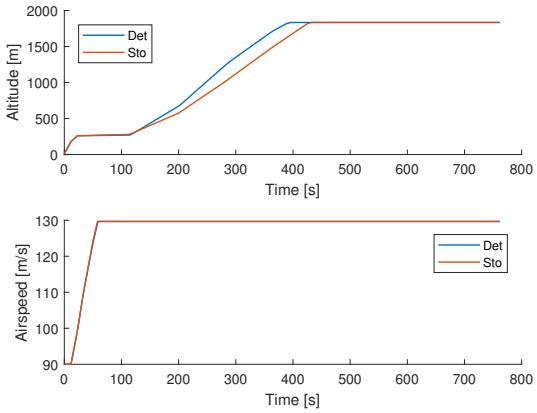

Figure 6.30: The altitude and airspeed profiles for test Case A.

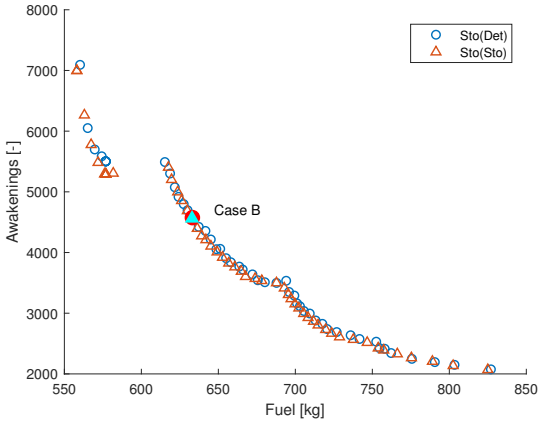

Figure 6.31: The Pareto fronts for the stochastic results obtained with the deterministic objective function and the stochastic results obtained with the stochastic objective function.

The two solution sets are also compared by using the deterministic simulation approach. The 'Sto' set of solutions are simulated with the same approach as was used in the deterministic optimization and compared with the original solutions from that optimization. The Pareto front for both sets are plotted in Fig. 6.34.

For the most part, both set of solutions are close together. However, in the region where the fuel consumption is low, some differences occur. The biggest difference in number of awakenings is at the illustrated Case C, where the amount of fuel burnt for both solutions is equal to 577 kg. A number of 5432 awakenings is calculated the deterministic solution, while the stochastic solution has a number of 5208 awakenings. Although this difference of 224 is still not that significant, it is quite bigger than for the different comparisons. To see where this difference comes from, the ground track for both solutions is plotted in Fig. 6.35. Here, the 'Sto' solution has a small deviation to left with respect to the 'Det' solution, but for the remaining of the trajectory is similar.

When comparing the altitude and airspeed profiles , seen in Fig. 6.36, they appear to be almost identical. Only at the end of the trajectories, the altitudes differ slightly. Therefore, it can be concluded that the trajectories are almost identical. The reason for that a relatively big difference in number of awakenings occur is because the trajectories pass directly over a highly population area. This makes the total noise impact sensitive for small deviation in the departure.

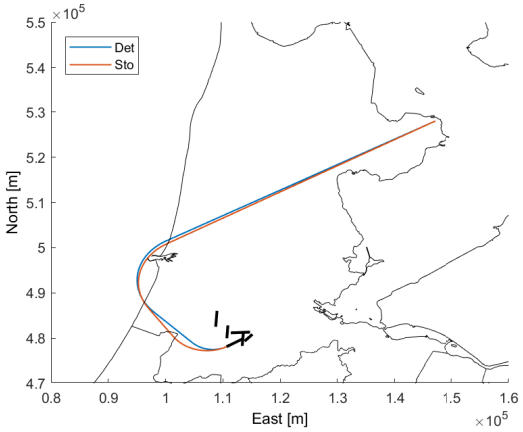

Figure 6.32: The ground tracks for the solutions of test Case B.

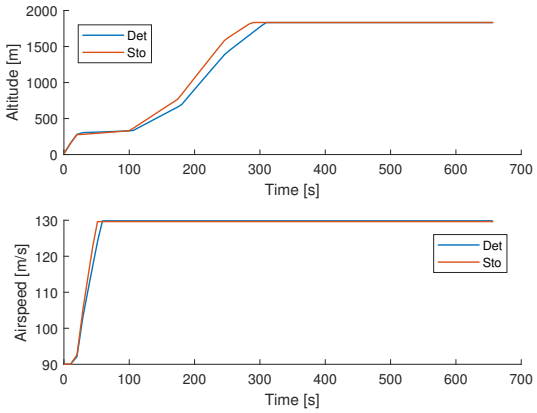

Figure 6.33: The altitude and airspeed profiles for test Case B.

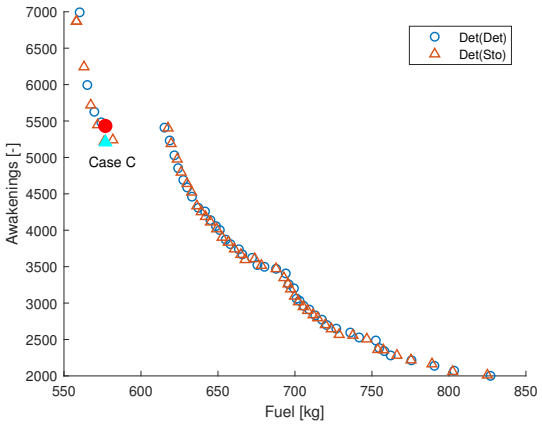

Figure 6.34: The Pareto fronts for the stochastic results obtained with the deterministic optimization and the stochastic results obtained with the stochastic objective function.

The ground track results obtained when optimizing for the Z-score corresponding to a 90 per cent confidence level, see Eq. 6.3, are plotted in Fig. 6.37. Just as in the first to optimization approaches, the solutions are be divided in three groups. Although almost no difference are spotted for the other two groups, there are some other trajectories for the minimum fuel consumption ground tracks. This could be explained by the fact that the objective criteria for noise is now E[Awak] + $1.28\sigma_{\text{Awak}}$ instead of just the E[Awak], which makes the algorithm try to avoid trajectories where the standard deviation for the number of awakenings is high. This σ_{Awak} is naturally higher for tracks which fly over populated areas. Therefore, the trajectories from the minimum fuel group deviate more away from the city of Amsterdam, which is of course a highly populated area.

Overall, the ground track solutions are similar to the solutions obtained with the previous optimizations. This is also made clear when comparing the Pareto fronts. The solutions from this and the deterministic optimization are compared for their deterministic simulation results (Det) and for their Z-score $Z_{0.9}^{\text{Awak}}$ (StoZ) approach, see Fig. 6.38 and Fig. 6.39 respectively. Again, no significant difference can be seen when comparing the Pareto fronts, with all solutions located on the same three curves. Therefore, it can be concluded that for this case study, the results are all similar for different noise related objective criteria.

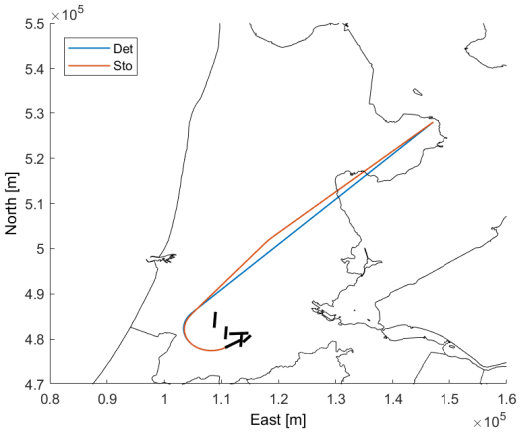

Figure 6.35: The ground tracks for the solutions of test Case C.

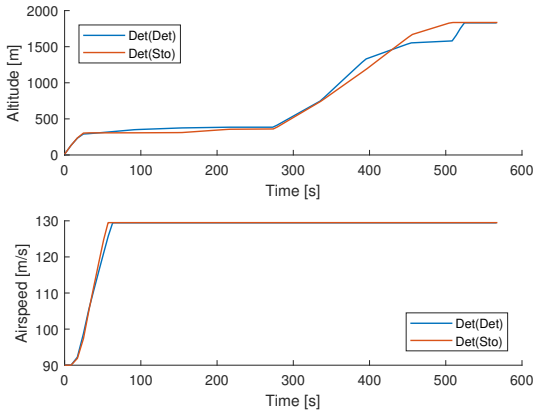

Figure 6.36: The altitude and airspeed profiles for test Case C.

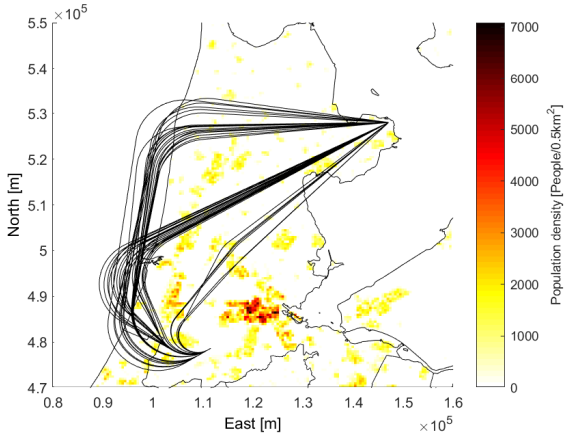

Figure 6.37: Optimal ground tracks obtained with the second stochastic (StoZ) objective function.

6.4.2. ARNEM 3E

The three described optimization problems will be solved again for the ARNEM 3E case study. The optimal ground tracks for the first two optimization problems, optimized for the deterministic number of awakenings 6.1 and expected number of awakenings 6.2, are presented in Fig. 6.40 and 6.41.

Although the constrains would allow for different trajectories, the optimal solutions all follow almost the same departure route. Without just a couple of exceptions from the deterministic optimization, all solution have such a heading change $\Delta\chi_2$ in the first turn, so that a second turn can almost be avoided. Secondly, the ground tracks solutions where is optimized for the expected number of awakenings are located much closer together with respect to the deterministic solutions, where a wider spread is present. Since that the stochastic approach takes into account lateral deviation, the expected number of awakenings increase more when the departure gets closer to an highly populated area. So, in this case study, the optimization algorithm attempts to find a solution located as far possible from the cities located left (Amsterdam) and right (Utrecht) from the trajectory. Therefore, the spread in ground tracks is less than with the optimization for the deterministic number of awakenings.

This however does not result in significant differences in the Pareto fronts of both optimizations, as can be seen in Fig. 6.42. In all three comparisons, the Pareto fronts exists of one continuous curve similar to each other. There are some small differences noticeable when comparing the deterministic number of awakenings with the expected ones, but these are not considered significant.

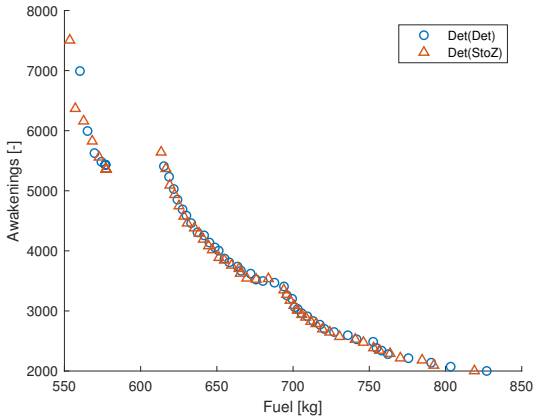

Figure 6.38: Pareto fronts for deterministic solution from the DET objective function and deterministic solution from the StoZ objective function

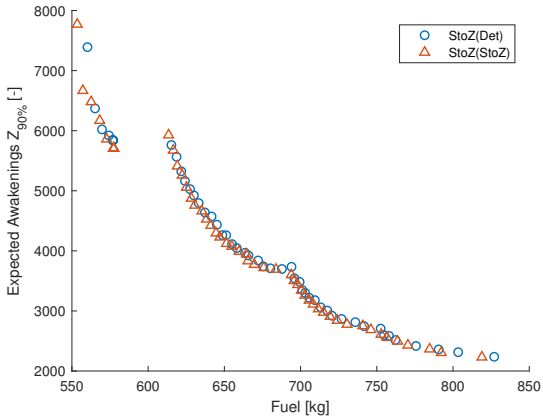

Figure 6.39: Pareto fronts for stochastic 1 Z-score solution from DET objective function and stochastic Z-score 1 solution form StoZ objective function

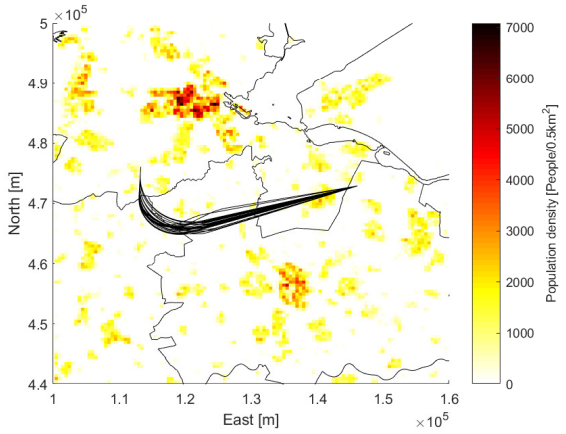

Figure 6.40: Optimal ground tracks from the deterministic (Det) approach (ARNEM)

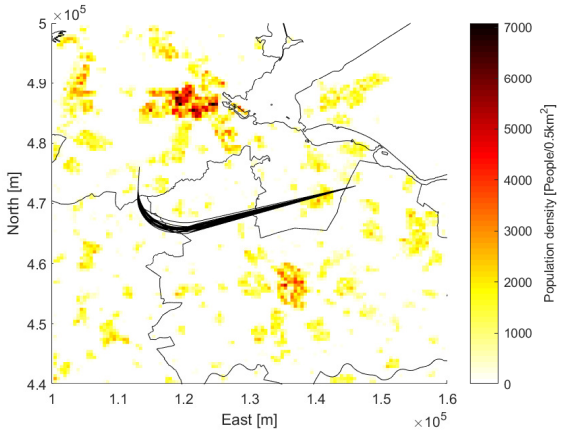

Figure 6.41: Optimal ground tracks from the first stochastic (Sto) approach (ARNEM)

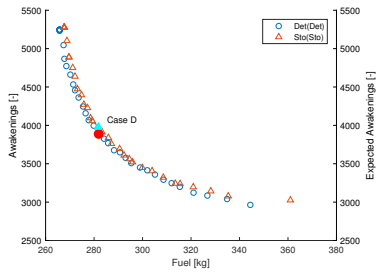

(a) Deterministic with Det and stochastic with Sto results

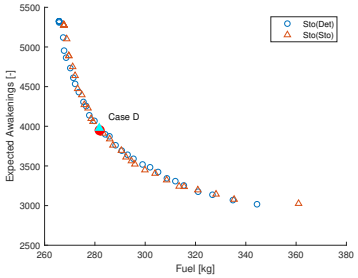

(b) Stochastic results for Det and Sto solutions

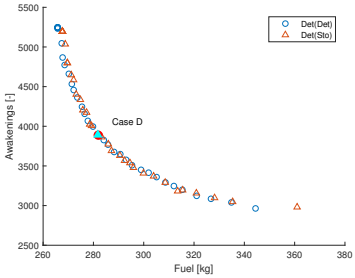

(c) Deterministic results for Det and Sto solutions

Figure 6.42: Deterministic and stochastic optimization results for the ARNEM 3E case study, compared with both simulation methods (ARNEM)

To confirm that the solutions for both optimization approaches are indeed similar, two trajectories from each approach will be compared and are highlighted in Fig. 6.42.The comparison is done for solutions with same amount of fuel, since these amounts are determined with the same method in both optimizations. For this test case D, the amount of fuel burnt for both solutions is 282 kg, where the deterministic number of awakenings is equal to 3888 and the stochastic solution has 3977 expected number of awakenings. When the two

solutions are compared with the same simulation approach, the noise impact results are close to each other as can be seen in Fig. 6.42b and 6.42c. This can be expected when the ground tracks for the two trajectories would be compared, which are plotted in Fig. 6.43. Expect for the radius of the first turn R_2, the two ground tracks seem to be identical. The vertical and airspeed profile, plotted in Fig. 6.44 also have no significant differences. So, optimizing for the expected number of awakenings in does not result in new solutions, in respect to optimizing to the deterministic number of awakenings. However, taken into account the lateral deviation results in trajectories which are located closer together.

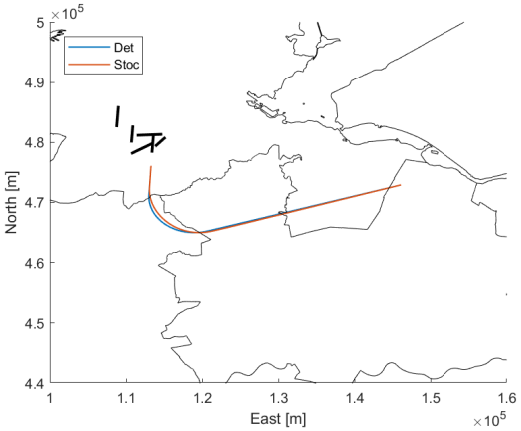

Figure 6.43: The ground tracks for the solutions of test Case D.

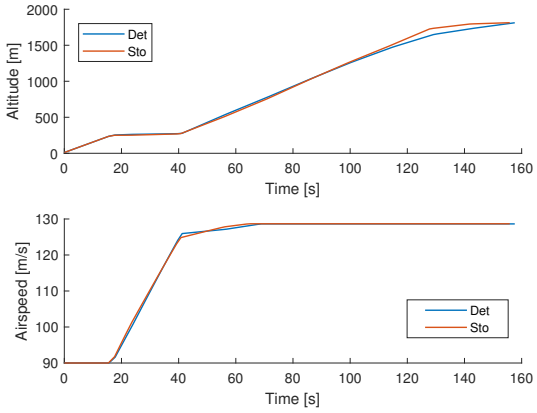

Figure 6.44: The altitude and airspeed profiles for test Case D.

To check what the influence will be when optimizing for the number of awakenings where 90 per cent is equal or lower than that number, the third optimizing problem 6.3 will also be solved for the ARNEM 3E departure route. The optimal ground tracks are presented in Fig. 6.45. Although the departure is optimized for a different noise related objective function, the results do not differ much with ground tracks from the previous two optimizations. The first turn is again selected in such a way that the aircraft can fly straight to the IVLUT waypoint. Also, the ground tracks are less spread out that for the ones from the deterministic optimization (Fig. 6.40). When comparing the Pareto front obtained with this optimization with the ones from the deterministic approach, there are almost no differences visible. As can be seen in Fig. 6.46 and 6.47, both fronts seems to be on the same curve.

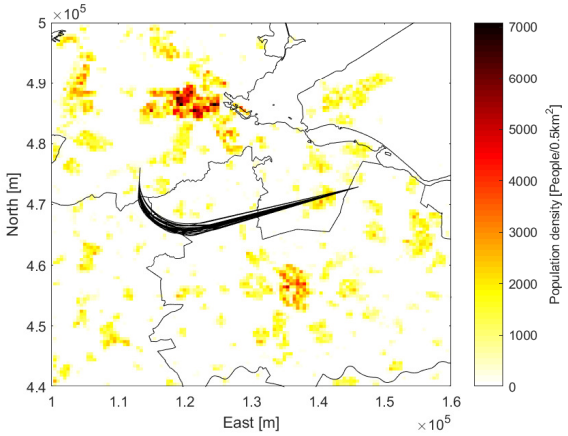

Figure 6.45: Optimal ground tracks from the second stochasti (StoZ) approach (ARNEM)

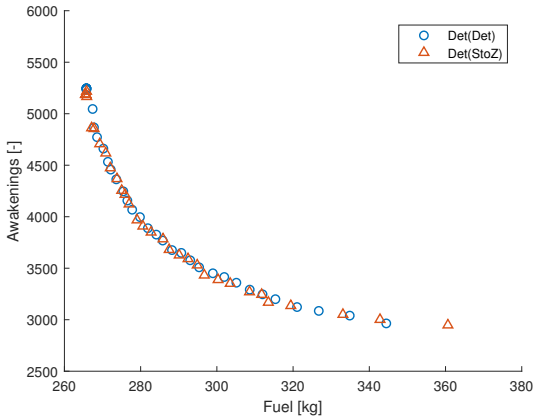

Figure 6.46: Pareto fronts for deterministic solution from the Det objective function and deterministic solution from the StoZ objective function (ARNEM)

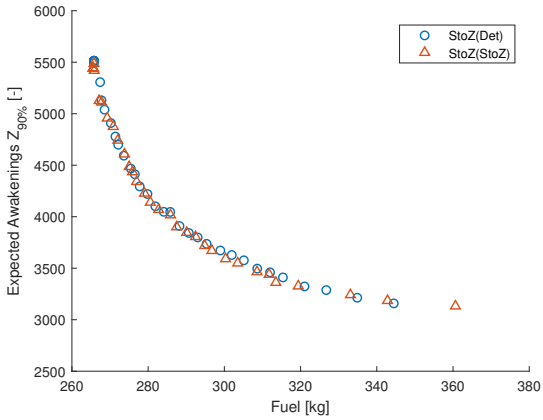

Figure 6.47: Pareto fronts for stochastic 1 Z-score solution from the Det objective function and stochastic Z-score 1 solution from the StoZ objective function (ARNEM)

In conclusion, the additional case study of optimizing the ARNEM 3E SID confirms the findings from the previous study. Optimizing for a stochastic noise objective function does not result in new solutions or neglecting existing ones. However, this case study shows that when lateral deviation is implemented within the optimization, solutions seems to more converged to each other. Apparently, due to the fact that the departure flies between two inhabited areas, the algorithm prefers to be further away from those areas when optimizing for the expected number of awakenings. Therefore, although no new solutions are found, some solutions seems to be more suited when taken into account the lateral variation.

6.5. ADJUSTED CASE STUDY

In all previously described case studies, the noise impact is quantified with the use of the ANSI criterion function [2], presented in Eq. 2.21. This is in contrast with previous noise abatement studies([27],[10]), where the FICAN criterion function [3] was applied . Although both functions have a different shape, the principle of them is similar. When the received SEL at a grid point is higher than a certain cutoff value, the percentage of awakenings that can occur there will be determined according to some curve. For the FICAN function, this cutoff $SEL_{Outdoor}$ value was 50.5 dB, meaning that no awakenings occur at locations were the received SEL is lower than that value. In this research, the same cutoff value was assumed for the ANSI function. However, after performing the case studies, it was discovered that this assumption was incorrect and that the cutoff should be equal to 65 dB. An outdoor received SEL of 65 dB corrected gives a SEL_{Indoor} of 50 dB, which is almost equal to the outdoor cutoff value of the FICAN function and was therefore probably the cause of the confusion. Both ANSI curves, with the correct and incorrect cutoff value are plotted in Fig. 6.48.

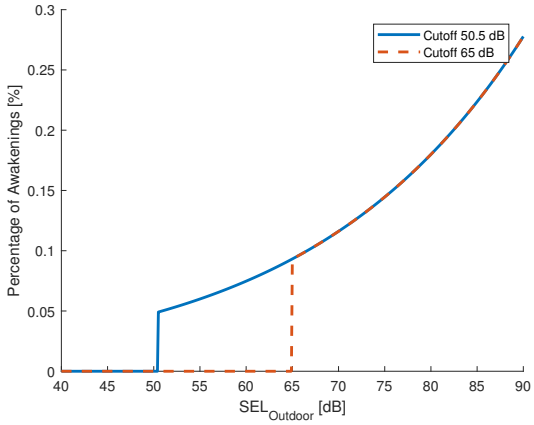

Figure 6.48: The ANSI curve plotted for both the correct and incorrect cutoff values.

Although the incorrect cutoff value was used in previous cases, the methodology used there still holds up. Using the incorrect value only affects the noise related objective function and not the simulation of the trajectory, lateral position error or the noise impact. Therefore, most of the obtained results are still valid and relevant. In the stochastic analysis of the lateral position error, the findings regarding the received SEL are not affected. However, the number of awakenings determined for the two cutoff values will be quite different. For the Spijkerboor 2K SID, the number of awakenings obtained with both the deterministic and the stochastic simulation are compared with the results obtained with correct cutoff value of 65 dB in Tab. 6.6.

Cutoff SEL	Awak	E(Awak)
50.5 dB	8297	8246
65 dB	4118	4696

Table 6.6: Awakenings results for both the deterministic and stochastic simulation for the two different cutoff SEL values

As expected, there are significant less awakenings when the new cutoff value of 65 dB is used, which can be explained when analyzing the differences in two curves in Fig. 6.48. In the range between 50.5 and 65 dB, where originally awakening could occur, the percentage now is set to zero. When comparing the expected number of awakenings resulting from the stochastic analysis with the deterministic results, there was no significant difference present when the incorrect cutoff value was used. However, when the $SEL_{Outdoor}$ of 65 dB is used, the difference is definitely significant. At first, when analyzing the difference in probability when the received SEL is higher than 65 dB, see Fig. 6.49, it looks like the area where the SEL is underestimated cancels out the area where it is overestimated. The only difference with the incorrect cutoff value is that the affected areas are now closer to the nominal trajectory. However, due to the fact that the cutoff is at a higher SEL, the jump between no percentage of awakenings to a percentage is also bigger. At 50.5 dB the difference in percentage is around 0.05 %, while at 65 dB this is almost 0.1 %. In highly populated areas, where for the

deterministic simulation no awakenings were considered, but could be possible in the stochastic approach, this jump in percentage could result in a lot more awakenings. Basically, this higher cutoff value results larger differences between first zero awakenings and the now possible number of awakenings. This can also be seen when the absolute difference between the deterministic number of awakenings and the expected number of awakenings is plotted, as in Fig. 6.50.

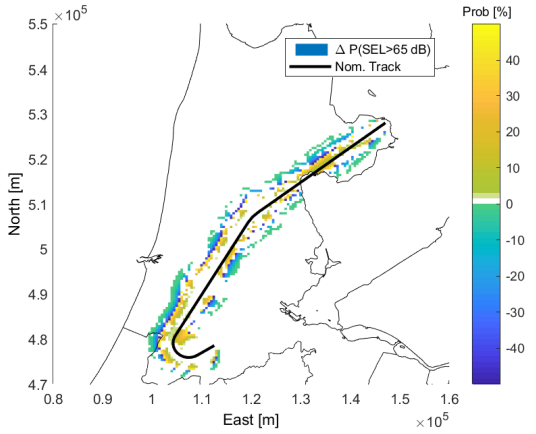

Figure 6.49: The difference in probability that SEL is higher than 65 dB for the Spijkerboor SID

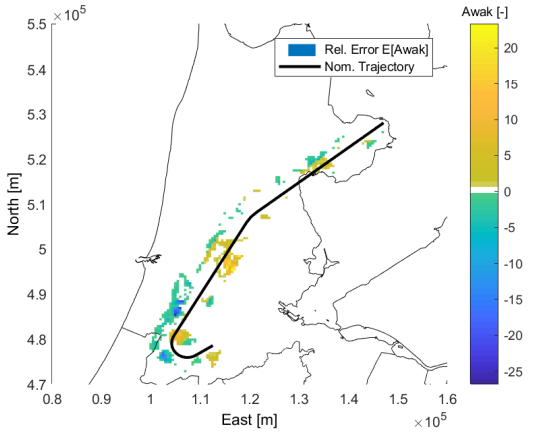

Figure 6.50: The difference in Awak between the lateral error and nominal track simulation for the adjusted case study

Since that for a cutoff SEL of 65 dB the difference between the deterministic and stochastic noise objective function could differ significantly, the case study presented in Sec. 6.2.1 will again be performed. Here, the Spijkerboor 2K departure route of AAS will be optimized for both the number of awakenings and the amount of fuel burnt, see Eq. 3.36 and Eq. 4.25 for the formulation of both the optimization problems. Next to the different cutoff value, the case study is completely the same as described in Sec. 6.2.1.

The ground tracks of the optimal solutions for the deterministic noise objective function are plotted in Fig. 6.51. In contrast to the results from the previous optimization (Fig. 6.26) a large part of the solutions are clustered together, flying around Haarlem and then continuing directly to the ANDIK waypoint. The second smaller cluster takes the shortest route to the waypoint and therefore consumes less fuel but causes more awakenings than the other trajectories. The overseas route, which was present in the previous optimization, is now not considered to be an optimal departure. The results from the stochastic noise objective function are plotted in Fig. 6.52, where the ground tracks can be divided into four groups. Apparently, considering the lateral position error now does affect the optimization and results in new departures which were not considered with the deterministic objective function.

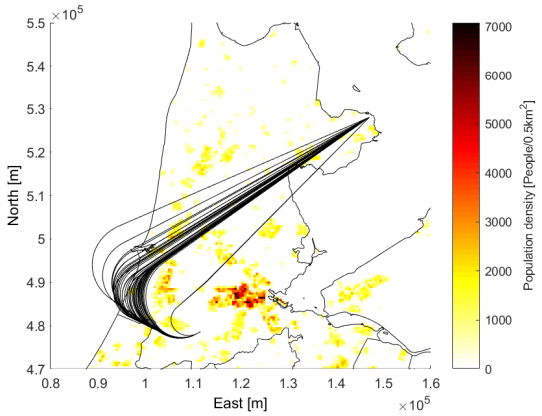

Figure 6.51: Optimal ground tracks from the adjusted deterministic approach

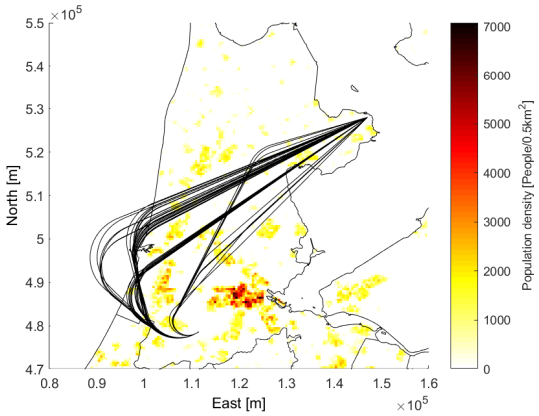

Figure 6.52: Optimal ground tracks from the adjusted stochastic approach

When analyzing the Pareto fronts for both optimizations, the previously identified clusters are visible. For

the deterministic solutions, as can be seen in Fig. 6.53, there is a short curve located at the minimum fuel solutions and large curve containing the remaining solutions. The four clusters of the stochastic results can also be identified in the deterministic Pareto front. When comparing the Pareto fronts obtained with both optimizations for the deterministic objective function, parts of the curve overlap each other, while other parts are on a different curve. Nevertheless, neither the deterministic nor the stochastic solutions out perform each other in this comparison. When the fronts are plotted for the stochastic objective function (E[Awak]), which can be seen in Fig. 6.54, some of the stochastic solutions score better with respect to expected number of awakenings than the solutions obtained with the deterministic approach. A clear difference is visible around 640 kg of fuel consumed and 1200 expected number of awakenings, where the deterministic curve almost goes horizontal for a bit, instead of following the optimal curve from the stochastic solutions.

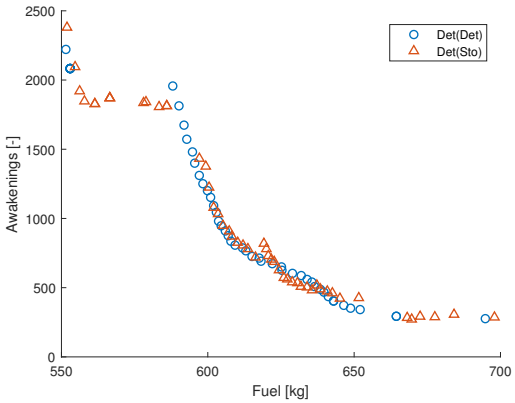

Figure 6.53: The deterministic simulated Pareto fronts obtained with the deterministic and stochastic objective function for the adjusted case study

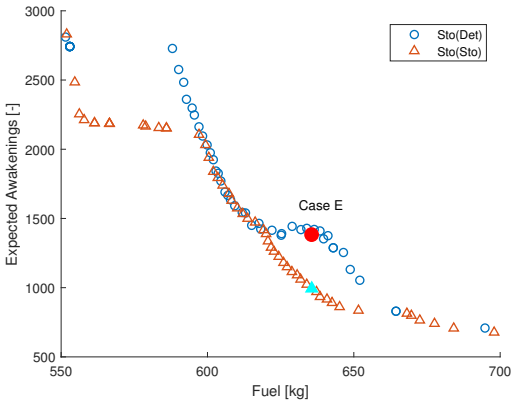

Figure 6.54: The stochastic simulated Pareto fronts obtained with the deterministic and stochastic objective function for the adjusted case study

To investigate what occurs in that region, a test case E is set up, where a deterministic and stochastic solution with the same amount of fuel burnt are compared. Both solutions consume around 635 kg of fuel, while the expected number of awakenings of the stochastic and deterministic solution are respectively 994 and 1383. These significant differs can be explained when the ground tracks of both solutions are compared, which is done in Fig. 6.55. Although the total distance flown and end time are almost identical, both tracks operate on a different ground track. Also, when the altitude profiles are compared in Fig.6.56, a significant different departure approach is selected by both solutions. The deterministic solutions starts the climb to the final altitude earlier, but is still causing more awakenings due to that a different ground track is selected. There are almost no differences seen in the airspeed profiles, which is expected since both the amount fuel consumed and the duration of the departure are identical.

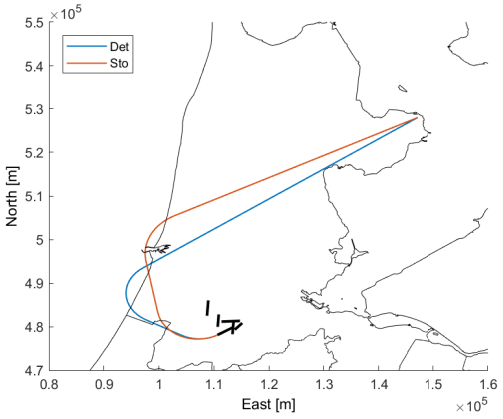

Figure 6.55: The ground tracks solutions for test case E

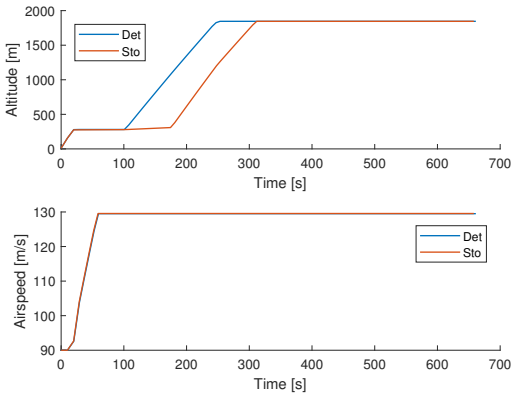

Figure 6.56: The altitude and airspeed profiles for test case E

Although the cutoff value has no direct influences on the methodology used in this research, it can have

an effect on the results. This is mainly due to the fact the objective function related to the noise impact is determined differently. Since the correct cutoff value is now at 65 dB, a smaller area can be awoken by a single departure, and so the total number of awakenings is smaller. However, a higher cutoff value results in a larger difference between no or some awakenings. Therefore, during the stochastic analysis of the lateral position error, expected number of awakenings can be significantly higher than for the deterministic simulation. This has than naturally an effect on the optimization for a stochastic noise objective function, which resulted in this case study for a new set of optimal solutions. If the optimization for this objective functions comes up with new solutions is highly depending on the case study itself. Depending on how the population density or the grid size would change, the effect of a higher cutoff value for the ANSI curve could be less or more.

7

CONCLUSIONS AND RECOMMENDATIONS

The objective of this research was stated, which was to develop an optimization algorithm for designing terminal departures procedures which can implement the stochastic behavior of aircraft state variables. Next to the main research objective, several sub-questions were formulated. To answers these questions, multiple case studies were performed in this research. The conclusions drawn from the case studies will be discussed in this chapter, as well the possible recommendations for future researches.

7.1. CONCLUSIONS

The main objective for this research was to answer the following question:

> **"How can the stochastic behavior of aircraft state variables be modeled within the optimization of terminal departures, related to noise and economic factors?"**

This was achieved by first developing a deterministic trajectory simulation model, which could determine the environmental impact. By combining a 2D intermediate-point mass aircraft model with the parameterization technique, it was possible to define the required aircraft states of a complete trajectory. The emission impact resulted from solving the ODEs and with the use of an INM and a GIS, the noise impact could be determined. Both the noise and the emission impact were the objective criteria for the multi-objective evolutionary algorithm based on decomposition, so the optimal departures could be found. Next to that, a stochastic model was developed to simulate the uncertainty of the lateral position. With the use of the Monte Carlo simulation, the effect of this lateral variation on the noise impact was be estimated. For the lateral position error, a normal distribution was assumed based on the RNP requirements. Due to the fact that it was desired to consider this stochastic noise impact in the optimization, an additional function was developed to approximate that same effect. This approximation function could generate results accurate enough to be compared with the ones obtained with the Monte Carlo simulation, but for a significant less computational cost. To see what the effect would be when different state variables show stochastic behavior, a similar approach is used to model the initial aircraft weight deviation. The optimization algorithm, both with the deterministic and stochastic noise impact, was verified and applied successfully in two case studies. Therefore, it can be concluded that as well the main research question, as well as the sub-questions, were answered.

Multiple findings were noticed related to the effect of lateral deviation on the noise impact when additional stochastic analyses were performed. The first thing that stood out, when comparing the SEL results from the Monte Carlo simulation with the deterministic results, was that close to the trajectory the SEL values from the stochastic simulation were lower than the deterministic values and further away slightly higher. The area of where the expected SEL was lower matches the bounds of the RNP 1. This is understandable, since in that area the aircraft can deviate further away from the observers with respect to the nominal trajectory. For the remaining area the expected SEL values are slightly higher due the fact that it is possible that the aircraft deviates somewhat closer to the observer than normally.

The KS-test showed that when the lateral position error is simulated as a normal distribution, the SEL is normal distributed, expect for the region close to the trajectory. Here the test fails due to the fact that, when the

observer is located close to the nominal trajectory (≈ 2.8 km), deviation of the aircraft cannot always result in higher SEL values. The maximum SEL is experienced when the observer is directly underneath the track, so lateral deviation here will only result in lower SEL values, since the aircraft can only deviate further away from the observer. Therefore a correction method was developed and applied at further noise impact calculations. For the standard deviation of the distribution, it is clear that it increases for observers closer to the nominal trajectory. Additional increase occurs for observers located on the outer side of a turn segment. For observers located on the inner side of a turn segment, the standard deviations decrease when compared to observers close to a straight segment.

When comparing the total expected number of awakenings with the number of awakenings resulting from the deterministic simulation, the differences seems to almost negligible. However, when analyzing the awakenings per observer point, significant differences were present. These relative differences cancel each other out when only the total number of awakenings are compared, as that for some observers the deterministic number of awakenings can be over or under estimated. This also showed when comparing the probability when awakenings could occur per observer, so the probability that the SEL is equal or higher than the threshold value of 50.5 dB. The effected regions became clearly visible and it seemed that the overestimated area was comparable to the under estimated area. Therefore, the stochastic noise impact did differ from the deterministic impact, but is not noticeable when evaluating just the total of awakenings.

This phenomenon could also be an explanation that there were almost no differences in results with the optimizations for the deterministic and stochastic noise impact. In both case studies, nor any additional solutions were found nor were existing solutions more or less preferable. Even when the noise related objective criteria is the Z-score corresponding to the 90 % left sided confidence interval, no differences in the Pareto front were observed. However, when analyzing just the ground track solutions which fly by inhabited communities, the solutions tend to be located further away from the communities. When the ground tracks fly between two inhabited areas, the solutions tend to be less spread out when there is optimized for the stochastic noise impact.

Since the ANSI curve helps determining both the deterministic and stochastic total number of awakenings, it has an important contribution to the noise related objective function and so the optimization results. The curve itself has a certain cutoff value and the SEL at the receiver is lower than that value, no awakenings are assumed. So, when for the adjusted case study of the Spijkerboor 2K departure a higher cutoff value was used, the results changed significantly. Not only differed the deterministic number of awakenings with the expected number of awakenings due to lateral deviation, different Pareto fronts resulted from the deterministic and stochastic objective functions. This could be explained by that for a higher cutoff value, the difference in percentages that awakenings could occur, or not, gets larger. Therefore, it can be stated that it is possible that the lateral deviation affects the results of the optimization, but the extend to which it affects depends on several characteristics of the case study.

When a Monte Carlo simulation was conducted to determine the effect of the initial weight deviation on the noise impact, it became clear that this was less than for the lateral position deviation. Apparently, varying the starting weight only influences the performances at moments in the departure where the aircraft switches between climbing or accelerating settings. For observers located to those points on the trajectory, the SEL shows some variation, but the overall variance of the noise is considered not to be significant when comparing it with the results from the lateral deviation simulation. There was also no direct relation discovered between the initial weight distribution and the distribution of the SEL received at a grid point. Therefore, to include the effect of the initial weight deviation in the objective function, an 'online' method was developed to approximate this effect. However, since this approach significantly increased the computational cost and that the effect on the noise impact was minimal, the decision was mate to neglect the initial weight variation for the optimization of departure procedures.

To conclude, this research successfully developed a multi-objective optimization algorithm where the stochastic behavior of a state variables could be considered. However, as illustrated by the two performed case studies, the benefit of this inclusion is questionable. The effect of optimizing for an noise impact generated by lateral deviation depends mostly on the population density of the affected area and the function on how the noise objective criterion is determined. The location of highly inhabited areas with respect to the departure route influences if the outcome of the optimization could be different. Although, when a stochastic analysis is performed prior to the optimization, some insights could be obtained of the possible effect when stochastic objective function would be used in the optimization. Then, the trade-off could always be made if it would be beneficial to implement the modeling of the lateral position error. When it is deemed to be not, a post-optimization stochastic analysis could also be performed to gain additional insights about the already found optimal departure trajectories.

7.2. RECOMMENDATIONS

This research was able to find and develop an approach to model the stochastic behavior of the lateral position within the optimization of terminal departure routes, but the benefit of this addition was deemed questionable. To ensure for further researches that implementing stochastic behavior of aircraft state variables could be beneficial, some recommendations are made.

First of all, additional analyses of the stochastic behavior of other state variables could be executed. The altitude error is in this research neglected. However, since altitude influences the distribution of the SEL significantly, it could affect the results of the optimization. Secondly, as the INM corrects the finite segments based on the airspeed, this state variable could also influence the noise impact in a way and therefore the optimization.

Due to the fact that the entire noise analysis is based on the INM model, it could be an improvement for the approximation function to somehow integrate the two databases. This would decrease computational cost, as the noise model already has to be executed, but could also increase the accuracy of the SEL distribution approximation.

For the estimation of the awakenings distribution, several significant assumptions were made related to the dependency of SEL distributions at surrounding grid points. Further research in this subject could result in a better understanding of how to compute the distribution for the number of awakenings and gain more insight in the robustness of trajectory. Thereby, when the distribution is more accurate, optimizing for certain left sided Z-score could result in different optimal solutions.

Finally, validation of the stochastic noise impact was lacking in this research. To get an insight in how accurate the stochastic analysis was, flight data could be used to re-simulate the actual noise impact caused by terminal procedures. This would generate a better understanding of how the SEL and number of awakenings are distributed, and how to estimate those.

BIBLIOGRAPHY

[1] *Acoustic weighting curves*. Wikipedia. Nov. 2005. URL: https://en.wikipedia.org/wiki/A-weighting#/media/File:Acoustic_weighting_curves_(1).svg.

[2] ANSI/ASA. *Quantities and Procedures for Description and Measurement of Environmental Sound Part 6: Methods for Estimation of Awakenings Associated with Outdoor Noise Events Heard in Homes*. ANSI/ASA. Washington, DC, USA, 2008.

[3] Federal Inter-agency Committee on Aviation Noise (FICAN). "Sleep Disturbance caused by aviation noise". In: (2007).

[4] Universal Avionics. "Understanding Required Navigation Performance (RNP) and Area Navigation (RNAV) Operations". May 2018.

[5] et. al. Boeker ER Dinges E. *Integrated noisemodel (INM) version 7.0 technical manual*. Tech. rep. ReportFAA-AEE-08-01. Washington, DC, USA: Federal Aviation Administration, 2007.

[6] Edmund K. Burke and Kendall Graham. *Search methodologies: Introductory tutorials in optimization and decision support techniques, second edition*. Springer, 2014, pp. 1–716. ISBN: 9781461469407. DOI: 10.1007/978-1-4614-6940-7. arXiv: 0910.4899v1.

[7] R. Torres; J. Chaptal; "Optimal, Environmentally Friendly Departure Procedures for Civil Aircraft". In: *Journal of Aircraft* Vol. 48.No. 1 (Jan. 2011).

[8] Joeri Dons. "Optimization of Departure and Arrival Routing for Amsterdam Airport Schiphol". MA thesis. TU Delft, June 2012.

[9] R.A.A.Wijnen H. G. Visser S. J. Heblij. *Improving the Management of the Environmental Impact of Airport Operations*. Tech. rep. NLR, 2008.

[10] S. Hartjes and H. Visser. "Efficient trajectory parameterization for environmental optimization of departure flight paths using a genetic algorithm". In: *Proceedings of the Institution of Mechanical Engineers, Part G: Journal of Aerospace Engineering* 0.0 (2016), pp. 1–9. ISSN: 0954-4100. DOI: 10.1177/0954410016648980. URL: http://pig.sagepub.com/lookup/doi/10.1177/0954410016648980.

[11] S. Hartjes, H. G. Visser, and S. J. Hebly. "Optimisation of RNAV noise and emission abatement standard instrument departures". In: *Aeronautical Journal* 114.1162 (2010), pp. 757–767. ISSN: 00019240. DOI: 10.1017/CBO9781107415324.004. arXiv: arXiv:1011.1669v3.

[12] R H Hogenhuis, S J Hebly, and H G Visser. "Optimization of area navigation noise abatement approach trajectories". In: *Proceedings of the Institution of Mechanical Engineers Part G-Journal of Aerospace Engineering* 225.G5 (2011), pp. 513–521. ISSN: 0954-4100. DOI: 10.1177/09544100JAERO840.

[13] *IATA Forecasts Passenger Demand to Double Over 20 Years*. IATA. Oct. 2016. URL: http://www.iata.org/pressroom/pr/Pages/2016-10-18-02.aspx.

[14] ICAO. *Aircraft Operations Volume II - Construction of Visual and Instrumental Flight Procedures*. Tech. rep. ICAO, Oct. 2006.

[15] Payuna Uday Karen B Marais Tom G Reynolds. "Evaluation of potential near-term operational changes to mitigate environmental impacts of aviation". In: *Proceedings of the Institution of Mechanical Engineers, Part G: Journal of Aerospace Engineering* Vol 227.Issue 8 (July 2012).

[16] Q. Zhang; H. Li. "The performance of a new version of MOEA/D on CEC09 unconstrained MOP test instances." In: *IEEE Transactions on Evolutionary Computation* 11.6 (2007), pp. 712–731.

[17] LVNL. *AIS the Netherlands: EHAM - AMSTERDAM/SCHIPHOL*. LVNL. 2018. URL: http://www.ais-netherlands.nl/.

[18] Public Works Ministry of Transport and Water Management. *Performance Based Navigation (PBN): ROADMAP for the Kingdom of the Netherlands 2010-2020*. May 2010.

[19] International Civil Aviation Organization. *Procedures for Air Navigation Services Aircraft Operations*. Volume I. ICAO Document Number 8168. International Civil Aviation Organization. Montreal, QC ,Canada, 2006.

[20] Xavier Prats et al. "Multi-objective optimisation for aircraft departure trajectories minimising noise annoyance". In: *Transportation Research Part C: Emerging Technologies* 18.6 (2010), pp. 975–989. ISSN: 0968090X. DOI: 10.1016/j.trc.2010.03.001. URL: http://dx.doi.org/10.1016/j.trc.2010.03.001.

[21] Subramanian Ramasamy et al. "Novel Flight Management System for Real-Time 4-Dimensional Trajectory Based Operations". In: *AIAA Guidance, Navigation, and Control (GNC) Conference* (2013). DOI: 10.2514/6.2013-4763. URL: http://arc.aiaa.org/doi/10.2514/6.2013-4763.

[22] Lina Abdallah Salah Khard. "Optimization approaches of aircraft flight path reducing noise: Comparison ofmodeling methods". In: *Applied Acoustics* Vol. 73.Issue 4 (Apr. 2012), Pages 291-301.

[23] *Takeoff weight diagram*. June 2014. URL: https://commons.wikimedia.org/wiki/File:Takeoff_weight_diagram.svg.

[24] H.G. Visser V. Ho-Huu S. Hartjes. "An improved MOEA/D algorithm for bi-objective optimization problems with complex Pareto fronts and its application to structural optimization". In: *Expert Systems With Applications 92* 92 (2018).

[25] T.L. Verbraak. "Large scale ADS-B data and signal quality analysis". In: *12th USA/Europe Air Traffic Management Research and Development Semina* (2017).

[26] Hendrikus Visser Vinh Ho-Huu Sander Hartjes. "An Efficient Application of the MOEA/D Algorithm for Designing Noise Abatement Departure Trajectories". In: *Aerospace* 4.54 (Nov. 2017).

[27] H. G. Visser. "Generic and site-specific criteria in the optimization of noise abatement trajectories". In: *Transportation Research Part D: Transport and Environment* 10.5 (2005), pp. 405–419. ISSN: 13619209. DOI: 10.1016/j.trd.2005.05.001.

[28] H. G. Visser and R. A A Wijnen. "Optimisation of noise abatement arrival trajectories". In: *Aeronautical Journal* 107.1076 (2001), pp. 607–615. ISSN: 00019240. DOI: 10.2514/2.2838.

[29] Arnoud Vooren. *Jaarrapportage 2017*. Research rep. Bewoners Aanspreekpunt Schiphol (BAS), Mar. 2018.

[30] H.G. Visser; R.A.A. Wijnen. "Optimization of Noise Abatement Departure Trajectories". In: *Journal of Aircraft* (2001).

[31] R. A A Wijnen and H. G. Visser. "Optimal departure trajectories with respect to sleep disturbance". In: *Aerospace Science and Technology* 7.1 (2003), pp. 81–91. ISSN: 12709638. DOI: 10.1016/S1270-9638(02)01183-5.

[32] Hui LI; Qingfu Zhang. "Multiobjective Optimization Problems With Complicated Pareto Sets, MOEA/D and NSGA-II". In: *IEEE Transactions on Evolutionary Computation* 13.2 (Apr. 2009).

A

Standard Instrument Departures

See next page.

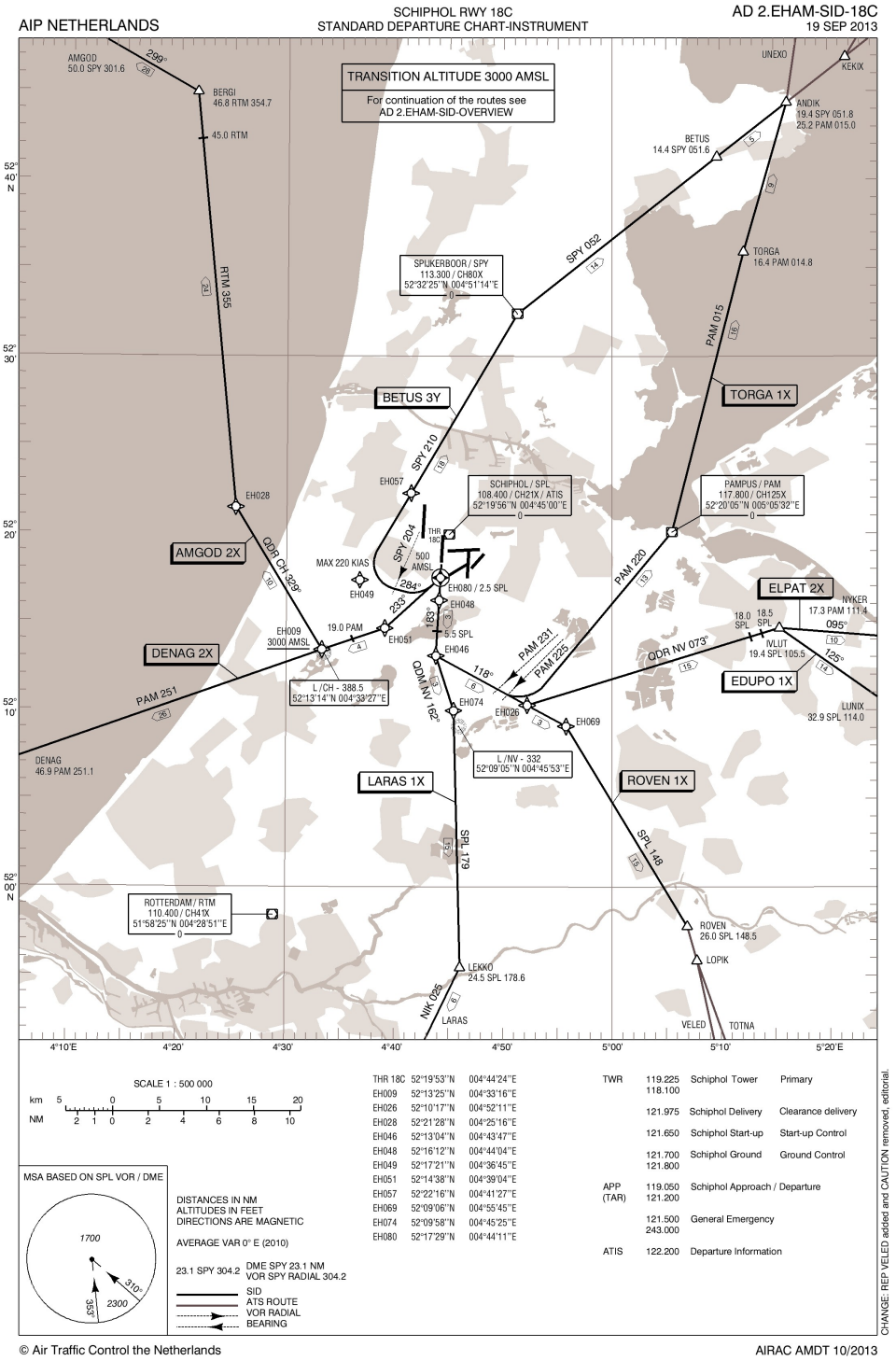

Figure A.1: Current SID Spijkerboor 2K [17]

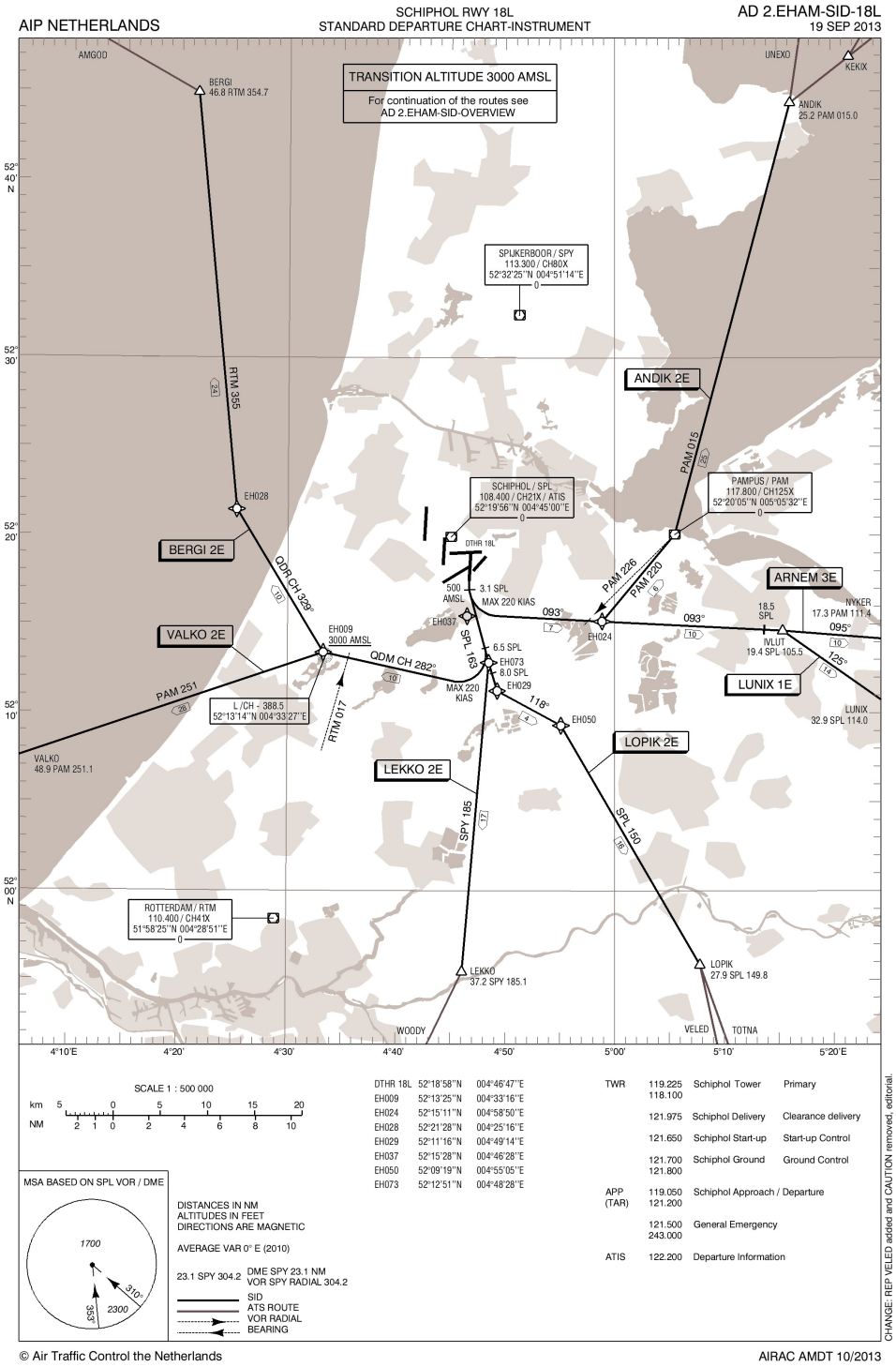

Figure A.2: Current SID ARNEM 3E [17]

B

MOEA/D Algorithm

See next page.

Algorithm 1. MOEA/D algorithm

Input:

- A multi-objective optimization problem;
- A stopping criterion;
- N: number of sub-problems;
- $\mathbf{w}^i = (w_1^i, .., w_m^i), i = 1, \dots, N$: a set of N weight vectors;
- T_m: size of mating neighbourhood;
- T_{rmax}: maximum size of replacement neighbourhood;
- δ the probability that mating parents are selected from the neighborhoods;
- *MaxIter*: maximum iteration;

Step 1. Initialization

1.1. Find the T_m closest weight vectors to each weight vector based on the Euclidean distances of any two weight vectors. For each sub-problem $i = 1, \dots, N$ set $\mathbf{B}^i = (i_1, .., i_{T_m})$ where $\mathbf{w}^{i_1}, \dots, \mathbf{w}^{i_{T_m}}$ are the closest weight vectors to $\mathbf{w}^i$;

1.2. Create an initial population $\mathbf{P} = \{\mathbf{x}^1, \dots, \mathbf{x}^N\}$ by uniformly randomly sampling from design space Ω. Evaluate the fitness value FV^i of each solution $\mathbf{x}^i$, i.e. $FV^i = (f_1(\mathbf{x}^i), \dots, f_m(\mathbf{x}^i))$ and set $\mathbf{FV} = \{FV^1(\mathbf{x}^1), \dots, FV^N(\mathbf{x}^N)\}$;

1.3. Initialize ideal point $\mathbf{z}^* = (z_1^*, \dots, z_m^*)^T$ by setting $z_j^* = \min\{f_j(\mathbf{x}) | \mathbf{x} \in \Omega,\ j = 1, .., m\}^T$

1.4. Set generation: $gen = 1$;

Step 2. Update

while (the stopping condition is not satisfied)

for $i = 1, \dots, N$; do

2.1. Selection of mating/update range

Set $\mathbf{B}_m = \begin{cases} \mathbf{B}^i & if\ rand < \delta \\ \{1, \dots, N\} & \text{otherwise} \end{cases}$

where *rand* is a uniformly distributed random number in [0,1];

2.2. Reproduction: randomly select three parent individuals r_1, r_2 and r_3 ($r_1 \neq r_2 \neq r_3 \neq i$) from $\mathbf{B}_m$ and generate a solution $\bar{\mathbf{y}}$ by applying "DE/rand/1" operator, and then perform a mutation operator on $\bar{\mathbf{y}}$ to create a new solution $\mathbf{y}$;

2.3. Repair: if any element of $\mathbf{y}$ is out of Ω, its value will be randomly regenerated inside Ω;

2.4. Evaluate the fitness value of new solution $\mathbf{y}$;

2.5. Update of $\mathbf{z}^*$ and $\mathbf{z}^{nad}$: for each $j = 1, \dots, m$ if $z_j^* \leq f_j(\mathbf{x}^i)$ then set $z_j^* = f_j(\mathbf{x}^i)$, and if $z_j^{nad} \geq f_j(\mathbf{x}^i)$ then set $z_j^{nad} = f_j(\mathbf{x}^i)$;

2.6. Update of solutions: use an adaptive replacement strategy in [23]:

end for

Set $FEs = FEs + N$, and $gen = gen + 1$;

Step 3. Stopping condition

Use a stopping criterion in [24].

if (stopping criterion is satisfied or *MaxIter* is reached)

Stop the algorithm;

end if

end while

Output: Pareto set $\mathbf{PS} = \{\mathbf{x}^1, \dots, \mathbf{x}^N\}$; Pareto front $\mathbf{PF} = \{FV^1(\mathbf{x}^1), \dots, FV^1(\mathbf{x}^N)\}$.

Figure B.1: The multi-objective evolutionary algorithm based on decomposition [26]